

UNIVERSITY OF OSNABRUECK

DOCTORAL THESIS

**Orthogonal substrate functionalization using
additive contact lithography**

Author

Fatih Alarslan

Supervisor

Prof. Dr. Martin Steinhart

School of Biology and Chemistry

April 2023, Osnabrück

Dissertation to partially fulfill the requirements for the degree of
‘Doctor rerum naturalium’
presented by Fatih Alarslan
to the University of Osnabrück

Reviewer #1: Prof. Dr. Martin Steinhart

Reviewer #2: Prof. Dr. Uwe Beginn

Table of contents

Abstract	1
1. Introduction	4
2. State of the art	8
2.1. Classification of substrate-based manufacturing.....	8
2.2. Lithographic patterning	10
2.2.1. Serial lithographic methods.....	10
2.2.2. Parallel lithographic methods.....	13
2.3. Partially and fully porous stamps for lithographic processes.....	15
2.3.1. Fully porous stamps	15
2.3.2. Partially porous stamps	17
2.3.3. DNHG _s and MnO ₂ , which were used in this work for lithography processes.....	17
2.4. Deposited model materials	21
2.4.1. Properties and device integration of LiNbO ₃	21
2.4.2. Properties of NiFe ₂ O ₄ and thin-layer configurations of solvothermal products	30
2.4.3. Properties of PFCMA and on-demand production of tailored surfaces with switchable wettability.....	34
2.5. Wetting on smooth and rough surfaces	36
2.6. Wettability Switching.....	38
3. Thin patterned lithium niobate films by parallel additive capillary stamping of aqueous precursor solutions	40
3.1. Introduction	41
3.2. Experimental section	41
3.2.1. Materials and chemicals	41
3.2.2. Stamp fabrication	42
3.2.3. Preparation of holey LiNbO ₃ films	43

3.2.4.	Electrochemical deposition of gold.....	44
3.2.5.	Characterization	45
3.3.	Results and discussion.....	48
3.3.1.	Pore generation.....	48
3.3.2.	Capillary stamping of aqueous LiNbO ₃ precursor solutions onto ITO substrates	48
3.3.3.	Formation of micropatterned LiNbO ₃ films on ITO substrates	50
3.3.4.	Phase analysis of the layered LiNbO ₃ -ITO system.....	53
3.3.5.	Second harmonic generation of micropatterned LiNbO ₃ films.....	56
3.3.6.	Orthogonal functionalization of ITO substrates: micropatterned LiNbO ₃ -gold films.....	57
3.4.	Conclusion.....	59
4.	Additive solvothermal capillary stamping with double network hydrogel-derived aerogel stamps	61
4.1.	Introduction	62
4.2.	Experimental section	62
4.2.1.	Chemicals and materials.....	62
4.2.2.	Fabrication of DNHG-derived aerogel stamps.....	63
4.2.3.	Additive solvothermal capillary stamping	67
4.2.4.	Electrodeposition of Nickel.....	69
4.2.5.	Characterization of the DNHG-derived aerogel.....	70
4.3.	Results and discussion.....	72
4.3.1.	DNHG-derived aerogel stamps	72
4.3.2.	Arrays of submicron nickel ferrite dots by solvothermal capillary stamping	75
4.3.3.	Properties of submicron nickel ferrite dot arrays	78
4.4.	Conclusion.....	83

5. High-temperature stamping of molten functional polymers: Orthogonal substrate functionalization for wettability management..85

5.1. Introduction	86
5.2. Experimental section	86
5.2.1. Chemicals and materials.....	86
5.2.2. Synthesis and characterization of PFcMA	87
5.2.3. Preparation of Ni/MnO ₂ composite stamps.....	88
5.2.4. High temperature capillary stamping	90
5.2.5. Electrochemical analyses and treatments of PFcMA-CNT hybrid microdot arrays.....	92
5.2.6. Microscopic characterization of PFcMA-CNT hybrid arrays	92
5.2.7. Surface analysis by X-ray photoelectron spectroscopy.....	92
5.2.8. Investigations of wettability and evaporation dynamics	93
5.3. Results and discussion.....	93
5.3.1. High-temperature capillary stamping.....	93
5.3.2. Wettability switching.....	98
5.4. Conclusion.....	103
6. Summary	105
Literature	108
Acknowledgments.....	127
List of publications	129
Curriculum Vitae	130
Statement of Authorship.....	131

Abstract

This work focuses on the orthogonal substrate functionalization by using parallel, additive contact lithography. Orthogonal functionalization of substrates patterned by capillary stamping may yield functional hybrid layers, in which the properties of the stamped pattern and the second component can be coupled. The coupling of functional films can lead to both additive and synergistic effects, allowing the properties of the hybrid film to be targeted for specific applications. Three different examples were investigated for this purpose. Lithiumniobate (LiNbO_3), nickel ferrite ($\text{Ni}_2\text{Fe}_4\text{O}_4$), and poly(2-(methacryloyloxy)ethyl ferrocenecarboxylate) (PFcMA) were each stamped and orthogonally functionalized with various components. While the stamping of LiNbO_3 on previously developed stamping techniques, the other two examples involve new developed stamping techniques such as solvothermal stamping and stamping from polymer melts. Microstructured LiNbO_3 holey films were generated by direct stamping with a polystyrene-*block*-poly(2-vinylpyridine) (PS-*b*-P2VP) stamp an aqueous solution of lithium acetate ($\text{C}_2\text{H}_3\text{LiO}_2$) and niobium oxalate hydrate ($\text{C}_{10}\text{H}_5\text{NbO}_2 \cdot 6 (\text{H}_2\text{O})$). Calcination of the stamped precursor film on ITO resulted in pure LiNbO_3 without any impurities. Orthogonal modification of the LiNbO_3 -film with gold nanoparticles via electrodeposition at the positions of the macropores increased the intensity of the second harmonic output by a factor of 5.4. Capillary imprinting with DNHG-derived aerogel stamps combined with a solvothermal synthesis based on ethanol solutions of iron(III) acetylacetonate ($\text{Fe}(\text{C}_5\text{H}_7\text{O}_2)_3$) and nickel(II) acetylacetonate ($\text{C}_{10}\text{H}_{14}\text{NiO}_4$) yielded submicron arrays of nickel ferrite dots on indium tin oxide (ITO) substrates. Then, the ITO substrates functionalized with ordered monolayers of submicron nickel ferrite dots were further orthogonally functionalized with metallic nickel by electrodeposition. The submicron nickel ferrite dots reduced the remanence of the ferromagnetic nickel film by half, while the saturation value of the magnetic moment per area remained largely constant. Furthermore, hybrid stamps made of Ni/ MnO_2 were generated for capillary microstamping of the stimuli-responsive ferrocene-containing polymer (PFcMA) blended

with multiwalled carbon nanotubes (CNTs) from the melt. Electrochemical WCA switching reversibly transformed the PFCMA-CNT hybrid microdots from a high-WCA state, in which the PFCMA is reduced, to a low-WCA state, in which the PFCMA is oxidized (the ferrocene units are positively charged), and *vice versa*. Orthogonal substrate functionalization of the areas around the PFCMA-CNT hybrid microdots shifted the WCA switching range by nearly 50°.

Diese Arbeit fokussiert sich auf die orthogonale Substratfunktionalisierung mittels paralleler, additiver Kontaktlithographie. Die orthogonale Funktionalisierung von Substraten, die durch Kapillarstempeln mit einem funktionalen Material strukturiert werden, kann funktionelle Hybridsysteme erzeugen, bei denen die Eigenschaften des gestempelten Films und der zweiten Komponente gekoppelt werden können. Das Koppeln funktionaler Filme kann sowohl zu additiven, als auch zu synergistischen Effekten führen, sodass die Eigenschaften des Hybridfilms gezielt für bestimmte Anwendungen verwendet werden können. Drei verschiedene Beispiele wurden zu diesem Zweck untersucht. Lithiumniobat (LiNbO_3), Nickelferrit ($\text{Ni}_2\text{Fe}_4\text{O}_4$) und Poly(2-(methacryloyloxy)ethyl ferrocencarboxylat) (PFCMA) wurden jeweils gestempelt und orthogonal mit verschiedenen Komponenten funktionalisiert. Während das Stempeln von LiNbO_3 auf vorher entwickelte Stempeltechniken aufbaut, beinhalten die beiden anderen Beispiele neu entwickelte Stempeltechniken wie solvothermales Stempeln und Stempeln von Polymerschmelzen. Löchrige, mikrostrukturierte LiNbO_3 -Filme wurden aus einer wässrigen Lösung, welche aus Lithiumacetat und Nioboxalat-Hydrat Lösung besteht, mittels PS-*b*-P2VP verstampelt. Die Kalzinierung des gestempelten Precursor-Films auf Indiumzinnoxid (ITO-Glas) führte zu reinem LiNbO_3 ohne jegliche Verunreinigungen. Die Lochfilme aus LiNbO_3 weisen, abgesehen an den Positionen der Mikrolöcher, ein einheitliches *SHG*-Signal auf. Die orthogonale Modifizierung der LiNbO_3 -Lochfilme erfolgte durch die Elektrodeposition von Goldnanopartikeln an den Positionen der Mikrolöcher und führte zu einer Erhöhung der *SHG*-Intensität um den Faktor 5.4. Das Kapillarstempeln mit DNHG-abgeleiteten Aerogelstempeln kombiniert mit einer

solvothermalen Synthese basierend auf Ethanollösungen von Eisen(III)-Acetylacetonat ($\text{Fe}(\text{C}_5\text{H}_7\text{O}_2)_3$) und Nickel(II)-Acetylacetonat ($\text{C}_{10}\text{H}_{14}\text{NiO}_4$) ergaben periodisch angeordnete Nickelferrit-Dots auf Indiumzinnoxid ITO-Substrate. Anschließend wurden die ITO-Substrate, die mit geordneten Monoschichten von mikroskaligen Nickelferrit-Dots funktionalisiert waren, durch Elektrodeposition orthogonal mit metallischem Nickel funktionalisiert. Die submikronen Nickel-Ferrit-Dots reduzierten die Remanenz des ferromagnetischen Nickel-Films um die Hälfte, während der Sättigungswert des magnetischen Moments pro Fläche größtenteils konstant blieb. Zusätzlich wurden Hybridstempel aus Ni/MnO₂ entwickelt, um das stimuli-responsives Ferrocen-Polymer PFCMA zusammen mit mehrwändigen Kohlenstoffnanoröhren (CNTs) mittels Kapillar-Mikrostempeln aus der Schmelze zu stempeln. Elektrochemisches Wasserkontaktwinkel-Schalten transformierte die PFCMA-CNT-Hybridmikrodots reversibel von einem hohen Wasserkontaktwinkel-Zustand, in dem das PFCMA reduziert wird, in einen niedrigen Wasserkontaktwinkel-Zustand, in dem das PFCMA oxidiert wird (die Ferrocen-Einheiten sind positiv geladen) und umgekehrt. Die orthogonale Substratfunktionalisierung der Bereiche um die PFCMA-CNT-Hybridmikrodots verschob den Wasserkontaktwinkel-Schaltbereich um fast 50°.

1. Introduction

Nowadays functional surfaces with various morphologies and different physico-chemical properties^[1] are of great importance for both in industry and research. Accordingly, they have been extensively investigated in the last decades as they have quite a few applications, such as in fields like optics,^[2] electronics,^[3] data storage,^[4] energy conversion and storage,^[5] catalysis,^[6] sensing,^[7] smart machines,^[8] and many other fields.

This work focuses on the orthogonal substrate functionalization by using parallel, additive contact lithography. By patterning substrates through capillary stamping, it is possible to create functional hybrid layers that combine the properties of the stamped pattern with those of a second component. This coupling can result in additive or synergistic effects that can be tailored to specific applications. The additive or synergistic interplay of the stamped pattern and the second functional component may allow for customizing the substrate properties in a way not possible otherwise.^[9,10] This work examined three model systems of this concept: The stamping methodology of lithium niobate (LiNbO_3), nickel ferrite ($\text{Ni}_2\text{Fe}_4\text{O}_4$), and poly(2-(methacryloyloxy)ethyl ferrocenecarboxylate) (PFcMA). Each material was stamped and orthogonally functionalized with various components. While the stamping of lithium niobate builds on previous research, the other two examples involve new developed stamping techniques such as solvothermal stamping and stamping from polymer melts.

(I) Lithium niobate (LiNbO_3) is attracting significant interest as a material for photonic components, actuators and data storage devices^[11] because it is characterized by a broad range of beneficial physical properties including ferroelectricity, piezoelectricity, the Pockels effect, photoelasticity and nonlinear optical polarizability.^[12] The advancement of LiNbO_3 -based devices is predominantly driven by thin-film lithium niobate technology.^[13-15] Thin LiNbO_3 layers are commonly transferred onto counterpart substrates by subjecting bulk LiNbO_3 single crystals to ion slicing, involving ion implantation to form blisters defining internal cleavage planes, followed by substrate bonding of the bulk LiNbO_3 single crystals and cleavage. Thus, thin LiNbO_3 layers

separated from the bulk LiNbO_3 single crystals remain attached to the counterpart substrates.^[16,17] Tailoring the properties of thin LiNbO_3 layers frequently requires further microstructural engineering.^[13–15] If, for example, the dimensions of LiNbO_3 -based components are shrunk to the nanoscale, the nonlinear radiation emitted by LiNbO_3 based on quadratic frequency mixing processes is intrinsically weak. This drawback may be overcome by thin patterned hybrid films consisting of LiNbO_3 and a plasmonic material such as gold^[18] because localized surface plasmon (LSP) resonances may boost the second harmonic (SH) output.^[19–24] Up to now, it has remained challenging to lithographically deposit LiNbO_3 precursor formulations by parallel additive patterning methods. Moreover, it would be desirable to use environmentally friendly aqueous precursor formulations for this purpose. So far, thin LiNbO_3 films were prepared from aqueous precursor solutions using, for example, lithium and niobium alkoxides^[25–29] or niobic acid and lithium hydroxide^[30] as lithium and niobium sources. Typically, either precursors are used, which are relatively expensive and difficult to handle, or the preparation of the precursor solutions is complex so that upscaling is challenging.

The first model system is about the generation of microstructured LiNbO_3 films on indium tin oxide (ITO) substrates by direct stamping of mild aqueous precursor via PS-*b*-P2VP stamp. The holey nature of the LiNbO_3 film enabled orthogonal substrate functionalization with gold via electrodeposition at the position of the holes, which resulted in an increase in the second harmonic output intensity by a factor of 5.4.

(II) A broad range of functional materials is accessible by solvothermal syntheses (including hydrothermal reactions), which are carried out in closed vessels, such as autoclaves, at temperatures exceeding the boiling point of the used solvent.^[31,32] Solvothermal syntheses may yield metastable phases, low-temperature phases, or phases otherwise difficult to attain under ambient conditions. For example, reactants insoluble under ambient conditions can be used in solvothermal syntheses. Furthermore, solvothermal syntheses are typically carried out at significantly lower reaction temperatures than alternative syntheses; in contrast to sol-gel syntheses, high-temperature calcination steps are typically not required. Although the production of continuous thin

films from solvothermal reaction products^[33] and their subsequent processing by standard lithography under ambient conditions^[34] has been achieved, direct lithographic patterning of substrates with solvothermal reaction products has remained difficult. Nevertheless, this approach could enable the integration of solvothermal reaction products into device components with complex architectures that go beyond simple thin-layer configurations. However, the porous stamps so far available are not compatible with solvothermal processes, while DNHG-derived aerogel stamps can be used for direct additive contact lithography.

The second model system focuses on additive solvothermal capillary stamping with aerogel stamps derived from double network hydrogels (DNHGs) as an approach to reconcile contact lithography and solvothermal syntheses. Capillary stamping with DNHG-derived aerogel stamps combined with a solvothermal synthesis based on ethanolic precursor solution of iron(III)-acetylacetonate ($\text{Fe}(\text{C}_5\text{H}_7\text{O}_2)_3$) and nickel(II)-acetylacetonate ($\text{C}_{10}\text{H}_{14}\text{NiO}_4$)^[35,36] yielded arrays of submicron nickel ferrite dots on indium tin oxide (ITO) substrates. Then, the ITO substrates functionalized with ordered monolayers of submicron nickel ferrite dots were further orthogonally functionalized with metallic nickel by electrodeposition for magnetic hardening the properties of the pure nickel film.

(III) Surfaces with tailored wettability may exhibit customized antifouling, antifogging, anti-icing and self-cleaning properties and may be used for applications like sensing, oil-water separation, water collection and water purification. Due to this fact, the control of the wettability of surfaces by additive surface manufacturing has attracted great interest.^[37-41] Frequently, surfaces are in many application scenarios in contact with water, aqueous solutions, or aqueous suspensions, making the apparent water contact angle (WCA) a suitable phenomenological descriptor for wettability. Depending on the application, either complete wettability associated with a spreading corresponding to a WCA of 0° , partial wettability ($\text{WCA} < 90^\circ$) or non-wettability ($\text{WCA} > 90^\circ$) is desired. The ability to vary WCAs can expand the functional versatility of surfaces, whereby shape-memory polymers or otherwise stimuli-responsive polymers may be deployed.^{[42-}

^{44]} Therefore, surface functionalization with stimulating polymers is an obvious approach to surfaces with switchable wettability. Patterns of discrete stimuli-responsive polymers, such as arrays of stimuli-responsive polymer microdots, offer additional advantages over continuous coatings. The advantage of microdot arrays over continuous layers is that they are not susceptible to crack propagation and delamination.

The third model system focuses on a potential manufacturing platform enabling the flexible on-demand production of tailored surfaces with switchable wettability by additive lithographic high-temperature deposition of molten stimuli-responsive polymers. For this purpose, high-temperature capillary stamping of melts of the stimuli-responsive ferrocene-containing polymer PFCMA^[45,46] blended with multiwalled carbon nanotubes (CNTs) were deployed. As example, arrays of PFCMA-CNT hybrid microdots onto conductive indium tin oxide (ITO) substrates electrochemical WCA switching reversibly transformed the PFCMA-CNT hybrid microdots from a high-WCA state, in which the PFCMA is reduced, to a low-WCA state, in which the PFCMA is oxidized (the ferrocene units are positively charged), and *vice versa* were stamped. Orthogonal substrate functionalization of the areas around the PFCMA-CNT hybrid microdots shifted the WCA switching range by nearly 50°.

2. State of the art

2.1. Classification of substrate-based manufacturing

Substrate-based manufacturing processes consist of six distinct components, including manufacturing technology, contact topology, substrate transport, substrate velocity, substrate feed, and degree of integration. These components are largely independent of each other and characterize any substrate-based manufacturing process. When combined, these components offer dozens of potential manufacturing process designs, far exceeding the current discussion about upscaling production of printed electronics. Figure 2.1 illustrates these components and their corresponding characteristics. The manufacturing technology component describes the procedurally by which a defined and distinct pattern is applied to the substrate.^[47]

Manufacturing Technology	Additive	Printing	Coating	Vacuum Deposition	...	
	Subtractive	Laser ablation	Photo-lithography	...		
	Structuring	Wetting/ De-Wetting	Imprint	Bonding	...	
Contact Topology	Flat on Flat	Round on Flat	Round on Round	Non-Contact on Flat	Non-Contact on Round	
Substrate Transport	Roll to Roll	Sheet to Sheet	Sheets on Shuttle	Roll to Sheet		
Substrate Velocity	Discontinuous		Continuous			
Substrate Feed	Intermittent		Non-stop			
Degree of Integration	Low (Offline)		Intermediate		High (Inline)	

Figure 2.1: Classification of substrate-based manufacturing processes.^[47]

There are three main categories of manufacturing technologies: additive, subtractive, and structuring. Additive technologies involve applying a distinct pattern onto the substrate through lithographic deposition of materials by processes such as printing, coating, or vacuum deposition. Liquid phase processing is commonly used in the graphical printing

and coating industries, with methods such as gravure, screen, offset, and lithographic printing, as well as blade and slot die coating. Vacuum deposition methods like sputtering and physical vapor deposition also produce uniform layers. Subtractive technologies, on the other hand, remove a part of the deposited material from the substrate or of the substrate itself, such as through laser ablation or photolithography combined with wet chemical etching. The third category, structuring technologies, involves wetting/dewetting, imprinting, or bonding to create patterns. In addition to directly applying functional materials, external devices or other substrates can be attached to the substrate through adhesive or welding techniques.^[47] Similarly, a distinction is made between serial and parallel lithographic methods. Serial and parallel lithography are two different methods for producing micro and nanostructures on a substrate. Serial lithography refers to methods where the structuring is carried out pixel-by-pixel. This means that each pixel of the structure is produced individually. Typically, a photoresist is applied to the substrate and a pattern is produced by a scanning laser or electron beam. Then, the photoresist is developed, and the steps are repeated until the structure is fully built. Serial lithography is a very precise method used for producing micro and nanoelectronic devices such as transistors and memory chips, as arbitrary patterns can be flexibly produced. However, serial lithography is also associated with drawbacks such as low throughput and limited areas and volumes that can be structured. On the other hand, parallel lithography refers to a method where the structuring is carried out all at once over a large area. It typically uses a mask set or a stamp containing the desired pattern, which is then transferred onto the substrate. The mask set consists of a transparent material that is coated with an opaque layer in certain areas. Light is projected through the transparent areas onto the substrate, where it creates the desired pattern. Parallel lithography is a fast method for producing micro and nanostructures over large areas, used for applications such as producing solar cells and optical devices. For this work, the parallel, additive lithographic methods are of great importance.^[48-50]

2.2. Lithographic patterning

In this section, important lithographic methods for this work are described and discussed, with a focus on additive lithographic patterning divided into serial and parallel methods such as contact microstamping, polymer pen lithography and ballistic printing.

2.2.1. Serial lithographic methods

2.2.1.1. Contact microstamping

Microcontact printing is a method for structuring surfaces. The method was developed in the nineties and has attracted a lot of attention over time. Soft lithography is used to produce stamps that can be used for contact stamping. Soft lithography ^[51] involves various methods of using elastomers to reproduce certain structures in the micrometer and nanometer range.^[52] The most common methods for molding structures using elastomers are replicate molding^[53], micromolding in capillaries^[54,55], microtransfer molding^[56] and solvent-assisted microcontact-molding.^[57] In general, with contact microstamping using a polymer stamp, large areas of a substrate are chemically modified with different components and patterned with nano- or microscale structures (Figure 2.2).

[52]

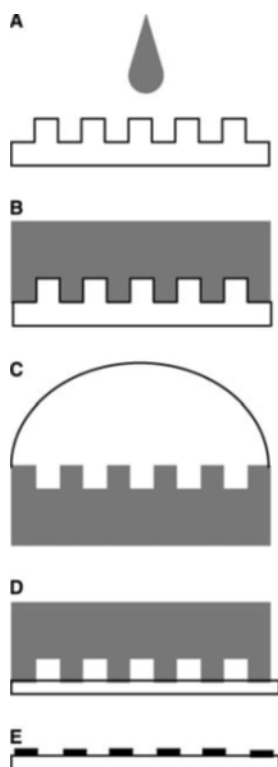


Figure 2.2: Schematic representation of the contact stamping. PDMS is poured over the structured surface (A) and forms the inverse pattern of the template (B). After the PDMS stamp has hardened, it is detached from the template and wetted with ink (C). The ink, deposited on the surface of the PDMS stamp, is transferred to a substrate (D) by the stamping process, so that the substrate is patterned with the ink (E).^[52]

Polydimethylsiloxane (PDMS) is the polymer that is most often used for molding structures, as the soft stamp enables conformal contact between the stamp and the substrate. The components of the ink are adsorbed on the surface of the PDMS. The stamp is attached to the substrate and after detachment the substrate is patterned with the ink. Although the method is uncomplicated and efficient, it has certain disadvantages. One of the problems is that the addition of the ink swells the polymer, so that the structures increase in size and individual tips are no longer uniform. Likewise, after the ink is deposited from the stamp to the substrate, there is an excess transfer of ink, which means that no regularly arranged structures arise. In addition, the soft stamps can be deformed at any time due to coupling, kinking or collapse of the contact elements when they come into contact with the substrate. With solid PDMS stamps, only a few stamp-substrate contacts can be made before ink has to be reloaded. The adsorption of ink is very time-consuming and makes scaling up complicated.^[52,58]

In addition to this common method, there are several other variations that are based on the same principle. The variations are, for example, modified PDMS stamps with which electromagnetic structuring^[58] or electrochemical transfer^[59] can be implemented.

2.2.1.2. Polymer pen lithography

Polymer pen lithography (PPL) is also a special form of contact stamping that was investigated by Mirkin et al^[50], among others. They report a scanning probe lithography method in which a soft elastomer with regularly arranged tips instead of a single tip is mounted on a cantilever to deposit inks directly on a surface. A typical PPL array consists of an elastomer that is cured in a silicon mold made by photolithography and then attached to a flat, transparent substrate (Figure 2.3). The regularly arranged tips are used as contact elements, as in classic contact stamping. PPL arrays with up to 11.000.000 pens were produced, which enable a high throughput and large-area structuring of surfaces. In addition, with PPL, the contact force of the tip substrate can be used to control the structure size, which enables the creation of micro- and nanoscale structures by varying the pressure on the tips. This method is the first example of scanning probe lithography using the tip as both a spring and a pressure tool.^[50]

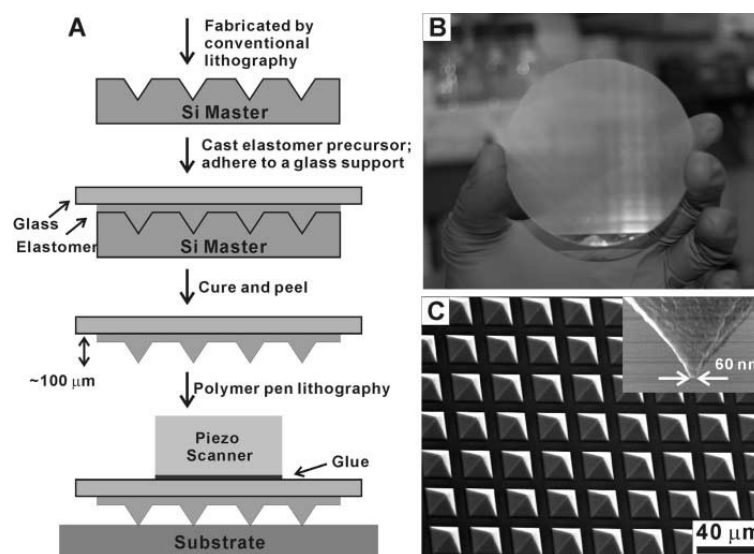


Figure 2.3: A) Schematic representation of the PPL structure. B) Image of a pen array with 11 million regularly arranged tips. C) SEM image of the polymer pen array. The average radius of curvature of the tip is around 70 ± 10 nm.^[50]

2.2.2. Parallel lithographic methods

2.2.2.1. Ballistic printing

Ballistic printing is a group of surface patterning techniques that involves the directed deposition of materials in a continuous and serial manner, resulting in the creation of arbitrary patterns. This technique includes inkjet printing, aerosol jet printing and laser induced forward transfer (LIFT).^[60]

Inkjet printing has been a successful technique in digital printing for many years. It involves ejecting liquid droplets through a nozzle, with two main categories of inkjet printing: continuous inkjet (CIJ) and drop-on-demand (DOD) printing. With CIJ, a continuous stream of droplets is produced and can either be directed towards the substrate or deflected by an electric field onto a droplet collector. With DOD, the liquid is emitted through the nozzle as a short jet that condenses into a droplet only when needed. Droplet diameters typically range from 10 to 100 μm , which corresponds to drop volumes from 0.5 to 500 picoliters ink.^[61]

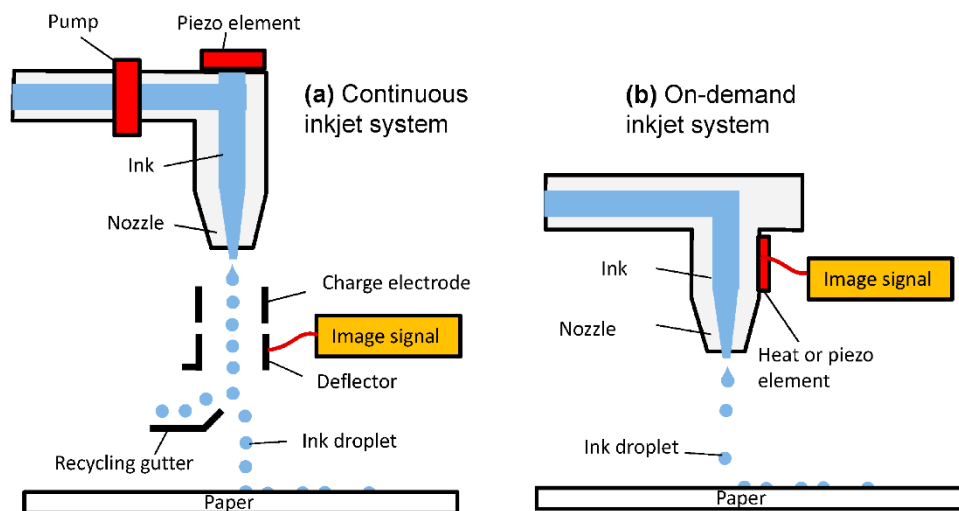


Figure 2.4: Schematic illustration of the two main categories of inkjet printing: (a) continuous inkjet printing and (b) drop-on-demand inkjet printing.^[62,63]

Inkjet printing is a versatile technique that can be used to print a wide variety of materials, including conductive, insulating, and semiconducting inks, as well as biomolecules and other functional materials. This technique can also be easily integrated into existing

manufacturing processes. However, inkjet printing also has some limitations. The resolution and quality of the printed patterns can be affected by factors such as ink viscosity, surface tension, and substrate roughness. Inkjet printing can also be affected by issues such as clogging of the printhead, ink droplet coalescence, and ink evaporation. Despite these limitations, inkjet printing remains a widely used and important technique for the deposition and patterning of functional materials in a variety of applications, including printed electronics, biosensors, and medical devices.^[64–66]

Aerosol jet printing is a 3D printing process based on the aerosol deposition of materials. It uses a finely dispersed mixture of particles and gases to print material onto a surface. The process is capable of printing materials onto surfaces with high precision and resolution, using a wide range of materials such as metals, polymers, ceramics, and organic materials. The process involves several steps: First, the material is converted into a liquid, which is then broken up into small droplets and accelerated by a gas flow. The droplets are then passed through a narrow nozzle, which controls the size and velocity of the droplets. The droplets are then printed onto a surface, forming a solid film of the material. Aerosol jet printing is used in various applications such as the production of flexible electronic components, solar cells, MEMS devices, sensors, and biomedical implants. The process offers many advantages over other printing methods, including high precision, high resolution, and the ability to print materials onto uneven surfaces.^[67–69]

Laser Induced Forward Transfer (LIFT) is a 3D printing technique that is based on the use of laser light to transfer materials from a donor layer to a receiving substrate. It is commonly used in micro- and nanotechnology to create precise structures with high resolution and thickness. For this purpose, a thin layer of the material is deposited onto a carrier film, which is then placed onto the target substrate. Then, a short laser pulse is directed onto the backside of the carrier film, causing the layer of material to be transferred onto the target surface. LIFT offers many advantages over other 3D printing methods, including the ability to transfer a variety of materials onto a wide range of substrates. It is also suitable for the fabrication of complex structures such as circuits,

microfluidic systems, and bio-components. The technology is currently used in various applications, including biomedicine, electronics, and sensing.^[70,71]

2.3. Partially and fully porous stamps for lithographic processes

This chapter describes partially and fully porous materials such as polydimethylsiloxane PDMS and polystyrene-block-poly(vinyl pyridine) PS-*b*-P2VP, which were used as stamps for lithographic processes to generate thin films of functional materials. Furthermore, materials such as DNHGs and MnO₂ are described, which were used as stamps for capillary microstamping in this work.

2.3.1. Fully porous stamps

Xu et al reported on porous polymer stamps, which are produced by a one-step phase separation. With porous stamps, the main disadvantages of microcontact printing could be circumvented and polar inks, in particular aqueous solutions for dendrimers, proteins and nanoparticles with a diameter of 60 nm could be transferred directly to the substrate via contact stamping.^[72] Stamp production was based on a process known as “non-solvent-induced phase separation” (NIPS). In NIPS, a solution of a polymer in a good solvent is added to an excess of a non-solvent for the polymer. A phase separation occurs into a solvent-rich and a polymer-rich phase, with the latter solidifying if the polymer content is high enough.^[73] The disadvantage of spinodal segregation and thus NIPS is that the morphology of the polymer sponges obtained in this way is irregular and difficult to adjust. In addition, the mechanical properties of the pore walls are poor, since the polymer chains in the confinement of the pore walls form only a few intermolecular entanglements.

Capillary microstamping is an additive substrate patterning method using spongy, mesoporous stamps. Schmidt et al^[74] reported on contact stamping using spongy, mesoporous silica stamps, which were manufactured using the sol-gel method. The stamps were provided with regularly arranged contact elements by molding macroporous

silicon templates. With the silica stamps, fullerene nanoparticles with a diameter of approx. 100 nm and a 1-dodecanethiol solution could already be stamped.^[74] In addition Hou et al^[75], and Han et al^[76] also reported on a lithographic stamping process using PS-*b*-P2VP stamps. The PS-*b*-P2VP sacrificial stamps were topographically patterned with pyramid-shaped contact elements and a spongy, continuously mesoporous nanopore system. The contact elements were obtained by molding macroporous silicon, while the porosity is due to the swelling of the stamp in ethanol. Guo et al^[77] used a PS-*b*-P2VP stamp with hexagonally arranged macropores to generate holey films of NaCl.

Before PS-*b*-P2VP were used as stamp for contact lithography, Wang et al. developed a method to create nanoporous BCP nanorods^[78-80] using anodic aluminum oxide (AAO) molds via non-destructive swelling-induced pore generation. This was achieved by treating BCP minority domains with selective solvents that cause osmotic pressure to drive the solvent into the minority domains, resulting in selective swelling. The glassy matrix of the BCP majority component then undergoes structural changes to accommodate the increased volume of the swollen minority domains. After the swelling process, the extended chains of the minority component undergo entropic relaxation, resulting in the formation of pores in place of the swollen minority domains. The resulting continuous pore networks can have adjustable pore diameters and can be open to the environment. Swelling-induced morphology reconstruction in ethanol at 60 °C of 100 μm thick PS-*b*-P2VP substrates bearing PS-*b*-P2VP nanorods (length 1.5 μm, diameter 300 nm) generated continuous pore systems with P2VP pore walls penetrating the entire specimens.^[81,82]

It was shown that porous stamps^[76,83-87] are particularly suitable for parallel additive substrate patterning even if diluted solutions are used as inks because the pore systems of the stamps act as ink reservoirs. Evaporation of the volatile ink components (typically the solvents) drags more and more of the non-volatile functional ink components into the liquid ink bridges formed between the contact elements of the stamp and the substrate to be patterned. In contrast to classic soft lithography with elastomeric stamps, capillary microstamping allows various organic and aqueous inks to be adsorbed by the porous PS-

b-P2VP stamps, transported by the nanopore system and then deposited on a substrate via the contact elements.

2.3.2. Partially porous stamps

Partially porous stamps are a type of stamp used in lithographic methods. These stamps have a porous region that allows the transfer of ink or other materials to the substrate during printing. The porous region is typically created by selectively removing material from the stamp using techniques such as laser ablation, etching or by replication molding with methods like nanoimprint lithography.^[56,88]

An example of this is structured PDMS, which is produced using the methods that have just been listed. The porous structure of the stamp allows for effective adhesion to the substrate, enabling precise transfer of patterns. By controlling the size and distribution of the pores, the adhesion of the stamp surface to the substrate can also be controlled. Structured PDMS is a popular material for the fabrication of micro and nanostructures due to its high resolution and flexibility. It can be used in many applications, including the fabrication of microfluidic systems, microelectronics, and optical components.^[52,89,90] The porosity of the stamps can be controlled by adjusting the size and distribution of the pores. Partially porous stamps offer several advantages over non-porous stamps in lithographic methods. For example, they can allow for better ink transfer and more precise control over the printed features. Additionally, the porous regions can help to prevent the buildup of air pockets or other defects that can occur during printing. Partially porous stamps have been used in a variety of lithographic techniques, including soft lithography, nanoimprint lithography, and microcontact printing.^[91-93]

2.3.3. DNHG_s and MnO₂, which were used in this work for lithography processes

2.3.3.1. Double network hydrogels

Double network hydrogels (DNHG_s) are a structure consisting of two physically

intertwined, but otherwise independent gel networks.^[94] There should not be too strong interactions between the two gel networks^[95], so that the two individual networks do not strongly influence each other on a microscopic level, but still retain different mechanical characteristics. For example, if there is a very soft, flexible gel network and a hard, rigid network that form strong interactions with each other, such as ionic interactions or a large number of covalent bonds, the two networks will not show separate mechanical characteristics, but behave like a single gel network both on the macroscopic and microscopic levels. In this case, when subjected to mechanical stress, the non-elastic network will break upon sufficient deformation, but the flexible network will also break due to its strong attachment to the rigid network, without being able to counteract the localized stress by distributing the force. Therefore, only the combined strength of both gel networks at the tip of the crack will resist further crack propagation. However, if the two gel networks do not have strong interactions with each other, but are only intertwined and otherwise independent, the inflexible network will break upon sufficient deformation, but the flexible network can move to a relatively large extent within the inflexible network and distribute the forces over a much larger area without tearing itself.^[96-99] This mechanism distributes the stress from the tip of the crack to a large volume of the gel. If the stress within the volume of the gel around the crack becomes too high, the inflexible network also breaks at this point and distributes the stress further into the gel volume with the help of the flexible network.

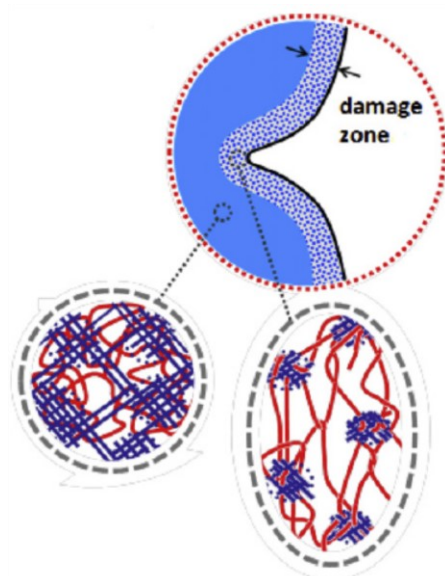


Figure 2.5: Schematic illustration of the sliding crosslinker theory.^[95]

In the literature, this mechanism is referred to as "sliding crosslinkers", as the flexible network is linked by fragments of the inflexible network along which it can practically slide. This distribution of applied stresses over a larger volume of the gel leads to a DNHG with a suitable composition being significantly more stable than the sum of the individual networks. For example, a DNHG made of poly(acrylamidomethylpropane sulfonic acid) and poly(acrylamide) has a fracture strength of 17.2 MPa, while the individual networks have fracture strengths of only 0.4 MPa and 0.7 MPa. Thus, the DNHG is more than 15 times more durable than the sum of the individual networks.^[96]

One limitation of DNHG is their complex two-step synthesis, which significantly restricts their range of applications. The "classical" synthesis by Gong et al. starts from AMPS, which is polymerized with MBA as a crosslinker in a free radical polymerization to form the first gel network. This gel network is then swollen in the monomer solution for the second network (AAM, MBA, and initiator) and polymerized again. Thus, a second network forms within the first network.^[94]

To achieve the high mechanical stability of DNHG, certain conditions must be met. One of the two networks must be highly crosslinked and low in concentration. This network is often made up of an ionic polymer such as pAMPS or polyacrylic acid. The second network must be more highly concentrated, have low crosslinking, and is usually made

of an electrically neutral polymer such as pAAM.^[94,95] Initially, it was believed that there should be no covalent bonds or other strong interactions between the two networks, or that the properties of DNHG would be better the fewer covalent bonds there were between the two networks. However, more detailed investigations by Gong et al. showed that the properties of DNHG were significantly worse when all residual double bonds of the first network were removed before the second polymerization and the second network had no crosslinking. Thus, a low degree of covalent linkages between the two networks does not seem to be fatal for the stabilization mechanism of double network hydrogels. However, an important finding was also that a DNHG consisting of two completely separate networks, in which the second network had a low degree of crosslinking, had better mechanical properties than a DNHG in which both networks had a low degree of crosslinking between them. Therefore, if possible, any bonds between the individual networks should be avoided.^[94] In this work, DNHG were used for the first time as stamps for additive lithography under solvothermal conditions.

2.3.3.2. Porous MnO₂

Broughton and Brett^[100] conducted a study on the properties of hydrous, porous MnO₂ grown through electrodeposition from aqueous solutions. The study focused on MnO₂ grown from MnSO₄ solutions mixed with electrolytes based on acetates for electrochemical capacitor applications. By adding acetates to the electrodeposition solution, the deposition potential under galvanostatic conditions was controllably reduced from approximately 0.95 to 0.55 V. Although some morphological changes were observed in the material under SEM examination when different acetate solutions were used, the capacitance of the material remained insensitive to this variable. The porous manganese oxide layers were utilized in this study to generate a Ni/MnO₂ composite stamp for high-temperature capillary stamping.

2.4. Deposited model materials

In this chapter, the chemical and physical properties of the stamped materials and the substances used for orthogonal modification are described. The issues related to conventional additive lithographic methods for lithographic deposition of LiNbO_3 , PFCMA, and NiFe_2O_4 are also discussed.

2.4.1. Properties and device integration of LiNbO_3

2.4.1.1. Crystal structure

Figure 2.6 shows the ferroelectric phase of LiNbO_3 , which occurs below the Curie temperature of 1210°C .^[101]

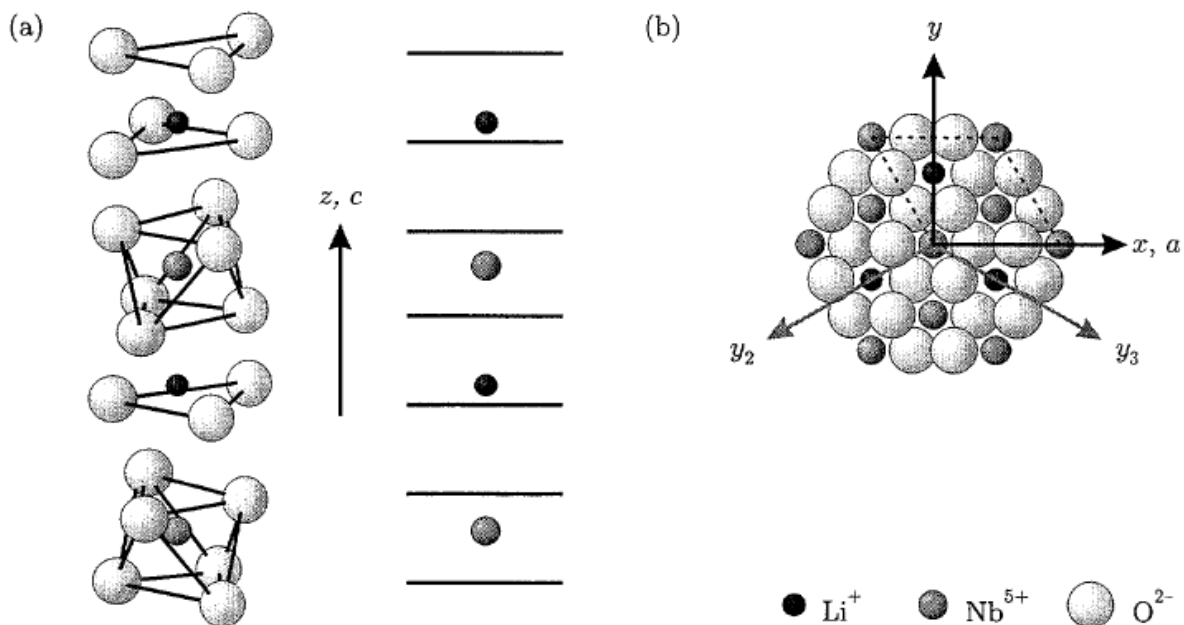


Figure 2.6: Crystal structure of LiNbO_3 in its ferroelectric phase, which occurs below the Curie temperature. a) Positions of lithium and niobium ions relative to the oxygen planes (—) along the crystallographic axis c or along the z -axis in the Cartesian coordinate system. b) LiNbO_3 has a threefold rotational symmetry (y_1, y_2, y_3) along the z or c axis and thus belongs to the space group $3m$.^[12,102]

The ferroelectric phase is defined by planar layers of oxygen atoms with a distorted hcp arrangement. This creates interstitial sites along the crystallographic c -axis, which are

occupied by lithium (Li⁺), niobium (Nb⁺), and vacancies (\square) in a 1:1:1 ratio.^[103]

At room temperature, elastic forces cause the anions to be displaced from their symmetric positions. This results in a spontaneous polarization in one direction of the crystal, which is compensated for at the surface of the crystal by the movable charge carriers. Therefore, LiNbO₃ is a ferroelectric material. The crystal structure and resulting physical effects of LiNbO₃ are temperature-dependent. Above the Curie temperature, the cations have enough energy to oscillate through the oxygen layers, resulting in an average symmetric position and causing the spontaneous polarization to disappear.^[101]

2.4.1.2. Nonlinear optical properties

Due to its crystal structure, LiNbO₃ is optically birefringent. Accordingly, the refractive index depends on the polarization of the incident light, so that the refractive index n_o results for properly polarized light and the refractive index n_e for extraordinarily polarized light. For properly polarized light, the polarization is perpendicular to the c-axis, while with extraordinarily polarized light, the polarization is parallel to the c-axis. As can be seen in equation (2.1), the birefringence δn depends not only on the wavelength but also on the temperature.^[101,104]

$$\delta n(\lambda, T) = n_e(\lambda, T) - n_o(\lambda, T) \quad (2.1)$$

When using a helium-neon laser with a wavelength of 632.8 nm as the light source, n_e and n_o are 2.2028 and 2.2866 at room temperature, so that the birefringence δn is negative^[101]. In addition, LiNbO₃ is an optically non-linear material and is used for frequency doubling. Frequency doubling, also known as second harmonic generation (SHG), is a physical process in which, under certain conditions, the irradiation of some materials with laser light, an additional emission at twice the frequency of the incoming radiation can be observed. When electromagnetic radiation passes through matter, there is an interaction between the oscillating electric field of the light wave and the electric dipole moments of the crystal structure, which are stimulated to vibrate and emit new waves. With a low intensity of the light, the deflections of the electrical charges from their rest position are small, whereby these then oscillate at a frequency that differs slightly from their

resonance. Most of the frequency components of the excitation are thus present. In case of large deflections of the electrical charges from their rest position, the potential that drives the dipole back to its initial state no longer has a parabolic shape, since the nuclear charges of neighboring atoms must now be taken into account. Thus, the optical non-linearity describes the relationship between the deflection and the restoring force, which is no longer linear in the case of high deflections of the electrical charges. When the charges are driven back to their original state, they are accelerated by the potential that binds them to the atomic cores, which results in a sinusoidal course of the speed. In the case of large deflections, however, there are deviations from the sinusoidal curve. As a result, not only the frequency of the incident radiation can be found in the frequency spectrum, but also that of its harmonics. The field strength of the electromagnetic radiation plays a decisive role in generating the frequency doubling. For weak intensities or small field strengths of the electromagnetic radiation, the polarization P increases linearly with the electric field and thus depends only on the first order term.^[104] At high intensities, as it is the case with lasers, higher-order terms must also be taken into account, as can be seen in formula (2.2):

$$P = \varepsilon_0 \sum_n \chi^{(n)} E^n = \varepsilon_0 \chi^{(1)} E + \varepsilon_0 \chi^{(2)} E^2 + \varepsilon_0 \chi^{(3)} E^3 + \dots \quad (2.2)$$

χ : dielectric susceptibility

E : Electric field strength

ε_0 : electrical field constant

In the case of SHG, the second order term in equation (2.2) is decisive. If an electromagnetic wave with high intensity and an angular frequency ω propagates in the z-direction in the material, it becomes a radiation field,

$$E(t) = E_0 \sin(\omega t) \quad (2.3)$$

which is time-dependent. The generated, time-dependent radiation field in turn generates a second order polarization. Trigonometric transformations and the insertion of equation (2.3) into equation (2.2) thus result in:

$$|P^{(2)}| = \frac{\varepsilon_0 E_0^2 \chi^{(2)}}{2} - \frac{\varepsilon_0 E_0^2 \chi^{(2)}}{2} \cos(2\omega t) \quad (2.4)$$

The first term of the 2nd order polarization is a static electric field, which is also referred

as optical rectification. The second term oscillates at twice the frequency of the fundamental wave and generates the SHG in the nonlinear material. So that the second harmonic and the fundamental wave do not cancel each other out (destructive interference), the refractive index in the direction of propagation must be the same for both waves ($n_{2\omega} = n_{\omega}$).^[105,106] In case of a bulk material, where the total material dimension is larger than the coherence length of the process, phase adjustment techniques need to be implemented to avoid a final cancelling interference between the fundamental and the SH wave. Several methods were discussed, such as critical or quasi-phase matching. During critical phase matching, a birefringent crystal such as LiNbO₃ is set up along its optical axis in such a way that the second harmonic and the fundamental wave have the same refractive index when passing through the crystal. The quasi-phase matching is based on the use of ferroelectric crystals. The periodic polarity reversal of the crystal orientation prevents the waves from diverging. Instead, the waves add up and constructively overlap.^[104,106] In the case of nanoparticles, thin films or other structures, which have dimensions that are limited along the direction of light propagation, the phase matching is not required and the SH can be generated at arbitrary wavelength.^[104]

2.4.1.3. Optical properties of gold nanoparticles

The precious metal gold (Au) is a chemical element of the first subgroup. The 5d shell is completely filled with 10 electrons (noble gas electron configuration). The metallic properties are therefore only due to the half-occupied 6s shell. The atoms form a metallic bond with one another, which leads to a free electron density of $n \sim 5.98 \cdot 10^{28} \text{ m}^{-3}$. In the crystalline state, gold has a face-centered cubic unit cell and a lattice constant of $a = 0.41 \text{ nm}$.^[107] The optical properties of gold nanoparticles in the visible spectral range are mainly determined by two types of optical excitations. On one hand, there are the individual excitations of electrons. They are based on optical transitions of individual 5d electrons into empty states of the 6sp band above the Fermi energy. These so-called interband excitations take place in nanoparticles in the same way as in bulk metal and begin at the interband edge (Au: 2.38 eV \sim 520 nm).^[108] In measurements of the optical

density, inter-band excitations show up as a steadily increasing background, which, regardless of the particle size, begins at around 520 nm. From the other side, there is the collective excitation of electrons. The quantum of this excitation is called particle plasmon and represents a collective oscillation of the conduction band electrons of the sp band. It is the dominant phenomenon in the visible spectral range. In the classic image of an oscillator, the conduction band electrons are periodically shifted in relation to the solid lattice atoms by the alternating electrical field of an incident light wave with a suitable frequency. In phases of maximum light field amplitude, an excess of electrons is formed on one side of the particle and a positive excess charge resulting from the remaining ion cores on the other side (Figure 2.7).^[108,109]

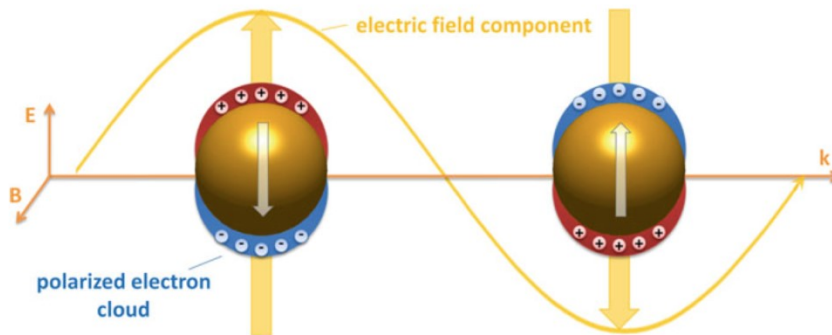


Figure 2.7: Schematic representation of the plasmonic excitation by an electric field.^[110]

The situation can be described as an oscillating dipole, which results in the generation of an electric field around the nanoparticle.

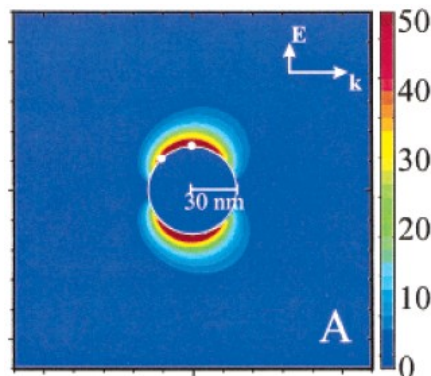


Figure 2.8: Intensity distribution of the electric field in the vicinity of a spherical silver nanoparticle with 60 nm diameter with resonant excitation.^[111]

The dipole is subject to various damping mechanisms depending on the size, which can be either radiating or non-radiating in nature. The restoring force of this oscillation is given by the Coulomb attraction between conduction electrons and ion cores and is harmonious.^[112,113] If the incident light field penetrates the nanoparticle homogeneously (the skin depth for gold is around 35 nm in the visible range^[108]), the situation is a driven, damped, harmonic oscillator that is driven into resonance with a suitable excitation frequency. In the case of spherical Au nanoparticles, the plasmon band of particles with a diameter of ~ 3 nm is at a Wavelength of ~ 520 nm. Plasmonic behavior occurs in all materials whose electrons can be regarded as freely moveable in a first approximation. The spectral position of the plasmon resonance is influenced by several factors. The coulomb fields of the plasmonic dipole run partially through the outer space of the nanoparticle and can thus be shielded depending on the polarizability of the surrounding medium and weaken the restoring force. The larger the refractive index of the surrounding medium, the stronger the external shielding and the resonance shifts spectrally to lower energies or to higher wavelengths.^[108] Internal shields can also lead to a redshift. In this case, the polarizable d electrons of the valence band shield the Coulomb attraction between ion cores and conduction band electrons. The spectral position of the plasmon resonance is, therefore, also dependent on the material of the nanoparticle.^[114] With increasing particle size there are electromagnetic retardation effects. The phase of the generated electromagnetic field in the particle is locally different because of the finite speed of propagation of the driving light, i.e. while small particles are homogeneously penetrated by the light field in terms of space and time, the conduction electrons in larger particles oscillate slightly out of phase between the front and rear. The phase shift, together with the weakening of the light field due to the limited penetration depth, again reduce the repulsive Coulomb forces. There is therefore a redshift that increases with the particle size.^[108]

2.4.1.4. SHG increase by synergistic interplay of LiNbO₃ and gold nanoparticles

The second harmonic generation (SHG) is a second order nonlinear optical process where two photons at a frequency ω interacting with a non-centrosymmetric material, like LiNbO₃, produce a new photon having the double of the initial frequency. At the nanoscale the process does not require the fulfilling of the phase matching condition, i.e., it can be produced at arbitrary wavelengths larger than the material band gap.^[115] It is also known that the intensity of the harmonic signal decreases by decreasing the material dimension making the efficiency of the process intrinsically weak. For example, for spherical nanoparticles the SHG it is known to decrease with the 6th power of the radius, as demonstrated for BaTiO₃.^[116] In the idea to build efficient nonlinear nano-devices, a large part of the research is nowadays devoted to the improvement of the final efficiency. One of the most promising solutions seems to be the exploitation of the plasmon resonance from metallic materials.^[117] Placing such materials, in particular gold^[118], on the top or embedding them on a nonlinear substrate enables stronger harmonic response compared to the situation without the resonant metallic nanostructure.^[118] For example, it has already been demonstrated that the SH output of lithium niobate is 20 times stronger when filled in a plasmonic nanoring resonator.^[119] Recent studies report how a 15-fold increase in second harmonic generation could be generated by coupling a single BaTiO₃ nanoparticle with a spherical metal (Au) nanoparticle in a dimer configuration.^[120] Spherical Au are expected to emit very low SHG^[121] and in this work it was demonstrated that the metal nanoparticle in this hybrid dimer configuration acts as a nonlinear nanoantenna for the BaTiO₃ nonlinear source. The net result is an enhancement of the BaTiO₃ harmonic signal and not a convolution of the signal of the metal nanoparticle and the nonlinear material. To fully exploit the bulk nonlinearity for maximum nonlinear response, it was proposed to embed BaTiO₃ into a core-shell nanocavity. Using this approach, the SHG intensity could be amplified by a factor of 500 experimentally.^[120,122] According to the metal geometry, two types of plasmons can be excited. The first one is called surface plasmon polaritons (SPPs) and it is generated at the metal-dielectric interface when a thin metal film is used. The second one is the localized surface plasmons

(LSPs) which can be created only in presence of nanoparticles. The last one is the one exploited in this work. They are defined as non-propagating excitations of the conduction electrons of the metallic nanostructure coupled to the electromagnetic field. Mathematically these oscillating modes are described using the quasi-static approximation of the scattering theory for sub-wavelength conductive nanoparticles in an oscillating radiation, i.e. the particle size is much smaller than the wavelength of the light in the surrounding medium ($d \ll \lambda$). In this situation the phase of the electromagnetic field can be considered as constant over the entire particle volume and the spatial distribution of the radiation can be calculated in this simplified problem. The time dependence can then be added subsequently once the spatial solution is known. This theory describes appropriately the optical properties till dimensions of around 100nm. According to this theory the external and internal electric field can be expressed as^[123]:

$$E_{in} = \frac{3\varepsilon_m}{\varepsilon + 2\varepsilon_m} E_0 \quad (2.5)$$

$$E_{ext} = E_0 + \frac{3n(\mathbf{n}\cdot\mathbf{p}) - \mathbf{p}}{4\pi\varepsilon_0\varepsilon_m r^3} \quad (2.6)$$

Where p is dipole moment, ε_m is the material permittivity, ε_0 is the vacuum permittivity, n the complex refractive index and r the particle radius. The two equations highlight that the resonance enhancement arise both for the electric field.^[123] A closer look on equation (2.6) highlights also that the amount of the external amplification depends on the nanoparticle size. The gain factor for noble metals is in the range of 10^2 - 10^4 .^[124] Physically the resonance can be understood as the result of the presence of a curved surface acting as a restoring force on the moving electrons. Indeed, this force keeps the charge confined in the nanoparticle during the oscillation, creating a resonance motion, which in turns leads to the electric field amplification inside and in the near vicinity of the surface. This amplification is the responsible for the nonlinear response enhancement on the non-centrosymmetric materials place in close vicinity to the metallic one.^[123] A representation of this effect can be seen in Figure 2.9.

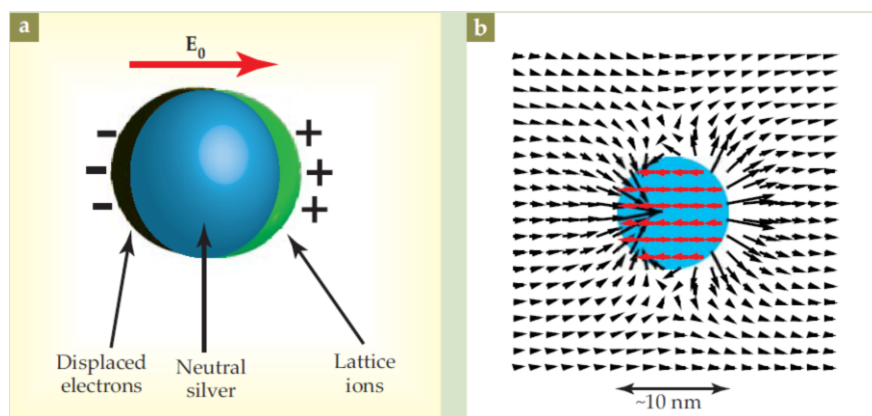


Figure 2.9: Schematic illustration of the electric field in the vicinity of a spherical silver nanoparticle with 10 nm diameter with resonant excitation. a) Electric field E_0 displacement on a 10 nm diameter silver sphere. The displacement is periodical with respect to the lattice, resulting in an oscillating electron density, i.e. the creation of the localised surface plasmon. b) The electronic oscillation greatly amplifies the electric field (black arrows) on the opposite site of the direction of E_0 . These calculations are done for the exemplary resonant photon of 3.5 eV which in addition shows that the internal field (red arrows) is constant and on the same order of magnitude of the external field located on the sphere surface.^[124]

For dimensions larger than 100 nm the quasi-static approximation fails and the complete Mie theory has to be applied. In this framework the amplification of the electric field becomes more complex to compute compared to equation 2.5 and 2.6 and a dependence on the external wavelength appears. In particular this theory predicts that nanoparticles larger than 100 nm experience a red-shift and a broadening of the resonance. The results shows also that the LSPs spectral dependence depends also on the nanoparticle geometry. The case used in this work is even more complex to model because several randomly oriented nanoparticles are inserted in one of the LiNbO₃ pore. In this situation the nanoparticles are interacting each others broadening and shifting the resonance position and affecting the final field enhancement in an unpredictable way.^[123]

2.4.1.5. Limitations of conventional methods to generate thin films of LiNbO₃

Classical patterning techniques, which can be employed to manufacture thin patterned LiNbO₃ films, are either serial and limited regarding their throughput (direct laser writing) or they comprise the use of photoresists as well as complex pattern transfer steps by

etching (mask-based methods such as photolithography) or layer transfer.^[125] Up to now, it has remained challenging to lithographically deposit LiNbO_3 precursor formulations by parallel additive patterning methods described in section 2.2.^[50,92,126] Moreover, it would be desirable to use environmentally friendly aqueous precursor formulations for this purpose. So far, thin LiNbO_3 films were prepared from aqueous precursor solutions using, for example, lithium and niobium alkoxides^[11] or niobic acid and lithium hydroxide^[12] as lithium and niobium sources. Another water-based synthesis route comprises the reaction of peroxy-polyniobic acid obtained from H_2O_2 and NbC with LiOH.^[13] However, often precursors are used that are either relatively expensive and difficult to handle, or the production of the precursor solutions is complex, so that upscaling is a challenge. Some aqueous LiNbO_3 precursor solutions are not suitable for the generation of thin LiNbO_3 layers on functional substrates because they involve the use of aggressive reagents, such as strong inorganic acids and bases or strong oxidants and reactants, which potentially harm the substrates.

2.4.2. Properties of NiFe_2O_4 and thin-layer configurations of solvothermal products

2.4.2.1. Crystal structure and magnetic properties of NiFe_2O_4 bulk material and nanoparticles

Nickel ferrite thin films are of great importance in research because of their physical properties. Due to its low conductivity (compared to metal films) and its magnetic properties, it is used in magnetic recording, high-frequency microwave devices and many other areas^[127,128]. Nickel ferrite crystallizes in the cubic crystal system in which the ions form an inverse spinel. The nickel ferrite can be represented with the following formula: $(\text{Fe}^{3+})_A[\text{Ni}^{2+}\text{Fe}^{3+}]_B\text{O}_4^{2-}$, where A describes the tetrahedral and B the octahedral sites^[127]. Figure 2.10 shows the spinel structure of the nickel ferrite.^[129]

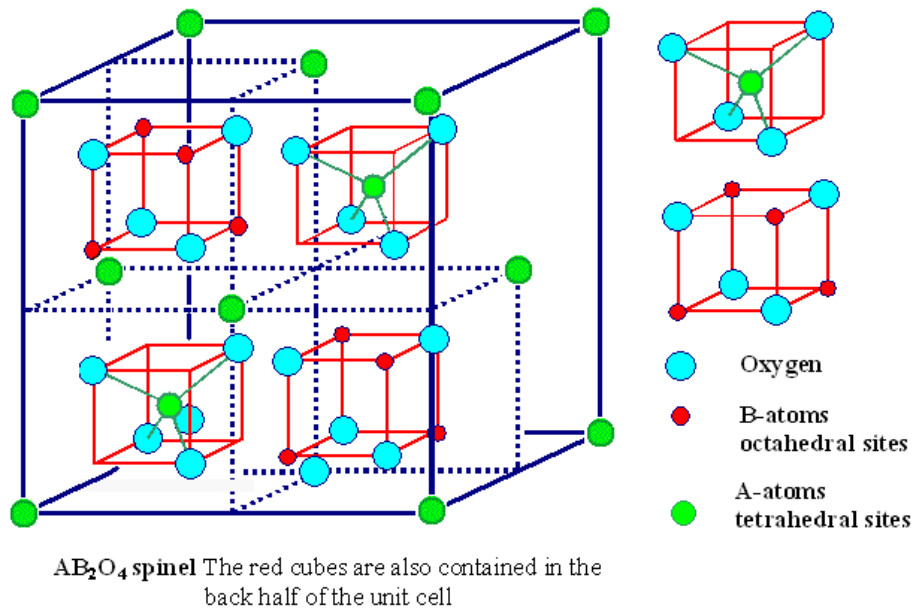


Figure 2.10: Inverse spinel structure of nickel ferrite.^[129]

Nickel ferrite is ferrimagnetic and belongs to the soft magnetic ferrites. Ferrimagnetism differs from ferromagnetism in the antiparallel, but quantitatively unequally distributed magnetic order of the elementary magnets in the Weiss domains. The oppositely aligned spins of paramagnetic ions are only partially compensated. The magnetisations of two neighbouring elementary magnets therefore only partially cancel each other out. The macroscopic behaviour is thus a weaker form of ferromagnetism. Figure 2.11 shows the three basic forms of the magnetic order.^[130,131]

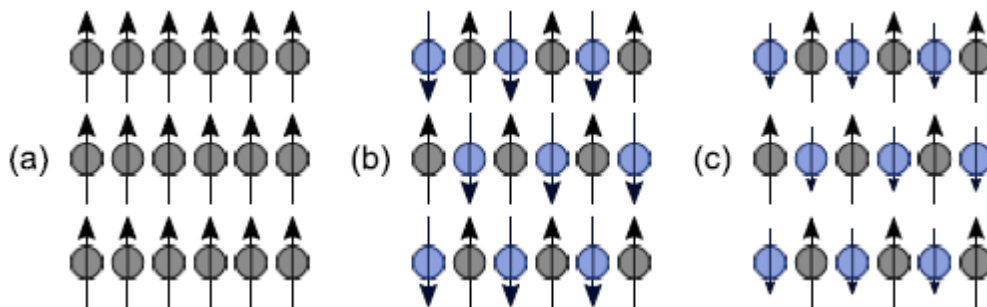


Figure 2.11: Schematic representation of the three basic forms of magnetic order. (a) Ferromagnetism - all magnetic moments are aligned in the same way. (b) Antiferromagnetism - The magnetic moments are in opposite directions spread and cancel each other out. (c) Ferrimagnetism (nickel ferrite) - The magnetic moments are divided in opposite directions with different amounts.^[132]

The magnetic properties of nickel ferrite also depend on the particle size. Brook et al ^[133] reported on superparamagnetic behavior in the case of polycrystalline nickel ferrite with a particle size of less than 10 nm and a ferrimagnetic behavior with a particle size greater than 15 nm. Figure 2.12 shows a schematic representation of the hysteresis curves of ferri- and superparamagnetic materials.

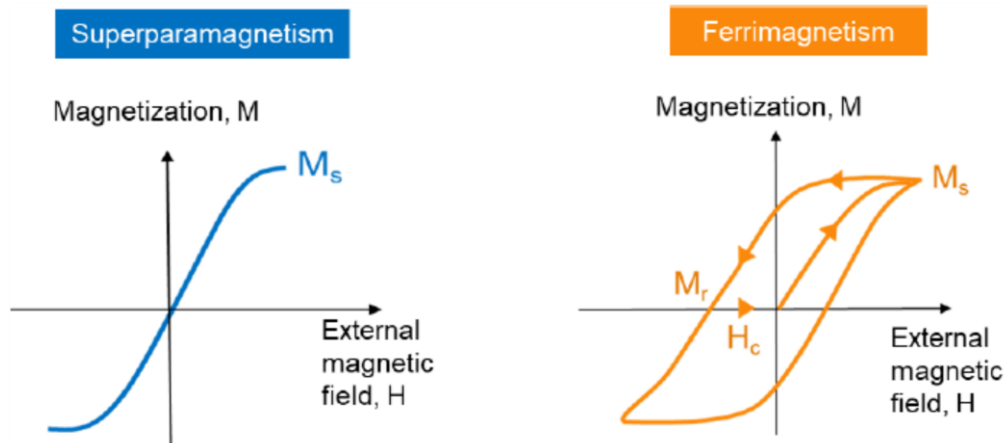


Figure 2.12: schematic representation of the hysteresis curves of ferri- and superparamagnetic materials.^[134]

For ferrimagnetic materials a magnetic moment results in each Weiss district. Since these magnetic moments are aligned uniformly in all directions over the entire crystal, the crystal does not show any magnetic properties towards the outside. However, if the crystal is brought into an external magnetic field, it is possible to align all magnetic moments. This gives a macroscopic magnetic moment, which is also retained when the external magnetic field is removed (see Figure 2.12). Above a specific temperature for each compound, the Néel temperature, the entire magnetic structure is lost and the compound shows paramagnetic behavior.^[130,135] For superparamagnetic materials, on the other hand, there is no permanent magnetization when the external magnetic field is switched off. In detail, the Néel relaxation takes place through thermal excitations. Here, the magnetic moments of the particles are repeatedly changed by thermal influences (without the influence of a magnetic field). The time within which the magnetic moment rotates is also known as the Néel relaxation time. Since the time in which the magnetization is measured

takes longer than the Néel relaxation and the changing magnetic moments in the measurement compensate each other, the magnetization seems to have the value 0 on average. A collection of such particles behaves macroscopically like a paramagnet, but still has the high magnetic saturation of a ferromagnet. In contrast to a paramagnet, it is not individual atoms that change their direction of magnetization independently of one another, but rather small magnetic particles.^[136]

Thin films of NiFe₂O₄ are typically produced using a variety of deposition techniques such as pulsed laser deposition^[137], sputtering^[133], or sol-gel methods.^[137,138] Nickel ferrite thin films possess unique magnetic properties, such as high coercivity and good thermal stability, which make them suitable for a range of applications including magnetic data storage, microwave devices, and magnetic sensors.^[139]

In recent years, there has been increasing interest in developing nickel ferrite thin films with tailored properties through the use of different synthesis and deposition methods, as well as post-treatment techniques such as annealing or doping with other elements.^[128,139]

Overall, nickel ferrite thin films are a promising class of materials for various technological applications due to their unique magnetic properties and the ability to control their properties through various synthesis and processing methods.

2.4.2.2. Limitations of conventional lithographic methods for solvothermal synthesis

While the generation of continuous thin films of solvothermal reaction products^[33] and the further processing of such films by standard lithography under ambient conditions^[34] have been established, direct lithographic patterning of substrates with solvothermal reaction products has remained challenging. However, in this way the integration of solvothermal reaction products into device components with complex architectures beyond simple thin-layer configurations would become possible. Moreover, orthogonal substrate functionalization^[9] could then yield device components exhibiting complementary or synergistic properties of solvothermal reaction products and a second functional material.

It is conceivable to pattern substrates with solvothermal reaction products by subtractive lithography comprising the transfer of a continuous layer of the solvothermal reaction product by methods such as wafer bonding or ion slicing onto the substrate to be patterned, additional deposition of a resist, pattern generation using masks or writing processes and finally pattern transfer into the continuous layer of the solvothermal reaction product by dry or wet etching. It is also conceivable to employ continuous donor layers of solvothermal reaction products for additive patterning of acceptor substrates by LIFT.^[70] However, ensuring sufficient adhesion of solid solvothermal reaction products deposited by ballistic transfer might be challenging. The combination of solvothermal syntheses and *in situ* additive substrate patterning under solvothermal conditions by state-of-the-art lithography is either demanding or even impossible. The serial additive lithographic methods as well as parallel additive lithographic methods described in section 2.2 would enable the deposition of precursors of solvothermal reaction products on counterpart substrates.^[50,92,126,140,141] However, while some efforts were directed to the utilization of tip-induced organic reactions during parallel scanning probe lithography under ambient pressure and temperature,^[142] faithful conversion of precursor patterns into patterns of solvothermal reaction products has remained an unsolved scientific problem.

2.4.3. Properties of PFcMA and on-demand production of tailored surfaces with switchable wettability

2.4.3.1. Syntheses and properties of PFcMA

Poly(2-(methacryloyloxy)ethyl ferrocenecarboxylate), or PFcMA, is a redox-active polymer that contains ferrocene groups. Ferrocene is a sandwich-type organometallic compound consisting of two cyclopentadienyl rings bound to a central iron atom. The ferrocene group within PFcMA serves as an electroactive site that undergoes reversible oxidation and reduction reactions. PFcMA can be synthesized through radical polymerization of 2-(methacryloyloxy)ethyl ferrocenecarboxylate (FMA) monomers. An initiator such as azobisisobutyronitrile (AIBN) or $[\text{Cu}^{\text{I}}(\text{PMDETA})\text{Br}]$ is used to generate

free radicals that initiate the polymerization (Figure 2.13).^[45,143]

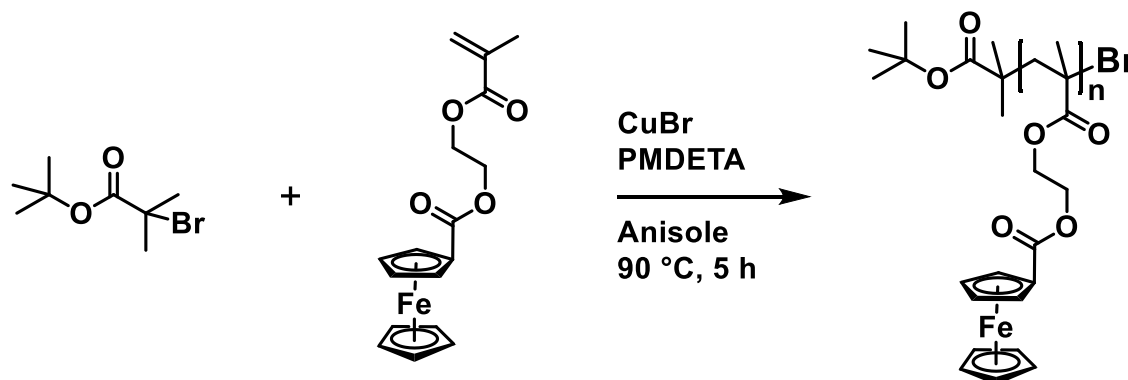


Figure 2.13: Exemplary synthesis of PFCMA in anisole by using $[\text{Cu}^{\text{I}}(\text{PMDETA})\text{Br}]$ as initiator.^[143]

Due to its redox-active nature, PFCMA exhibits interesting properties such as electrochromism, where the color of the polymer changes upon application of an electrical potential, and electroactivity, where the polymer can be used as an electrode material for energy storage applications. PFCMA has been utilized for the creation of redox-responsive materials that can undergo reversible structural changes when the redox state of the ferrocene groups is altered; these ferrocene groups undergo a rapid and reversible redox reaction, resulting in a local polarity change and remarkable swelling behavior upon ferrocene moieties oxidation. These materials have potential applications in areas such as drug delivery and sensing. Overall, PFCMA is a versatile polymer with unique electroactive properties that make it a promising material for a range of applications in fields such as electrochemistry, materials science, and biomedical engineering.^[45,143–145]

2.4.3.2. Lithographic transfer of highly viscous, stimuli-responsive polymers

Additive lithographic deposition of functional polymers including stimuli-responsive polymers^[146] is frequently applied to produce functionalized surfaces. Classical additive lithographic methods including inkjet and aerosol jet printing^[140] as well as soft lithography^[92,126] and polymer pen lithography^[50,141,147] are not compatible with the

lithographic transfer of highly viscous or solidified polymers. To overcome this problem, polymer solutions in volatile organic solvents are used as inks. The presence of volatile organic solvents during the stamping process reduces the amount of non-volatile functional polymer per stamping step. Moreover, during the evaporation of volatile organic solvents hardly controllable structure formation processes such as liquid-liquid phase separation may occur.^[148] When transferring functional polymers to substrates using methods such as laser-induced forward transfer, sufficient adhesion might be difficult to realize. Due to the fact that melt processing of polymers by extrusion or electrospinning^[149] is well established, direct additive lithographic transfer of polymer melts without organic solvents would be an extremely attractive approach for surface manufacturing, mainly because the process is straightforward and no expensive equipment is required.

2.5. Wetting on smooth and rough surfaces

Wetting describes the behavior of liquids in contact with the surface of solids, which depend on intermolecular and electrostatic interactions between the two phases and wettability is the associated property of the solid surface.^[150] Depending on the type of liquid, the material the surface is made of and its nature, for example in terms of roughness, the liquid wets the surface to a greater or lesser extent, resulting in a high or low contact angle of the liquid on the surface of the solid.^[151] To determine if a drop spreads on a surface, the cohesive and adhesive forces were compared. If the adhesive forces are significantly greater than the cohesive forces, the drop will completely wet the surface.^[150]

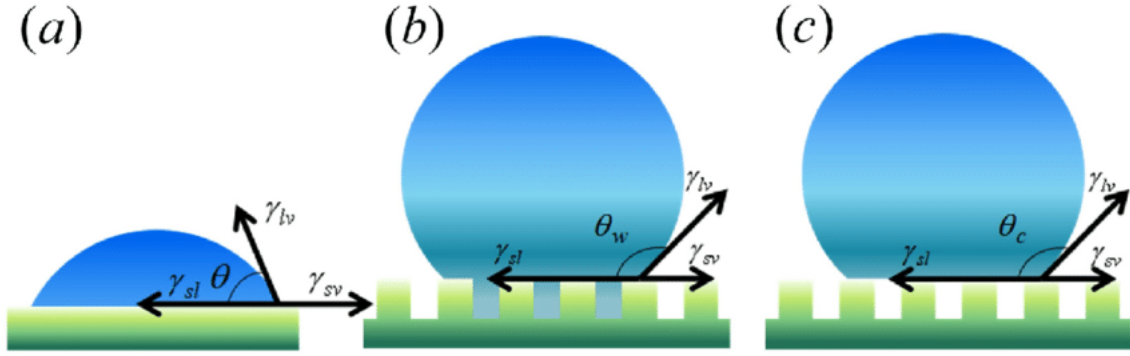


Figure 2.14: Model representation of a liquid drop on a solid surface by a) Young, b) Cassie-Baxter and c) Wenzel.^[152]

The Young equation applies to three-phase systems in thermodynamic equilibrium for ideal solids and pure liquids. On the edge of one sessile drop is a three-phase point at which the liquid, the solid and air meet.^[153,154] Young's equation

$$\cos \theta = \frac{(\gamma_{SV} - \gamma_{SL})}{\gamma_{LV}} \quad (2.7)$$

establishes a relationship between the free specific surface energy γ_{SV} of a flat solid to the surrounding gas, the specific interfacial energy γ_{SL} between the solid and a drop of liquid on it, the surface tension γ_{LV} of the liquid to the surrounding gas and the contact angle θ .^[153,155–157]

Rough or finely structured surfaces offer an additional interface for liquid spreading, which leads to a change in the contact angle, whereby the wetting of the liquid can be homogeneous (Wenzel) or heterogeneous (Cassie Baxter).^[158] According to Wenzel's model^[159], the drop penetrates all the recesses of the structure and completely covers the rough surface. Accordingly, the contact angle θ_w depends on the roughness factor, which is the ratio of the actual surface to the associated smooth surface. It results from the angle θ of the smooth surface described by equation (2.8):

$$\cos \theta_w = r \cdot \cos \theta \quad (2.8)$$

Eq. 2.8 shows that the rough surface makes hydrophilic surfaces ($\theta < 90^\circ$) even more hydrophilic and hydrophobic ($\theta > 90^\circ$) even more hydrophobic.^[160,161]

In the Cassie-Baxter model^[162], on the other hand, the heterogeneously wetting drop lies only on the peaks of the surface structure and thus hovers over the valleys, so that the

liquid only comes into contact with the bumps of the rough surface. The Cassie-Baxter equation

$$\cos\theta_{CB} = f_1 \cdot \cos\theta - f_2 \quad (2.9)$$

describes the dependence of the Cassie-Baxter angle on the surface proportions of water, air and substrate (f_1 : water-substrate, f_2 : air-substrate, $f_1 + f_2 = 100\%$). Here too, the rough surface makes hydrophobic/hydrophilic surfaces even more hydrophobic/hydrophilic.^[163,164]

Alternative criteria for the Cassie-Baxter state are: contact line forces must exceed gravity, and the surface features must be long enough to prevent the formation of bridges to the base.^[165] The dependence of contact angles on heterogeneous solid surfaces on the surface and interfacial tensions of the involved fluid phases (the wetting liquid and another fluid phase such as a surrounding gas) and the wetted solid surface is controversially discussed.^[166,167] For example, McCarthy and co-authors argue that contact angles are determined by the properties of the three-phase contact line between the involved fluid phases and the solid surface.^[168,169]

Two limiting cases, the constant contact angle (CCA) mode and the constant contact radius (CCR) mode, were identified for the evaporation of sessile drops.^[170] The CCR mode is naturally associated with contact line pinning, that is, the temporary immobilization of the three-phase contact line between solid substrate, liquid and gas phase. On chemically and/or topographically patterned substrates, pronounced contact line pinning was experimentally observed^[171–174] and theoretically predicted^[174–176] in different scenarios involving changes in the volume of the wetting liquid.

2.6. Wettability Switching

Wettability switching of surfaces refers to the ability to change the surface energy and alter the wetting behavior of liquids on the surface. One approach to achieve wettability switching is by modifying the surface chemistry of the substrate. This can be achieved by using various techniques such as plasma treatment, chemical functionalization, and

deposition of self-assembled monolayers (SAMs). The modification of surface chemistry can lead to changes in the surface energy and the formation of specific functional groups that alter the interaction of the surface with liquids.^[177,178]

Another approach to achieve wettability switching is by using responsive materials that can undergo changes in their properties in response to an external stimulus, such as temperature, light, pH, or electric field. For example, some polymers can change their surface energy and wettability in response to changes in temperature or pH. Polymer brushes, where the polymer chains are tethered to a surface, can also be used to tune the wettability of surfaces.^[143,179,180]

One specific class of materials that can switch their wettability through reduction and oxidation are ferrocene-containing polymers. These polymers have been shown to exhibit reversible switching of surface wettability upon application of a redox potential. In the oxidized state, the polymers exhibit hydrophobic behavior with a high contact angle, while in the reduced state, the polymers become hydrophilic with a low contact angle.^[45,143] Overall, wettability switching of surfaces is an important area of research with potential applications in various fields, including microfluidics, biomedical devices, and anti-fouling coatings.^[38,39,41]

3. Thin patterned lithium niobate films by parallel additive capillary stamping of aqueous precursor solutions

3.1. Introduction

Thin micropatterned lithium niobate (LiNbO_3) layers may be used for photonic components, actuators and data storage devices because LiNbO_3 exhibits nonlinear optical properties as well as anisotropic polarizability and ferroelectric behavior.^[11,101] Commonly, thin micropatterned LiNbO_3 layers are integrated into device architectures by complex manufacturing algorithms including direct wafer bonding, mechano-chemical wafer thinning or mechanical cleavage of thin LiNbO_3 layers from bulk LiNbO_3 crystals, as well as lithographic patterning of and/or pattern transfer into the thin LiNbO_3 layers.^[13,17] The high-throughput generation of thin microstructured LiNbO_3 layers was achieved by parallel additive capillary stamping of environmentally friendly aqueous LiNbO_3 precursor solutions with topographically patterned porous polymer stamps. The precursor solutions contain the cheap, commercially available compounds lithium acetate and niobium oxalate hydrate, which are simply dissolved in water as received. In this way, rough surfaces not suitable for layer transfer methods involving direct wafer bonding, such as the surfaces of ITO substrates, are functionalized with microstructured LiNbO_3 layers. Microstructured holey 100 nm thick LiNbO_3 films showing uniform second-harmonic generation (SHG) except at the positions of the holes are obtained. Orthogonal substrate formation is demonstrated by electrodeposition of gold into the holes, which increases the SHG output 5.4 times.

3.2. Experimental section

3.2.1. Materials and chemicals

Macroporous silicon containing pores with a diameter of 1 μm and a depth of 800 nm arranged in hexagonal arrays with a lattice constant of 1.5 μm was purchased from SmartMembranes GmbH (Halle an der Saale). Sylgard 184 formulation supplied by Dow Corning was used for the preparation of negative polydimethylsiloxane (PDMS) replicas of macroporous Si. Gold chloride (AuCl_3), L-Cystein ($\text{C}_3\text{H}_7\text{NO}_2\text{S}$) and indium tin oxide

substrates ($(\text{In}_2\text{O}_3)_{0.9} \cdot (\text{SnO}_2)_{0.1}$ with a resistance of $8\text{-}12 \Omega \text{ sq}^{-1}$ and a thickness of $1200\text{--}1600 \text{ \AA}$) were purchased from Sigma Aldrich. Lithium acetate ($\text{C}_2\text{H}_3\text{LiO}_2$) and niobium oxalate hydrate ($\text{C}_{10}\text{H}_5\text{NbO}_{20} \cdot 6\text{H}_2\text{O}$) were purchased from Alfa Aesar. Sulfuric acid (0.5 mol L^{-1}) was purchased from Carl Roth GmbH. Perfluorodecyltrichlorosilane ($\text{C}_{10}\text{H}_4\text{Cl}_3\text{F}_{17}\text{Si}$) was purchased from abcr GmbH, Karlsruhe. PS-*b*-P2VP (M_n (PS) = $110,000 \text{ g/mol}$; M_n (P2VP) = $52,000 \text{ g/mol}$; PDI = 1.10) was purchased from Polymer Source. Tetrahydrofurane ($\text{C}_4\text{H}_8\text{O}$) was purchased from Berndt Kraft GmbH. Pt wires were purchased from Rettberg Glasapparatebau and Ag/AgCl electrodes ($c(\text{KCL}): 3 \text{ mol L}^{-1}$) from Metrohm.

3.2.2. Stamp fabrication

The following figure illustrates the schematic for the production of the PS-*b*-P2VP stamp and the stamping process.

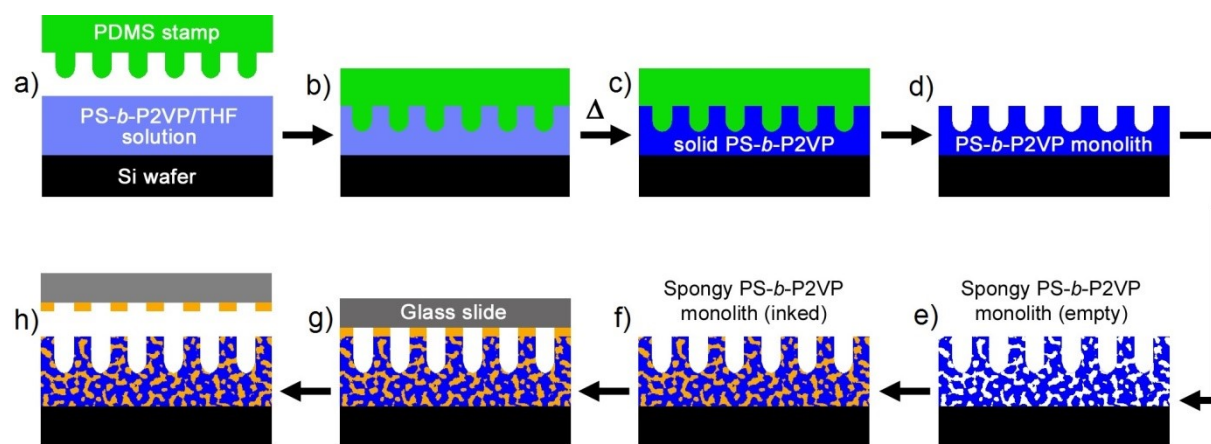


Figure 3.1: Scheme for the fabrication of the macro- and mesoporous PS-*b*-P2VP stamp and the stamping process.^[77]

The macroporous silicon was first treated with oxygen plasma for 10 minutes using Diener Femto plasma cleaner and then coated with $\text{C}_{10}\text{H}_4\text{Cl}_3\text{F}_{17}\text{Si}$ at $100 \text{ }^\circ\text{C}$ for 10 h by chemical vapor deposition adapting procedures reported elsewhere.^[181] A PDMS negative of the surface-modified macroporous silicon used as secondary mold was prepared as follows. Sylgard 184 prepolymer and crosslinker were mixed at a mass ratio of 10:1,

stirred, degassed in a vacuum, poured onto the surface-modified macroporous silicon, cured for 12 h at 70 °C and detached. In the next step, 10 μL of a solution containing 0.1 g mL^{-1} PS-*b*-P2VP in THF were dropped onto a flat silicon wafer, and the THF was allowed to evaporate under ambient conditions. The PDMS negatives were molded against the viscous PS-*b*-P2VP films obtained in this way under a pressure of 3.9 kN m^{-2} and under a vacuum at 200 °C for 10 h (heating and cooling rates amounted to 20 K min^{-1}). As a result, PS-*b*-P2VP monoliths with a thickness of $\sim 3 \mu\text{m}$ and with topographically structured surfaces were obtained, which were negatives of the PDMS secondary molds and positives of the macroporous silicon. Both the PDMS secondary molds and the topographically patterned PS-*b*-P2VP monoliths extended approximately 1 cm^2 . To generate spongy mesopore systems, the PS-*b*-P2VP monoliths were swelled in ethanol for 30 min at 70 °C.

3.2.3. Preparation of holey LiNbO_3 films

20 μl of a precursor solution containing 0.491 g (7.44 mmol) lithium acetate and 1.664 g (2.57 mmol) niobium oxalate hydrate per 50 mL water was dropped onto the porous PS-*b*-P2VP stamps. After a wait time of 1 min, excess precursor solution was removed with tissue. The PS-*b*-P2VP monoliths were glued with double-sided adhesive tape onto a stainless-steel pin with a mass of 40 g (Figure 3.2).

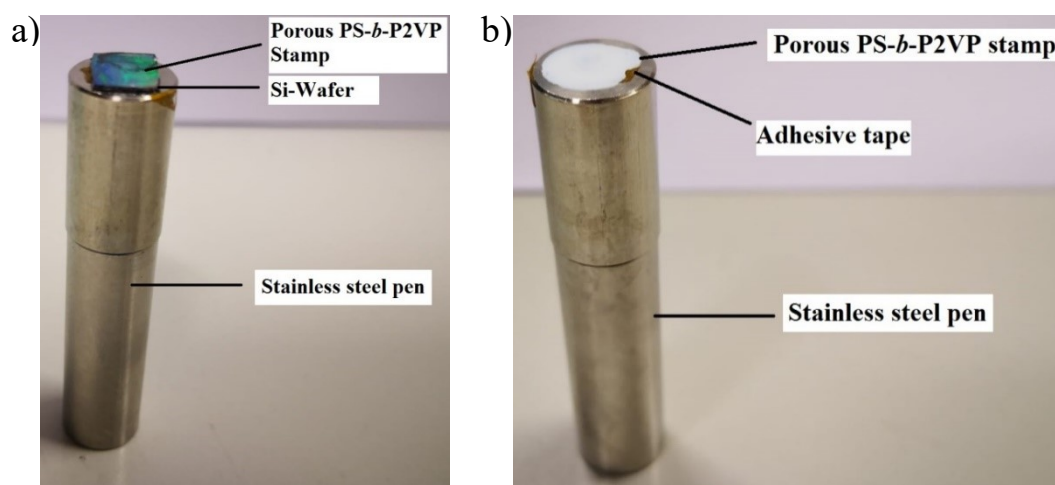


Figure 3.2: Configurations used for capillary stamping. a) Porous PS-*b*-P2VP stamp attached to a silicon wafer glued onto a stainless-steel pin; b) free-standing porous PS-*b*-

P2VP stamp directly glued onto a stainless-steel pin.

ITO substrates were modified with $C_{10}H_4Cl_3F_{17}Si$ in the same way as the macroporous silicon templates. Capillary stamping was carried out with a contact time of 3 s and under a pressure of 3.9 kN m^{-2} . The stamped samples were heated at a rate of 20 K min^{-1} to $600 \text{ }^\circ\text{C}$, kept at this temperature for 10 h and cooled to room temperature at a cooling rate of -200 K h^{-1} . The annealing procedure was carried out in air.

3.2.4. Electrochemical deposition of gold

Gold was deposited at the positions of the holes of the microstructured $LiNbO_3$ films by electrodeposition using the setup displayed in Figure 3.3.

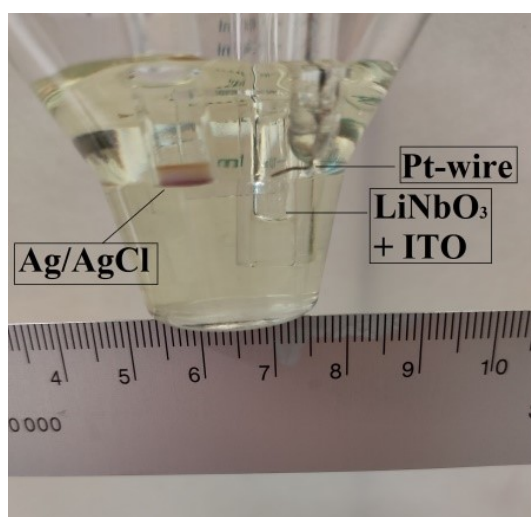


Figure 3.3: Setup for the electrodeposition of gold on ITO. The ITO substrate acted as working electrode, a platinum wire as counter electrode and an Ag/AgCl electrode as reference electrode.

The ITO substrate acted as working electrode (the $C_{10}H_4Cl_3F_{17}Si$ coating degraded during the calcination step), a platinum wire as counter electrode and an Ag/AgCl electrode as reference electrode. The plating solution consisted of 303.33 mg (1 mM) $AuCl_3$ and 12.12 mg (0.1 mM) L-cystein dissolved in 20 ml of a 0.5 M H_2SO_4 solution.^[182] The electrodeposition was carried out at a constant voltage of 0 V *versus* Ag/AgCL for 600 s using a potentiostat Interface 1000 (Gamry).

3.2.5. Characterization

3.2.5.1. Contact angle measurements

Contact angles were measured applying the sessile drop method with a DSA100 drop shape analyzer at 23 °C and a relative humidity of 34 %. The LiNbO₃ precursor solution was applied to 6 different places on ITO substrates modified with C₁₀H₄Cl₃F₁₇Si.

3.2.5.2. X-ray diffraction (XRD)

Theta-theta scans were carried out with Cu K α radiation using an X'Pert Pro MPD diffractometer (PANalytical) equipped with a rotating sample plate and a PixCel 1D detector. The diffractometer was operated at a voltage of 40 kV and a current of 30 mA.

3.2.5.3. GIXRD measurement

An ITO substrate was investigated as received. Since the areas of the microstructured LiNbO₃ films generated on ITO substrates by capillary stamping are too small for GIXRD measurements, a thin-film sample completely covering an ITO substrate extending 3 x 1 cm² by spin-coating were prepared. 0.491 g (7.44 mmol) lithium acetate and 1.664 g (2.57 mmol) niobium oxalate hydrate were dissolved in 50 mL water. 300 mg hydroxypropyl cellulose (HPC, purchased from Alfa Aesar, M_w : 100.000 g/mol) was dissolved in 10 ml of the solution under stirring. After stirring for 2 h, a homogeneous liquid mixture was obtained. The ITO substrate was completely wetted with the homogeneous liquid mixture and then rotated for 30 seconds at 2000 rpm using a Spincoat G3P-8 from Specialty Coating Systems. The coated ITO substrates were heated at a rate of 20 K min⁻¹ to 600 °C, kept at this temperature for 10 h and cooled to room temperature at a cooling rate of -200 K h⁻¹. The annealing procedure was carried out in air. The LiNbO₃ film had a thickness of 150 nm, as determined by AFM.

GIXRD measurements were carried out with a PANalytical X'Pert Pro MRD diffractometer equipped with a Eulerian cradle and a PIXcel detector using Cu K α radiation ($\lambda = 0.15418$ nm). The diffractometer was operated at a voltage of 40 kV and a

current of 40 mA. The θ angle between incident X-rays and sample surface was fixed to 1° . The 2θ angle was varied from 10° to 80° with a step size of 0.02° and an integration time of 2 s.

3.2.5.4. Scanning electron microscopy (SEM)

The samples were dried overnight at 40°C under ambient conditions, glued onto a sample holder and sputter-coated 2-3 times for 15 s with platinum/iridium alloy. The images were recorded at an acceleration voltage of 3 kV and at a working distance of 5 mm using a Zeiss Auriga device equipped with a field emission cathode and a Gemini column. The images were captured with an InLens detector.

3.2.5.5. Atomic force microscopy (AFM)

AFM topography images were recorded in the tapping mode with a NTEGRA microscope (NT-MDT) using HQ:NSC16/AL BS cantilevers obtained from μmasch .

3.2.5.6. Nonlinear imaging

The setup consisted of a laser scanning microscope FV3000 (Olympus) optically combined with a regeneratively amplified femtosecond laser (Pharos-HE-20, Light Conversion Inc.) described in detail elsewhere.^[183] The fs laser acts as a pump source for an optical parametric amplifier (OPA) (Orpheus-Twins F, Light Conversion). The fs pulses are adjusted collinearly to the optical path of the integrated continuous lasers in the microscope scanning unit. A UPLSAPO 60x water immersion objective with a numerical aperture of 1.2 was used. The focal point was diffraction-limited and had a diameter of ≈ 500 nm. For transmission CLSM the scanning light of a continuous laser at 640 nm was collected *via* a condenser lens and redirected to a photomultiplier (PMT). For SHG imaging an excitation wavelength of 1000 nm (emission wavelength 500 nm) applying a time-average power at the exit of the optical parametric amplifier of 1.3 mW, a repetition rate of 100 kHz and a pulse duration of 180 fs was used. The SHG images are

the average of 16 successive scans of the same area acquired with a pixel dwell time of $80 \mu\text{s pixel}^{-1}$. For light detection in reflection and transmission a PMT was used.

3.2.5.7. Optical set up for non-linear spectroscopy

The optical setup used for the spectroscopic evaluation of the SHG is shown in Figure 3.4.

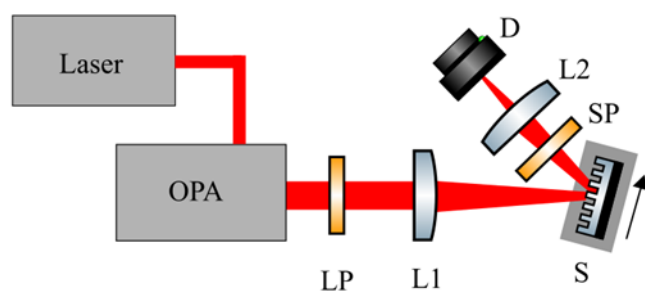


Figure 3.4: Sketch of the optical setup used for nonlinear spectroscopy. A femtosecond laser acts as the source for an optical parametric amplifier (OPA). The light passes through a longpass filter (LP) to clean the residual light of the OPA. Then, it is focused via a lens (L1) on the sample (S). The sample can be moved along the direction marked by the arrow and in the orthogonal direction. The emitted light is then filtered from the fundamental via a short pass filter (SP) and focused via another lens (L2) on the detector (D).

The same fs laser as for SHG mapping was used as a pump source for the OPA Orpheus F (Light Conversion). The laser was focused with a lens (L1) having a focal length of 2000 mm and placed at a distance of 14 cm from the sample (S) surface. The sample was mounted on a manual translational stage, which can be moved as indicated by the arrow in the Figure 3.4 and in addition perpendicularly to the optical table. The residual radiation of the laser system was suppressed with a long pass filter (LP) (cut wavelength of 600 nm) inserted in the beam path between the OPA and lens L1. The zero order of the diffracted light from the sample was collected by the spectrometer (D) QE Pro (Ocean Optics) after filtering by a short pass filter (SP) with a cut wavelength at 525 nm and refocused by another lens (L2) (focal length = 25 mm). The laser repetition rate was set to 12.5 kHz, which corresponded to an average power of 227 mW at the sample position. This power setting prevents radiation damage of the sample. The spectrometer integration

time was set to 500 ms.

3.3. Results and discussion

3.3.1. Pore generation

After structuring, the PS-*b*-P2VP stamp is swollen in ethanol at 70 ° C for 30 min in order to generate a spongy, continuous pore system. The osmotic pressure drives the ethanol molecules into the P2VP domains. The P2VP blocks thereby adapt elongated conformations in order to maximize contact with the ethanol molecules. Because the P2VP domains swell and increase in volume, the morphology of the glassy PS matrix is reconstructed. After the evaporation of the ethanol, an entropic collapse of the stretched P2VP blocks occurs, which relax back to their primary coil-like conformation, while the glassy PS matrix fixates on the changed morphology. Thus, a continuously mesoporous and spongy system is generated.^[77] Figure 3.5 shows SEM images of the mesoporous, spongy PS-*b*-P2VP stamp with hexagonally arranged macroporous holes.

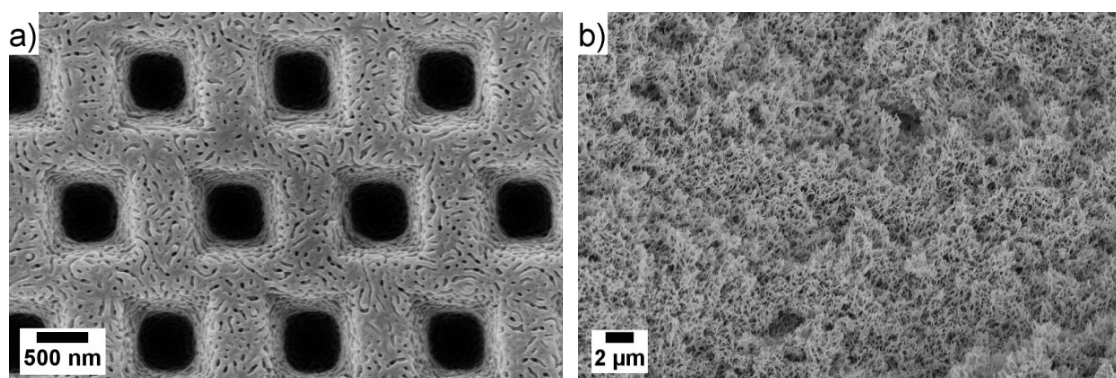


Figure 3.5: a) SEM images of the porous PS-*b*-P2VP stamps. a) Top view; b) cross-section.

3.3.2. Capillary stamping of aqueous LiNbO₃ precursor solutions onto ITO substrates

It is assumed that the stamping of the LiNbO₃ precursor ink used here with porous stamps having smooth contact surfaces without protruding contact elements will yield continuous films of the LiNbO₃ precursor ink. However, continuous films of the LiNbO₃ precursor

ink on hydroxyl-terminated substrates such as ITO^[184] are much easier accessible by spin coating or dip coating. The stamping process reported here was specifically devised so as to directly generate microstructured LiNbO₃ films on relatively rough substrates, as it is required for a broad range of device architectures.^[13–15,17]

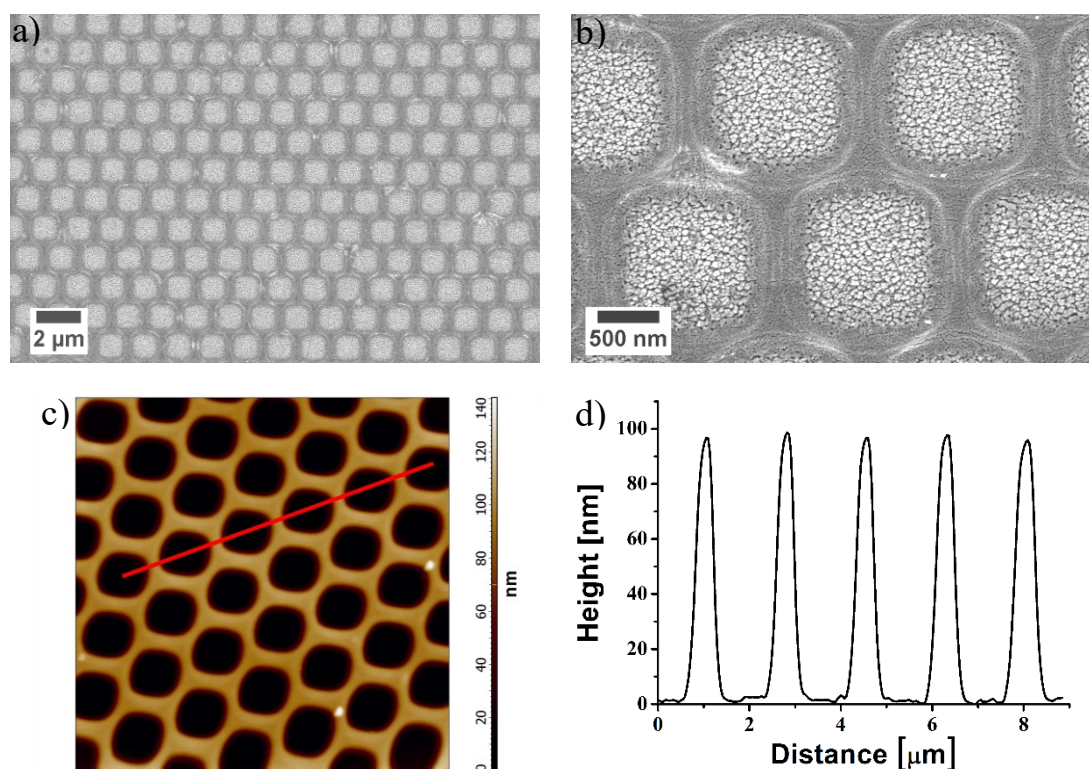


Figure 3.6: Holey LiNbO₃ films prepared by stamping aqueous precursor solutions containing lithium acetate and niobium oxalate hydrate onto an ITO substrate followed by calcination. a), b) SEM images showing LiNbO₃ rims surrounding holes, in which the grainy ITO surface is exposed. a) Overview, b) detail. c) AFM topography image extending 10 x 10 μm² of a holey LiNbO₃ film with a thickness of 100 nm on an ITO substrate. d) Topographic profile along the red line in panel c).

To stamp the aqueous LiNbO₃ precursor solution, porous stamps^[76,83] with a pore diameter of ~50 nm consisting of the block copolymer polystyrene-*block*-poly(2-vinylpyridine) (PS-*b*-P2VP) were used. Porous polymer stamps are compatible with automated stamping devices designed for polymer pen lithography,^[85] allow storage and replenishment with ink anytime during stamping and enable, therefore, efficient additive surface manufacturing. The porous PS-*b*-P2VP stamps had topographically patterned contact surfaces containing indentations arranged in hexagonal arrays with a lattice

constant of $\sim 1.5 \mu\text{m}$. Both the diameter and the depth of the indentations amounted to $\sim 800 \text{ nm}$ (Figure 3.5). Following procedures reported elsewhere,^[77] the porous PS-*b*-P2VP stamps were prepared by double replication molding of macroporous silicon (Figure 3.7),^[185] a classical two-dimensional photonic crystal with bandgaps for wavelengths in the infrared range.^[186]

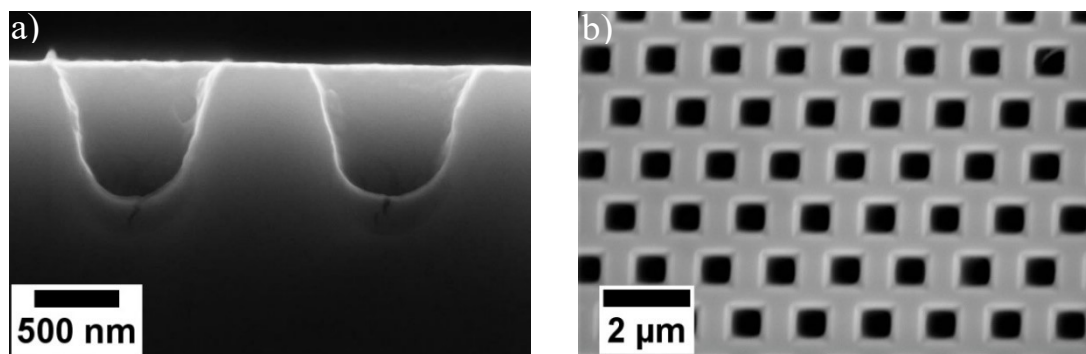


Figure 3.7: SEM images of macroporous silicon used as master template in the double-replication process yielding the porous PS-*b*-P2VP stamps seen in Figure 3.5. a) Top view; b) cross-sectional view.

Porous PS-*b*-P2VP stamps filled with the aqueous LiNbO_3 precursor solution were brought into contact with ITO substrates hydrophobically modified with 1h,1h,2h,2h-perfluorodecyltrichlorosilane ($\text{C}_{10}\text{H}_4\text{Cl}_3\text{F}_{17}\text{Si}$) for 3 s under a pressure of 3.9 kN m^{-2} (Figure 3.1). The contact angle of the LiNbO_3 precursor solution on surface-modified ITO substrates amounted to $74^\circ \pm 2^\circ$ so that spreading was prevented. Thus, the LiNbO_3 precursors were exclusively deposited in areas where the porous PS-*b*-P2VP stamps formed contact with the surface-modified ITO substrates.

3.3.3. Formation of micropatterned LiNbO_3 films on ITO substrates

Due to the hygroscopic properties of the lithium acetate used as lithium source, the stamped patterns were calcined in air immediately after stamping. The samples were heated to a target temperature of $600 \text{ }^\circ\text{C}$ at a rate to of 20 K per minute , kept at $600 \text{ }^\circ\text{C}$ for 10 h and cooled to room temperature at a cooling rate of -200 K min^{-1} . The thermal treatment also removed the $\text{C}_{10}\text{H}_4\text{Cl}_3\text{F}_{17}\text{Si}$ coating on the ITO substrates. In this way,

holey LiNbO₃ films consisting of LiNbO₃ rims with a width of ~400 nm enclosing circular areas with a diameter of ~1 μm were obtained, in which the grainy ITO substrate surface was exposed (Figure 3.6a,b). The circular holes were arranged in hexagonal lattices and had a center-to-center distance of ~1.5 μm. Thus, the LiNbO₃ patterns faithfully replicated the macroporous silicon master templates, that is, a photonic bandgap configuration well established in silicon photonics. The smallest typical LiNbO₃ waveguide structures are characterized by lateral dimensions in the 1 μm range. As obvious from Figure 3.6, LiNbO₃ micropatterns with this feature size can conveniently be generated by capillary stamping. The LiNbO₃ micropatterns produced here enable orthogonal substrate functionalization – the deposition of a second component with synergistic functionality into the holes of the LiNbO₃ micropatterns, where the surface of the ITO substrate is exposed. Of course, a corresponding design of the topography of the porous stamps contact surfaces allows stamping arbitrary lithium niobate patterns optimized for any envisaged application.

The nonlinear optical (NLO) properties of LiNbO₃ layers depend on their thickness. If the LiNbO₃ layers are too thin (below 100 nm), the overall NLO efficiency will be negligible. Typical thicknesses of lithium niobate layers obtained by crystal ion slicing range from 300 nm to 900 nm.^[17] AFM topography imaging revealed that the height of the LiNbO₃ rims of the micropatterned LiNbO₃ layers produced here amounted to ~100 nm (Figure 3.6c,d). As discussed below, even these 100 nm thick LiNbO₃ microstructures show the typical NLO properties of LiNbO₃, such as second harmonic generation (SHG). The thickness of the LiNbO₃ layers generated by capillary stamping and annealing is crucially influenced by the concentrations of the lithium and niobium sources in the ink. Reducing the concentrations to 75 % of the initial values used for capillary stamping of the micropatterned LiNbO₃ films seen in Figure 3.6 yields about 80 nm thick lithium niobate layers (Figure 3.8) that do no longer show significant NLO properties.

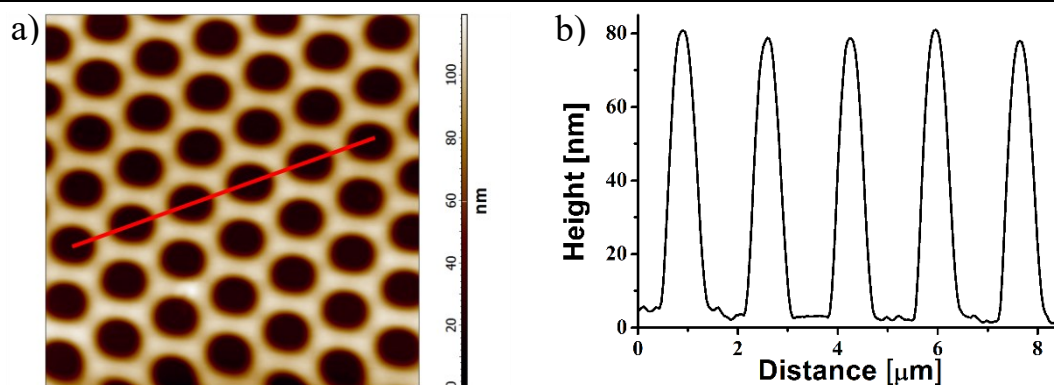


Figure 3.8: Holey LiNbO_3 film obtained by capillary stamping of an aqueous solution containing 0.368 g (5.58 mmol) lithium acetate and 1.248 g (1.928 mmol) niobium oxalate hydrate per 50 mL water. Therefore, the concentrations of the lithium and niobium sources were reduced to 75 % with respect to the concentrations used to produce the holey LiNbO_3 film displayed in Figure 3.6. Otherwise, the preparation procedures were exactly identical. a) AFM topography image. The area of the image field is $10 \times 10 \mu\text{m}^2$. b) Topographic profile along the line in panel a).

The surface of ITO substrates consists of reactive hydroxyl groups, the dehydroxylation of which is reversible.^[184] It is, therefore, reasonable to assume that the forming LiNbO_3 finds abundant anchoring sites on the surfaces of the ITO substrates. Moreover, the large real surface areas of the ITO substrates related to their rough surface topography supports strong adhesion between the LiNbO_3 layer and the ITO substrates (in contrast to the extremely smooth surfaces required for all layer transfer methods involving direct wafer bonding). Consequently, the LiNbO_3 tightly adheres to ITO substrates. Delamination, detachment, or abrasion of the LiNbO_3 microstructures from the ITO substrates were not observed during the entire sample lifetime.

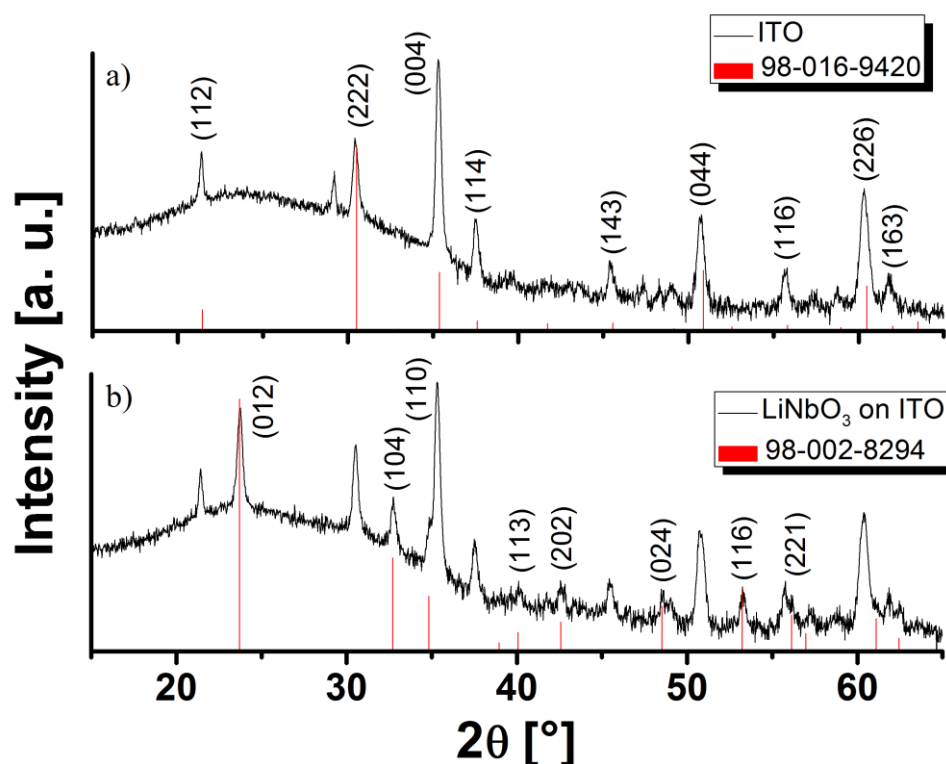


Figure 3.9: XRD characterization of the patterned LiNbO_3 films. a) XRD pattern of the ITO substrate before any modification or use. The red lines (PDF 98-016-9420, Inorganic Crystal Structure Database (ICSD)) indicate characteristic reflections of In_2O_3 with a cubic crystal system.^[187] b) XRD pattern of a holey LiNbO_3 film on an ITO substrate. The red lines (PDF 98-002-8294, ICSD) indicate characteristic reflections of LiNbO_3 with a hexagonal crystal system.^[188]

3.3.4. Phase analysis of the layered LiNbO_3 -ITO system

X-ray diffraction (XRD) analysis revealed that the calcination step transformed the precursor mixture into randomly oriented nanocrystals consisting of trigonal LiNbO_3 (space group $R3c$). The XRD patterns of an ITO substrate before any modification or use show characteristic reflections of cubic ITO belonging to space group $Ia-3$ (Figure 3.9a).^[187] Moreover, an amorphous halo is apparent in the 2θ range from 15° to 35° . After capillary stamping of the aqueous LiNbO_3 precursor solution and calcination, in addition the characteristic reflections of trigonal LiNbO_3 occurred, such as the (012) reflection at a 2θ value of 23.710° , the (104) reflection at a 2θ value of 32.702° , the (110) reflection at a 2θ value of 34.826° and the (116) reflection at a 2θ value of 53.231° (Figure 3.9b).^[188] Grazing incidence XRD (GIXRD) measurements were carried out on a thin-film

reference sample to cross-check whether the synthetic route reported here involves any side reactions. The thin-film reference sample was prepared by spin coating the LiNbO_3 precursor solution used for capillary stamping on an ITO substrate and subsequent calcination following the procedure applied to the ITO substrates micropatterned by capillary stamping. The GIXRD measurement did not reveal any indications that components other than LiNbO_3 and ITO were present.

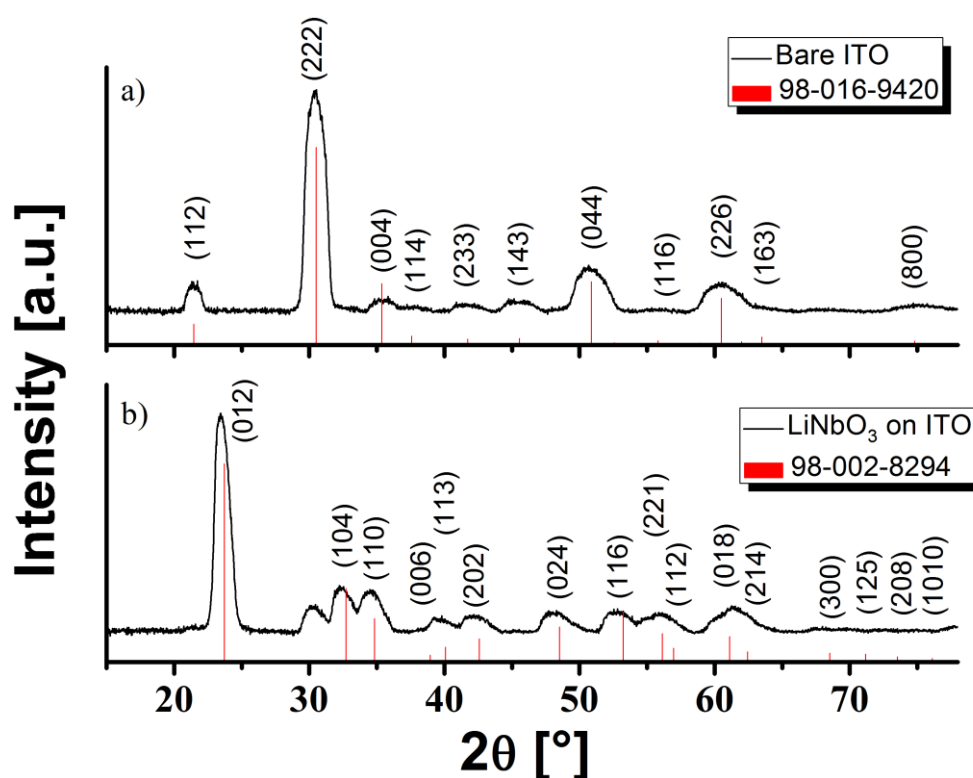


Figure 3.10: Grazing incidence X-ray diffraction (GIXRD) characterization. a) GIXRD patterns of an as-received ITO substrate. The vertical red lines indicate characteristic reflections of In_2O_3 with a cubic crystal system (PDF 98-016-9420; ICSD).^[187] b) GIXRD patterns of a 150 nm thick LiNbO_3 film on an ITO substrate. The vertical red lines indicate characteristic reflections of LiNbO_3 with a hexagonal crystal system (PDF 98-002-8294; ICSD).^[188]

In line with the XRD results obtained here, previous investigations of ITO- LiNbO_3 layer systems also revealed that high-temperature treatments do not significantly compromise the functional properties of LiNbO_3 and ITO. For example, LiNbO_3 was deposited on ITO-coated silicon substrates by radio-frequency sputtering at 600 °C and then annealed

at 750 °C. XRD investigations combined with qualitative SIMS depth profiling revealed that the composition of the different layers was approximately stoichiometric and that only a limited number Li and O vacancies had formed.^[189] It should also be noted that well-established LiNbO₃ layer transfer methods involving direct wafer bonding steps include high-temperature treatments of the transferred LiNbO₃ layers to remove defects and to reduce their surface roughness.^[17,190] In this case, the mismatch of the thermal expansion coefficients of the transferred LiNbO₃ layers and the substrates needs to be considered also. Nevertheless, commercial products can reliably be produced in this way.

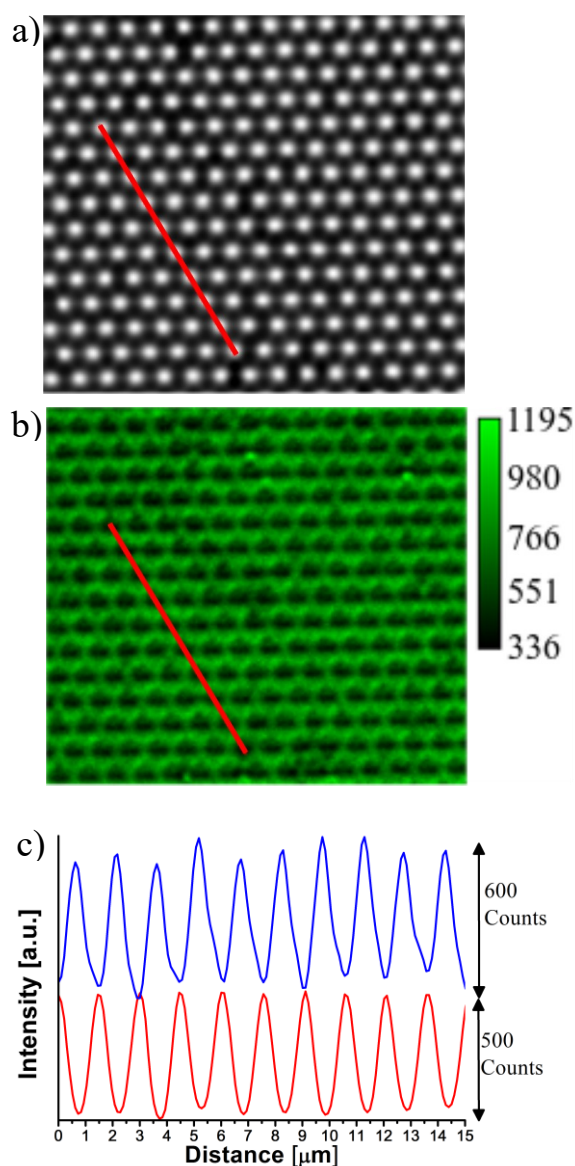


Figure 3.11: Mapping of the SHG output of a holey LiNbO₃ film. a) Transmission CLSM image of a holey LiNbO₃ film on an ITO substrate. The image field extends 20 x 20 μm². Areas covered by LiNbO₃ appear dark, the holes where the ITO substrate is exposed

bright. b) Confocal scanning non-linear optical microscopy of the SHG output at 500 nm of the sample area shown in panel a). Black areas have lower SHG output, green areas higher SHG output. The edge length of a pixel is 104 nm. c) Intensity line profiles taken along the red lines in panel a) and b). The upper blue curve was taken from the SHG intensity map (panel b), the lower red curve from the transmission CLSM image (panel a).

3.3.5. Second harmonic generation of micropatterned LiNbO₃ films

Figure 3.11a shows a transmission confocal laser scanning microscopy (CLSM) image of a holey LiNbO₃ film on an ITO substrate. The LiNbO₃ rims appear dark and the holes, where the surface of the ITO substrate is exposed, appear bright. Microscopic scanning of the SHG^[183] in the same area yielded the SHG map displayed in Figure 3.11b. The SHG signal reproduces the structure of the holey LiNbO₃ film apparent from the CLSM image (Figure 3.11a) and is in line with the LiNbO₃ patterns imaged by SEM (Figure 3.6a,b) and AFM (Figure 3.6c). Figure 3.11c shows intensity profiles along the red lines in the transmission CLSM image seen in Figure 3.11a (lower red curve) and the SHG map shown in Figure 3.11b (upper blue curve). Both intensity profiles were taken along the same path on the sample. The brightness minima in the intensity profile obtained from the transmission CLSM image, which correspond to the LiNbO₃ rims, are correlated with the maxima in the intensity profile obtained from the SHG map. In turn, the brightness maxima in the intensity profile obtained from the transmission CLSM image, which correspond to the holes where the surface of the ITO substrate is exposed, are correlated with the minima in the intensity profile obtained from the SHG map. The peak-to-valley amplitudes apparent in the SHG intensity profile amounted on average to 484 ± 47 counts. The intensity of SHG signals originating from LiNbO₃ depends on the orientation of the LiNbO₃ crystals relative to the laser polarization. The good homogeneity of the SHG signal in the areas covered by LiNbO₃ indicates that the number of randomly oriented nanoscale LiNbO₃ crystallites located in the focal volume was by and large sufficient to cancel out orientation effects. This outcome is consistent with the XRD results and corroborates the notion that the LiNbO₃ nanocrystals are small enough for macroscale isotropy but large enough to show the characteristic NLO properties of LiNbO₃.

According to previous reports, no indications for size-induced symmetry changes were found for LiNbO₃ particles with diameters down to 5 nm, which in turn still show full non-linear optical response.^[191] Layer transfer *via* direct wafer bonding is typically limited to single-crystalline layers having strongly anisotropic properties. For certain applications, it might be advantageous if LiNbO₃ exhibits isotropic properties on the macroscale – for example, if it is desired to harvest photons for SHG and other optical functionalities from randomly scattered light.

3.3.6. Orthogonal functionalization of ITO substrates: micropatterned LiNbO₃-gold films

Orthogonal substrate functionalization involves the deposition of two functional components on a substrate. Ideally, synergistic effects result in functionalities that cannot be achieved by single-component substrate functionalizations. As example, the SHG intensity of the holey LiNbO₃ films were boosted by electrodeposition of gold at a constant voltage of 0 V *versus* Ag/AgCl for 600 s adapting procedures described elsewhere.^[182] The electrodeposition of gold was templated by the microstructured LiNbO₃ film functioning as a lithographic mask in that the gold was exclusively deposited in the holes, where the surfaces of the conductive ITO substrates were exposed. In contrast, no gold was deposited in the areas covered by the insulator LiNbO₃. Therefore, at least the uncovered areas of the ITO substrates apparently retained their surface conductivity. The change in the dielectric permittivity across the ITO/lithium niobate interface (LiNbO₃ is a large-band gap insulator) will have a negligible effect on the ITO conductivity. Only photoelectrical processes may cause changes in the conductivity of the ITO, but are not expected to occur for the nominally pure lithium niobate formed here (besides at residual defects due to impurities). The only photoelectric process that may be envisioned for lithium niobate/ITO systems is band-to-band excitation via two-photon absorption (TPA) triggered by intensive IR radiation. However, in the case of TPA the SHG efficiency would break down significantly.

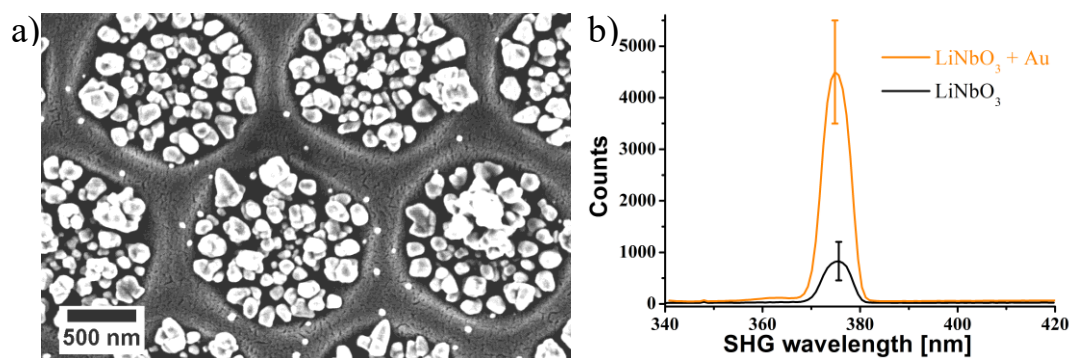


Figure 3.12: Holey LiNbO₃ films on ITO after electrodeposition of gold into the holes. a) SEM image. b) SHG curves of a holey LiNbO₃ film prior to (black curve) and after (orange curve) electrodeposition of gold. The curves are the average of 12 spectra taken at different positions on each sample with an excitation wavelength of 750 nm. The error bars indicate the standard deviations.

The SHG output of holey LiNbO₃ films prior to and after electrodeposition of gold into the holes was comparatively studied by nonlinear spectroscopy (Figure 3.12b). In preliminary experiments the electrodeposition parameters were adjusted in such a way that the gold deposited in the form of nanoparticles with diameters in the 100 nm range showed a broad optical absorption maximum related to the excitation of LSPs at 750 nm (Figure 3.13).

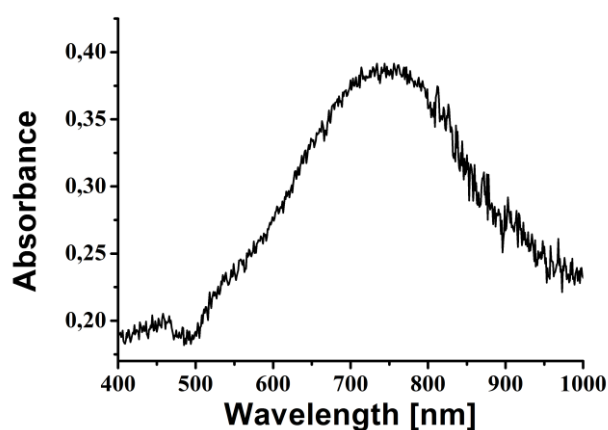


Figure 3.13: Localized surface plasmon resonance of gold deposited by electrodeposition for 300 s at 0 V on an ITO substrate probed by absorption spectroscopy with a two-beam spectrometer UV-3600 Shimadzu (spectral resolution 1 nm). The baseline of the spectrum was measured in a part of the ITO substrate where the ITO was not covered with gold so that the displayed spectrum exclusively represents the absorbance of the deposited gold.

Hence, this wavelength was used to excite both LSPs and to generate SH emission. As a result, the SHG output had a wavelength of 375 nm. For all measurements the setup parameters, such as the distance between lens L1 and the sample surfaces, were kept constant so as not to change the laser intensity on the sample surface. Also, all tested samples had the same layer thickness of ~ 100 nm. The SHG curves shown in Figure 3.12b are the average of spectra taken at 12 different positions on each sample. In the case of the holey LiNbO₃ film prior to electrodeposition of gold, the maximum SHG intensity at 375 nm obtained in this way amounted to 829 ± 224 counts. After electrodeposition of gold into the holes, the maximum SHG intensity increased to 4498 ± 1000 counts. Therefore, electrodeposition of gold into the holes increased the SHG intensity by a factor of 5.4.

3.4. Conclusion

The additive parallel manufacturing of thin micropatterned lithium niobate films with dimensions suitable for waveguide applications has been reported, achieved through capillary stamping of aqueous lithium niobate precursor solutions with porous polymer stamps. The environmentally friendly aqueous inks contained lithium acetate and niobium oxalate hydrate as cheap and commercially available lithium and niobate sources, which can simply be dissolved in water. The use of porous polymer stamps and the stability of the precursor solution allows replenishment of ink through the pore systems of the stamps anytime during stamping. Hence, continuous automatized stamping operations are possible. Moreover, the polymeric stamp material can easily be topographically structured with arbitrary patterns, which can then be lithographically transferred. Classical methods to transfer LiNbO₃ layers involve direct wafer bonding, for which the contacting surfaces must be absolutely smooth. Since even minute amounts of particulate contaminations impede efficient contact formation, clean room conditions are required. These stringent requirements enhance the complexity of classical layer transfer techniques. In addition, the application-specific microstructuring of the

transferred LiNbO₃ layers is typically achieved by complex subtractive lithographic methods. By contrast, capillary stamping of aqueous LiNbO₃ precursor inks can be carried out under ambient conditions and enables the patterning of rough substrates not suitable for direct wafer bonding with LiNbO₃ microstructures. As example, LiNbO₃ precursor solution on hydrophobically modified ITO substrates were stamped. Subsequent calcination yielded micropatterned LiNbO₃ films containing regular arrays of holes, in which ITO was exposed. The LiNbO₃ film showed uniform SHG except at the positions of the holes. As example for orthogonal functionalization, gold nanoparticles were electrodeposited into the holes, resulting in an increase in the SHG output by a factor of 5.4. Thus, the SHG enhancement for LiNbO₃ by a plasmonic material in a thin-layer configuration was demonstrated. The specific configuration could be used as test substrate for multiphoton and/or NLO microscopes (without gold deposition) or as coating to harvest photons for SHG (with gold deposition). Capillary stamping of aqueous LiNbO₃ precursor solutions might be an alternative for the high-throughput manufacturing of thin patterned LiNbO₃ layers, which can, moreover, easily be orthogonally functionalized to enhance existing beneficial properties or to introduce additional beneficial properties.

4. Additive solvothermal capillary stamping with double network hydrogel-derived aerogel stamps

4.1. Introduction

Integration of solvothermal reaction products into complex thin-layer architectures is frequently achieved by combinations of layer transfer and subtractive lithography, whereas direct additive substrate patterning with solvothermal reaction products has remained challenging.^[70] Reactive additive capillary stamping under solvothermal conditions as a parallel contact-lithographic access to patterns of solvothermal reaction products in thin-layer configurations were reported. To this end, corresponding precursor inks are infiltrated into mechanically robust mesoporous aerogel stamps derived from double-network hydrogels (DNHGs). The stamp is then brought into contact with a substrate to be patterned under solvothermal reaction conditions inside an autoclave. The precursor ink forms liquid bridges between the topographic surface pattern of the stamp and the substrate. Evaporation-driven enrichment of the precursors in these liquid bridges along with their liquid-bridge-guided conversion into the solvothermal reaction products yields large-area submicron patterns of the solvothermal reaction products replicating the stamp topography. As example, thin hybrid films, which contained ordered monolayers of superparamagnetic submicron nickel ferrite dots prepared by solvothermal capillary stamping surrounded by nickel electrodeposited in a second, orthogonal substrate functionalization step were prepared. The submicron nickel ferrite dots acted as magnetic hardener halving the remanence of the ferromagnetic nickel layer. In this way, thin-layer electromechanical systems, transformers and positioning systems may be customized.

4.2. Experimental section

4.2.1. Chemicals and materials

Acrylamide (AAM) (>99%) and zirconium(IV)-chloride (>98%) were purchased from Merck. Potassium peroxodisulfate (PPS) (>99%) and titanium(IV)-chloride (>99%) were purchased from Fluka. *N,N*-Methylenebis(acrylamide) (MBA) (99%), *p*-toluenesulfonyl chloride (>98%), nickel(II)-acetylacetonate (95%), iron(III)-acetylacetonate (97%), nickel sulfate, sodium chloride, boric acid and potassium dodecyl sulfonate were

purchased from Sigma-Aldrich. *N,N,N,N*-tetramethylethylenediamine (TMEDA) (99 %) and tetraethoxysilane (98 %) were purchased from Alfa Aesar. Ethylene glycol (99.8 %) was purchased from VWR Chemicals. Perfluorodecyltrichlorosilane (FDTS; $C_{10}H_{17}Cl_3F_{17}Si$) was purchased from aber GmbH (Karlsruhe). Synthetic hectorite $Na^{+}_{0.7}[(Si_8Mg_{5.5}Li_{0.3})O_{20}(OH)_4]^{-0.7}$ (Laponite RD) was purchased from GMW (Vilsheim). Macroporous silicon^[185,192] with macropores having a diameter of 1 μm and a depth of 730 nm arranged in a hexagonal array with a lattice constant of 1.5 μm was purchased from Smart Membranes (Halle an der Saale). Indium tin oxide substrates $(In_2O_3)_{0.9} \cdot (SnO_2)_{0.1}$ (resistance 8-12 Ωsq^{-1} , thickness 1200–1600 \AA) were purchased from Sigma Aldrich. All water used was fully deionized and further purified using a Sartorius stedim/arium 611 UV device. If not stated otherwise, chemicals were used as received.

4.2.2. Fabrication of DNHG-derived aerogel stamps

The experimental procedures for the preparation of the DNHGs and the DHNG-derived aerogels described in chapter "4.2.2. Fabrication of DNHG-derived aerogel stamps" were developed by Martin Frosinn and are part of his PhD work. However, to provide a complete description of the experimental procedures, the protocols for the DNHG synthesis provided by Martin Frosinn as private communication are already included in this work.

Preparation of synthetic hectorite/zirconylchloride octahydrate solutions

To prepare synthetic hectorite solutions, 10 g synthetic hectorite was dissolved in 1 L deionized water. Synthetic hectorite solutions show a complex phase evolution starting with the swelling of stacked hectorite platelets, which is followed by exfoliation and the formation of house-of-cards structures, in which the positive charged sides of the platelets interact with the negative charged faces of surrounding platelets (Figure 4.1).^[193]

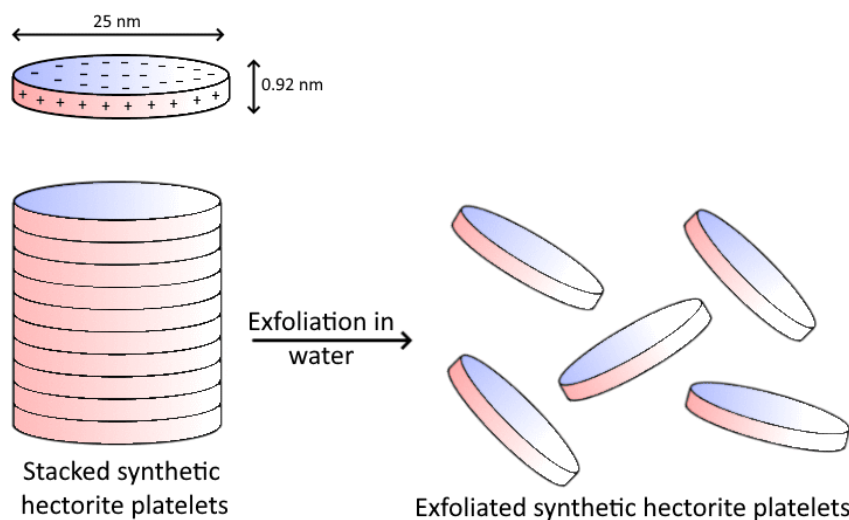


Figure 4.1: Exfoliation of synthetic hectorite platelets. In the dry state, synthetic hectorite platelets are stacked. Upon contact with water, swelling and exfoliation occurs. Since only exposed platelet surfaces can adsorb TMEDA radicals, complete exfoliation is desirable. Addition of acidic zirconyl chloride leads to partial precipitation. The precipitate re-disperses within one or two days. To ensure a high degree of homogeneity, the sol is left to equilibrate for one week. Figure provided by M. Frosinn.^[10]

Therefore, the properties of freshly prepared synthetic hectorite solutions slightly differ from those of aged synthetic hectorite solutions. Thus, all synthetic hectorite solutions used in this work were aged for at least one week. Zirconylchloride octahydrate was prepared by hydrolyzing zirconium chloride in deionized water, followed by evaporation of excess water under reduced pressure until no further mass loss was observed. 100 g of zirconylchloride octahydrate was added to the turbid synthetic hectorite solutions, which were then stirred for one week so that transparent synthetic hectorite/zirconylchloride octahydrate solutions were obtained.

Preparation of tetrakis-(2-hydroxyethoxy)-silane solutions in ethylene glycol

Ethylene glycol (300 g, 4.83 mol), tetraethoxyorthosilane (250 g, 1.20 mol) and *p*-toluenesulfonyl chloride (40 mg, 0.21 mmol) were filled into a 1 L round-bottom flask. Vigorous stirring for 60 minutes at 70 °C under ambient pressure yielded a homogenous colorless solution. 200 g of the reaction product ethanol was removed from the sol solution by distillation with a rotary evaporator applying a reduced pressure of 300 mbar

for two hours and subsequently a reduced pressure of 90 mbar. Thus, a clear, colorless and moisture-sensitive solution containing tetrakis-(2-hydroxyethoxy)-silane as well as oligomeric or polymeric silane species derived from tetrakis-(2-hydroxyethoxy)-silane in ethylene glycol was obtained.

Preparation of the sol solution for the DNHG synthesis

8 g tetrakis-(2-hydroxyethoxy)-silane solution was added to 10 g synthetic hectorite/zirconylchloride octahydrate solution in a 50 ml round-bottom flask under constant stirring. Subsequently, 6 g AAm (84.41 mmol) and 2.5 mg MBA (0.0162 mmol) were added. The flask was placed in an ice bath after a clear solution was obtained. A mixture of 2 μ l TMEDA (1.55 mg, 0.0133 mmol) in 0.5 ml H₂O was added and the flask was closed with a septum cap. A separate flask with a septum containing 4 mg PPS (0.0148 mmol) and 1 ml H₂O was placed in the ice bath as well. Both solutions were suffused with nitrogen for 30 minutes. Under exclusion of oxygen, both solutions were combined and mixed thoroughly. The combined solutions were subjected to three vacuum-ultrasonication cycles under cooling to 0 °C using ice baths. Each cycle comprised the application of a vacuum for 30 seconds using a diaphragm pump followed by sonication for 30 seconds, while the vacuum was maintained. The obtained sol solution was kept at 0 °C under nitrogen atmosphere and used within 5 minutes.

Preparation of DNHG-derived aerogel stamps

The surface of macroporous silicon was treated with oxygen plasma for 10 minutes and then coated with FDTS by chemical vapor deposition at 100 °C for 10 h following procedures reported elsewhere.^[181] About 15 mL of the sol solution was poured onto FDTS-coated macroporous silicon pieces extending 1 cm² located in glass vials under exclusion of oxygen under nitrogen atmosphere. The vials were closed airtight and gelation as well as aging was allowed to take place at 25 °C for at least one week. The aged cylindrical DNHG monoliths with a diameter of 24 mm, a height of ~22 mm and a mass of ~16 g having a topographically patterned contact surface were detached from the

macroporous silicon under ambient conditions while still being wet. Then, each aged hydrogel monolith was treated with 500 ml methanol for 120 h, 500 ml THF for 120 h and 500 ml *n*-hexane for 120 h in a Soxhlet extractor. This procedure resulted in shrinkage to 78% of the initial volume of the water-filled DNHG. Evaporation of the *n*-hexane at 20 °C in a vacuum of ~ 0.001 mPa did not lead to further shrinkage. Subsequently, the macroporous silicon template was removed from the gel. As a result, DNHG-derived aerogel stamps (**3**) (Figure 4.2) were obtained, which had contact surfaces extending 1 cm² topographically patterned with contact elements (**4**). The contact elements (**4**) had a diameter of 900 nm and a height of 600 nm. Prior to further use, the height of the DNHG-derived aerogel stamps (**3**) was reduced to ~ 1.3 cm by sawing. The remaining surfaces except the topographically patterned contact surface with the contact elements (**4**) were ground to shape DHNG-derived aerogel stamps as desired.

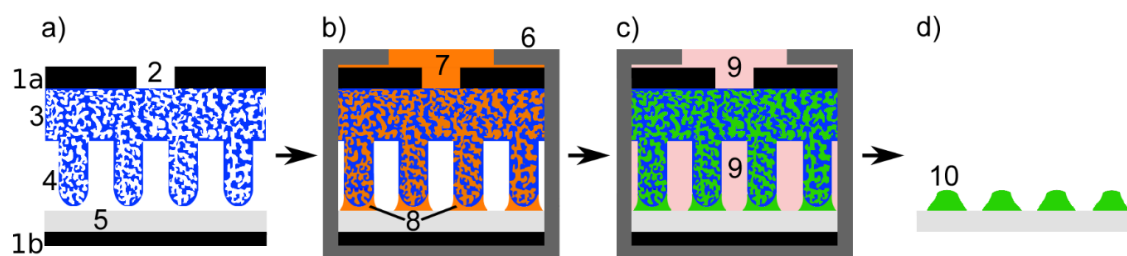


Figure 4.2: Additive solvothermal capillary stamping. a) A stamping device (**1**) consists of an upper part (**1a**) with an ink supply hole (**2**) and a lower part (**1b**). A DNHG-derived aerogel stamp (**3**) with contact elements (**4**) is attached to upper part (**1a**) and approached to a substrate (**5**) attached to lower part (**1b**). b) Stamping device (**1**) is inserted into PTFE vessel (**6**). Precursor solution (**7**) deposited on the surface of upper part (**1a**) flows through hole (**2**) into DNHG-derived aerogel stamp (**3**) and forms liquid bridges (**8**) between contact elements (**4**) and substrate (**5**). c) PTFE vessel (**6**) is then located in a sealed steel autoclave (**11**). Under solvothermal conditions, an ethanol-rich gas phase (**9**) fills PTFE vessel (**6**). The nonvolatile precursors of the solvothermal reaction product (**10**) and eventually solvothermal reaction product (**10**) itself enrich in the liquid bridges (**8**). d) After removal from stamping device (**1**) and detachment of DNHG-derived aerogel stamp (**3**), substrate (**5**) is modified by patterns of solvothermal reaction product (**10**), here arrays of submicron nickel ferrite dots.

4.2.3. Additive solvothermal capillary stamping

The following figure illustrates the schematic for capillary stamping under solvothermal conditions via DNHG-derived aerogel stamp.

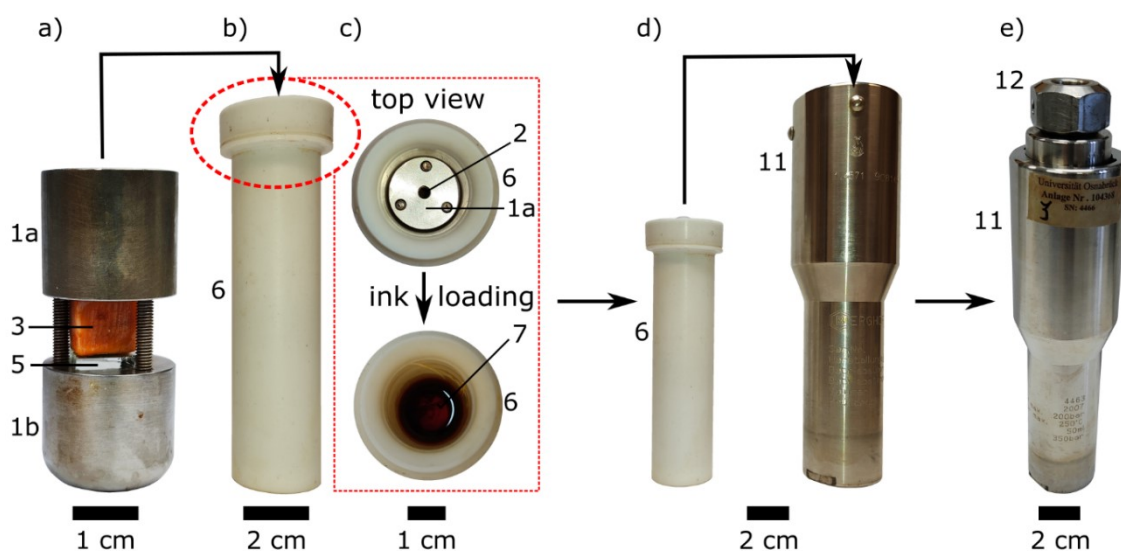


Figure 4.3: Setup for additive solvothermal capillary stamping. a) Stamping device (1) consists of an upper part (1a), on which a DNHG-derived aerogel stamp (3) is mounted, and a lower part (1b), on which substrate (5) (here: FDTs-coated ITO) is placed. Upper part (1a) and lower part (1b) are then connected by pins preventing lateral displacement. b) Stamping device (1) including the DNHG-derived aerogel stamp (3) and substrate (5) is transferred into PTFE vessel (6). c) Upper part (1a) of stamping device (1) containing hole (2) is covered with precursor solution (7) while located in PTFE vessel (6). Precursor solution (7) flows through hole (2) into the DNHG-derived aerogel stamp (3). d) PTFE vessel (6) including stamping device (1), DNHG-derived aerogel stamp (3), substrate (5) and precursor solution (7) is inserted into steel autoclave (11). e) Steel autoclave (11) is then sealed with lid (12).

The stamping device (1) consisted of an upper part (1a) and a lower part (1b). The upper part (1a) consisted of a stainless-steel cylinder with a diameter and a height of 2 cm. The steel cylinder contained three peripheral holes parallel to the cylinder axis with a diameter of 3 mm forming an equilateral triangle with an edge length of 1.4 cm as well as a central hole (2) parallel to the cylinder axis with a diameter of 4 mm. A DNHG-derived aerogel stamp (3) was glued onto the upper part (1a) with double-sided adhesive tape in such a way that the contact elements (4) of the DNHG-derived aerogel stamp (3) pointing away from upper part (1a) where exposed (Figure 4.2). The lower part (1b) of the stamping

device (**1**) was an exact copy of the upper part (**1a**) except that it did not contain a central hole (**2**). The ITO substrates (**5**) were coated with FDTS applying the same procedure reported elsewhere^[181] as in the case of macroporous silicon. The contact elements (**4**) of the DNHG-derived aerogel stamp (**3**) glued on the upper part (**1a**) were brought into contact with an FDTS-coated ITO substrate (**5**) placed on the lower part (**1b**) (Figure 4.2a). The upper part (**1a**) was then fixed on the lower part (**1b**) by inserting pins into the three peripheral holes of upper part (**1a**) and the corresponding counterpart holes in the lower part (**1b**) (Figure 4.3a). The pins prevented lateral displacement of the upper part (**1a**) and the lower part (**1b**) with respect to each other. Furthermore, the pins prevented lateral displacement of the FDTS-coated ITO substrate (**5**), which was not fixated otherwise on the lower part (**1b**). The contact pressure exerted by the DNHG-derived aerogel stamp (**3**) on the FDTS-coated ITO substrate (**5**) amounted to 3.9 kN/m² and originated from the mass of the upper part (**1a**) of 40 g. The assembled stamping device (**1**) including the DNHG-derived aerogel stamp (**3**) and the FDTS-coated ITO substrate (**5**) was then inserted into a cylindrical PTFE vessel (**6**) with a height of 12 cm, a diameter of 3.8 cm and a total volume of 40 mL (Figure 4.3b). The upper part (**1a**) of stamping device (**1**) fitted into PTFE vessel (**6**) in such a way that the rim of the upper part (**1a**) was in close, self-sealing contact with the wall of the PTFE vessel (**6**). Nickel ferrite precursor solution (**7**) was prepared by dissolving 54.8 mg (0.2 mmol) nickel(II)-acetylacetonate and 150.68 mg (0.4 mmol) iron(III)-acetylacetonate in 50 mL ethanol. 6 mL of precursor solution (**7**) was deposited on the surface of the upper part (**1a**) of the stamping device (**1**) located in PTFE vessel (**6**), flowed through the central hole (**2**) in the upper part (**1a**) and infiltrated the DNHG-derived aerogel stamp (**3**) (Figure 4.2b and Figure 4.3c). Then, the PTFE vessel (**6**) containing the assembled stamping device (**1**) loaded with precursor solution (**7**) was inserted into a steel autoclave (**11**), which was then sealed with a steel lid (**12**) (Figure 4.2c and Figure 4.3d). The solvothermal reaction yielding arrays of submicron nickel ferrite dots (**10**) was carried out in a pressure digestion system (Berghof digestec DAB-2) at 413 K (140 °C) for 48 hours. After completion of the synthesis and disassembly of the stamping device (**1**), the DNHG-

derived aerogel stamp (3) was detached from the substrate (5) patterned with submicron nickel ferrite dots (10) (Figure 4.2d), which was washed with ethanol and dried at 40 °C for 1 h. The volume of the autoclave (11) equipped with PTFE vessel (6) and stamping device (1) including a DNHG-derived aerogel stamp (3) and an ITO substrate (5) available to a fluid phase in its interior was determined by differential weighing before and after filling with water and amounted to ~29.15 mL.

4.2.4. Electrodeposition of Nickel

For the electrodeposition of nickel, ITO substrates (5), which were either FDTS-coated or functionalized with submicron nickel ferrite dots (10), were placed in an electrochemical cell. An aqueous plating solution containing 1 mol/L $\text{NiSO}_4 \cdot 6\text{H}_2\text{O}$ and 0.1 mol/L of the other components H_3BO_3 , NaCl and $\text{NaC}_{12}\text{H}_{25}\text{SO}_4$ was used.^[194] Thus, 0.536 g $\text{NiSO}_4 \cdot 6\text{H}_2\text{O}$ (0.02 mol), 0.124 g H_3BO_3 (0.002 mol), 0.117 g NaCl (0.002 mol) and 0.557 g $\text{NaC}_{12}\text{H}_{25}\text{SO}_4$ (0.002 mol) dissolved in 20 ml water were deposited into the electrochemical cell. The ITO substrate (5) acted as working electrode, a platinum wire as counter electrode and an Ag/AgCl electrode as reference electrode. The electrodeposition was carried out at a constant current of 1 mA/cm^2 for 10 min using a potentiostat Interface 1000 (Gamry). The thickness of the nickel films was determined by scanning electron microscopy investigation of a cross-sectional specimen (Figure 4.4).

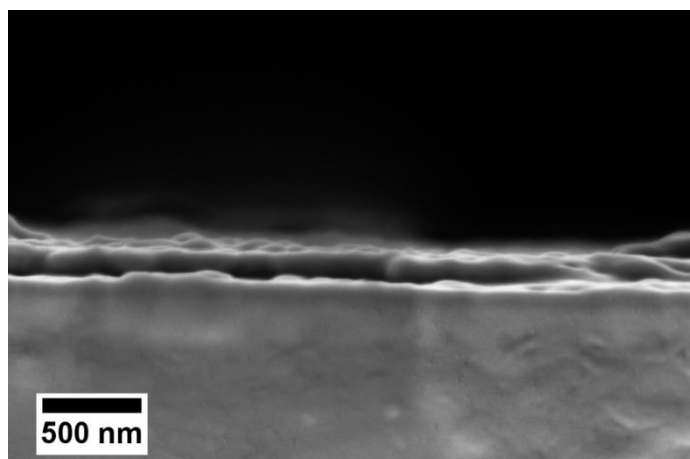


Figure 4.4: Nickel film with a thickness of 100 nm electrodeposited at a constant current of 1 mA/cm^2 for 10 min on an ITO substrate (5) modified with FDTS but without nickel

ferrite dots (10).

4.2.5. Characterization of the DNHG-derived aerogel

4.2.5.1. Nitrogen sorption

Nitrogen sorption measurements on DNHG-derived aerogel samples were performed with a device Autosorb from Quantachrome at 77 K. Before any measurement, about 100 mg sample material was degassed at 373 K for 10 h in an ultrahigh vacuum. The specific surface area was calculated using the BET method in a relative pressure range $p/p_0 = 0.05 - 0.30$. The total pore volume was calculated at $p/p_0 = 0.995$. For the calculation of the pore size distribution, the BJH method was applied to the desorption branch of the isotherm. For the analyses, the program ASiQwin (Quantachrome Instruments) was used. Mercury intrusion measurements applied to determine the porosity of the samples were carried out with a Pascal 440 device (Porotec). Intrusion measurements were performed at 297 K up to 400 MPa. The contact angle of mercury was set to 140° and the surface tension to 0.48 N m^{-1} .

4.2.5.2. Contact angle measurements

Contact angles of the nickel ferrite precursor solution (0.2 mmol nickel(II)-acetylacetonate and 0.4 mmol iron(III)-acetylacetonate dissolved in 50 mL ethanol) on FDTS-modified ITO substrates were measured by the sessile drop method with a DSA100 drop shape analyzer at 22°C and a relative humidity of 33 %. Overall 6 measurements at different positions were carried out.

4.2.5.3. Microscopy and energy-dispersive X-ray spectroscopy

Prior to scanning electron microscopy (SEM) imaging, the samples were dried overnight at 40°C in air and then sputter-coated 2-3 times for 15 s with platinum/iridium alloy using an EMITECH K575X sputter coater. SEM images were taken with a Zeiss Auriga device equipped with a field emission cathode and a Gemini column with a working distance of

5 mm applying an acceleration voltage of 3 kV. For image detection an InLens detector was used. For energy-dispersive X-ray (EDX) spectroscopy mappings a X-Max 80 mm² silicon drift detector (Oxford Instruments) was used. The EDX maps extending 1024x788 pixels were recorded with a pixel dwell time of 5000 μ s and a frame live time of 1.05 h. Atomic force microscopy (AFM) topography images were recorded with an NTEGRA microscope (NT-MDT) in the tapping mode using HQ:NSC16/AL BS cantilevers from μ masch with a resonance frequency of 170 - 210 kHz and a force constant of 30 - 70 N/m.

4.2.5.4. XPS

XPS measurements were carried out under ultra-high vacuum using an ESCA system Phi 5000 VersaProbe III with a base pressure of $1 \cdot 10^{-9}$ mbar equipped with a monochromatized aluminum anode ($K\alpha = 1486.6$ eV) and a 32-channel electrostatic hemispherical electronic analyzer. An ion gun and an electron gun were used to prevent sample charging. A take-off angle of 45° was used. The XP spectra were calibrated using the carbon C 1s peak at 284.5 eV.^[195]

4.2.5.5. X-ray diffraction (XRD) of submicron nickel ferrite dots

XRD scans were carried out in theta-theta geometry with Cu $K\alpha$ radiation using an X'Pert Pro MPD diffractometer (PANalytical) equipped with a rotating sample plate and a PixCel 1D detector. The diffractometer was operated at a voltage of 40 kV and a current of 30 mA. For the XRD measurements, ~ 2 mg submicron nickel ferrite dots (**10**) were carefully scraped off from several ITO substrates (**5**) with scalpels.

4.2.5.6. Magnetometry

Magnetization curves of ITO substrates (**5**) with an area of 1 cm² functionalized with arrays of submicron nickel ferrite dots (**10**), continuous nickel layers with a thickness of ~ 100 nm or nickel ferrite-nickel hybrid films (**13**) (Figure 4.4) were measured at 300 K by varying the magnetic field from -1 T to 1 T using a vibrating sample magnetometer

(LakeShore, Model 7404). Magnetization loops were corrected by subtracting the diamagnetic contribution from the substrate.

4.3. Results and discussion

4.3.1. DNHG-derived aerogel stamps

DNHGs are synthesized by simultaneously polymerizing acrylamide via free radical mechanism and hydrolysis and polycondensation of suitable tetraalkoxysilanes. The resulting double network hydrogel is subjected to a sequence of solvent exchanges, promoting precipitation of the polyacrylamide network. The exact details of the synthesis and the characterization of DNHGs can be found in Alarslan, Frosinn et al.^[10]

The DNHGs were converted to DNHG-derived aerogels by a two-step solvent exchange procedure from water to methanol to *n*-hexane followed by subcritical drying under ambient conditions. The first solvent exchange from water to methanol also results in the removal of residual reactants such as ethylene glycol and of unreacted acrylamide. The polyacrylamide network tends to minimize its surface area exposed to the non-solvent methanol^[196] so that the polyacrylamide precipitates onto the silica network. It is reasonable to assume that the polyacrylamide preferentially agglomerates in the joints between neighboring silica particles. Hence, a tough shell of polyacrylamide encapsulates the brittle silica network. While the tough polyacrylamide network reinforces the stiff silica network, the stiff silica network fixates the tough polyacrylamide network. The second solvent exchange involves the replacement of methanol by *n*-hexane. The lower surface tension of *n*-hexane further reduces the Laplace pressure across the menisci that form in the mesopores during subcritical evaporation of the *n*-hexane under ambient conditions. The DNHG resists the stress occurring during evaporation and undergoes only minor shrinkage, while the structural features of the DNHG are conserved. The DNHG-derived aerogel obtained in this way is a variation of class I hybrid composite aerogels,^[197] since the reinforcing polyacrylamide network and the silica network are physically entangled. Even though the silica network and the polyacrylamide network are not

covalently connected with each other, they cannot be separated without cleavage of covalent bounds. The DNHG-derived aerogel has a mean pore diameter of 18 nm as well as a total pore volume of $34 \text{ cm}^3/\text{g}$ (Figure 4.5a,b) and combines a low density of $0.5 \text{ g} \cdot \text{cm}^{-3}$ with an excellent compressive strength of $53.57 \text{ MPa} \pm 7.71 \text{ MPa}$ (average of five measurements on different specimens, Figure 4.5c).

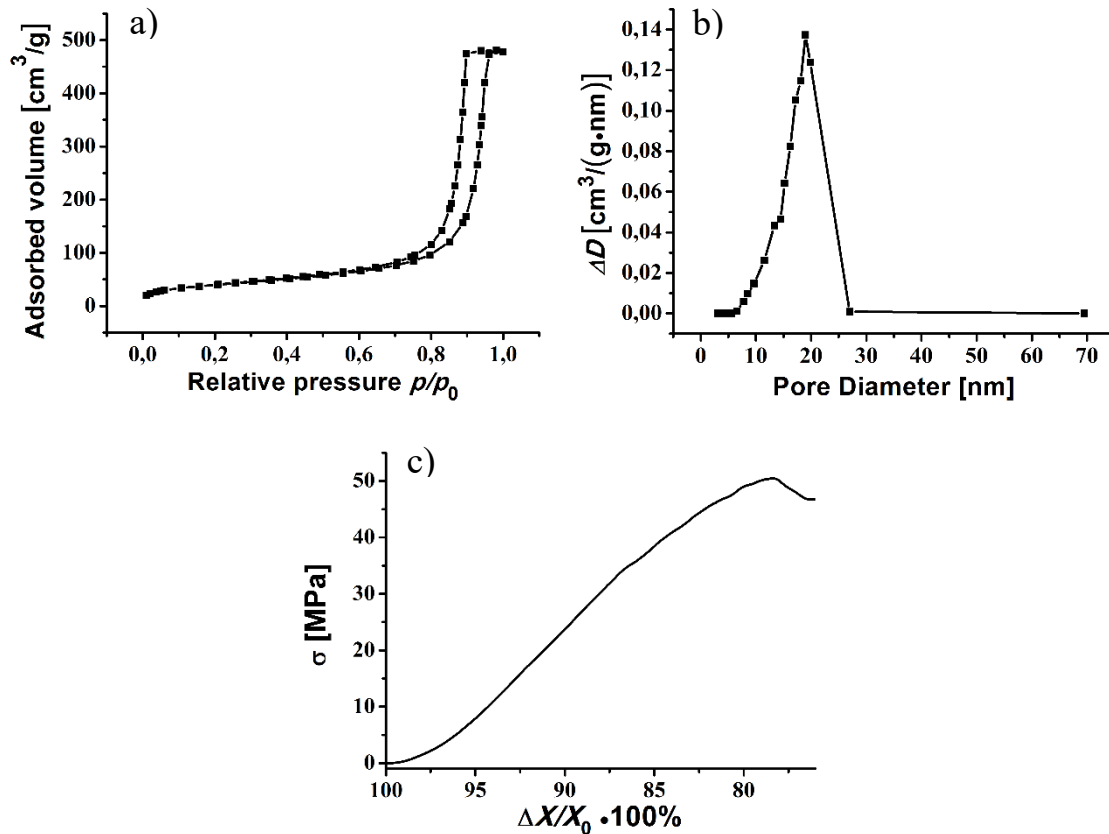


Figure 4.5: Nitrogen sorption measurements on DNHG-derived aerogel. a) Nitrogen sorption isotherm. b) Differential pore volume (ΔD) plotted against the pore diameter. The pore size distribution is calculated with the BJH theory from the desorption branch of the isotherm yielding a mean pore diameter of 18 nm. c) Exemplary stress-strain curve of a DNHG-derived aerogel specimen. The compressive stress σ is plotted against the relative compression $\Delta X/X_0$. X_0 is the initial extension of the DNHG-derived aerogel specimen at the start of the measurement and corresponds to a relative extension of 100 %. At a relative extension of 0 % the absolute thickness of the specimens would approach zero.

DNHG-derived aerogel stamps with topographically patterned contact surfaces can easily be obtained by carrying out the DNHG synthesis in contact with any kind of mold. The mechanical robustness of the DNHG-derived aerogels should allow the realization of

even filigree arbitrary surface structures. For the stamping of ink, the contact surfaces of the topographic stamp features contacting the receiving substrate should exhibit sufficient surface porosity for ink transfer. Considering the spongy pore morphology of the DNHG-derived aerogel stamps used here and their mean pore diameter of 18 nm, the minimum printable feature size was estimated to ~ 100 nm. Here macroporous silicon^[185,192] containing macropores with a diameter of 1 μm and a depth of 730 nm arranged in hexagonal arrays with a pore-center-to-pore-center distance of 1.5 μm were used as mold. The macroporous silicon was selected because it is commercially available and because its feature sizes match those of 2D photonic crystals with bandgaps in the infrared range.^[186] The DNHG-derived aerogel stamps obtained in this way consisted of a monolithic body, which had a height of 13 mm and a topographically patterned contact surface extending 1 cm^2 . The topographic patterns of the contact surfaces consisted of arrays of rod-like contact elements with a height of ~ 600 nm and a diameter of 900 nm arranged in a hexagonal lattice with a lattice constant of 1.5 μm (Figure 4.6a).

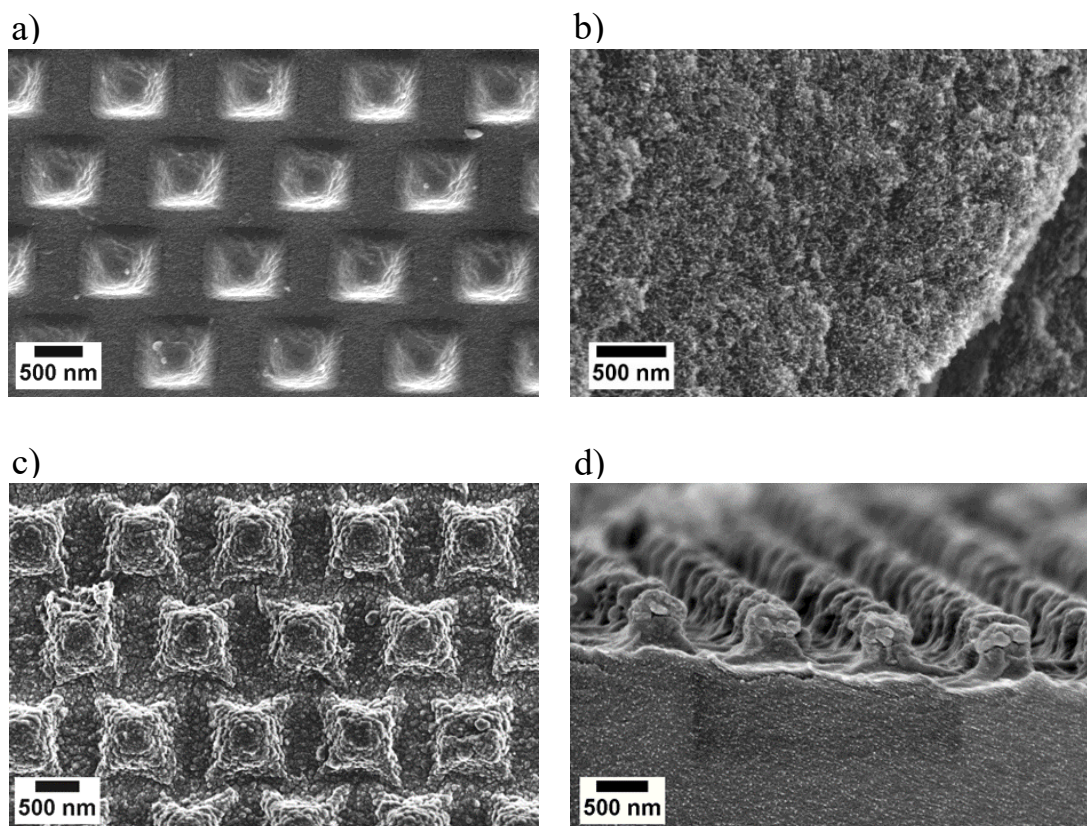


Figure 4.6: SEM images of the contact surfaces of DNHG-derived aerogel stamps (3) with contact elements (4). a) As-prepared DNHG-derived aerogel stamp and b) SEM

image of a cross-section of DHNG-derived aerogel stamp (3). c), d) DNHG-derived aerogel stamp after infiltration with precursor solution (7), solvothermal capillary stamping, disassembly of stamping device (1) and detachment from ITO substrate (5). c) Top view and b,d) cross-section.

The shrinkage in the course of the transition from a DNHG in contact with a macroporous silicon mold to a DNHG-derived aerogel stamp does not affect the lattice constant of the arrays of the contact elements because their positions are fixed by the positions of the macropores of the macroporous silicon molds.

4.3.2. Arrays of submicron nickel ferrite dots by solvothermal capillary stamping

Solvothermal capillary stamping was carried out using a specifically constructed stamping device that consisted of two steel cylinders; an upper part and a lower part. The DNHG-derived aerogel stamps were glued on the upper part. Indium tin oxide (ITO) substrates surface-modified with the silane perfluorodecyltrichlorosilane (FDTS) were placed on the lower part. The upper part and the lower part of the stamping device were assembled in such a way that the contact elements of the DNHG-derived aerogel stamps contacted the FDTS-coated ITO substrates with a contact pressure of 3.9 kN/m^2 (Figure 4.2a and Figure 4.3a). The assembled stamping device was inserted into a cylindrical PTFE vessel (Figure 4.3b). An ethanolic precursor solution containing nickel(II)-acetylacetonate and iron(III)-acetylacetonate was deposited through the opening of the PTFE vessel and the central hole in the surface of the upper part of the stamping device onto the DNHG-derived aerogel stamp (Figure 4.2b and Figure 4.3c). The precursor solution invaded the DNHG-derived aerogel stamp and filled its mesopore network up to the tips of contact elements. The filling level of the DNHG-derived aerogel stamps could be assessed with the naked eye owing to the brown color of the precursor solution. Figure 4.7a shows a photograph of a cross-section of a colorless as-prepared DNHG-derived aerogel stamp, whereas Figure 4.7b shows a photograph of a cross-section of a DNHG-derived aerogel stamp after infiltration with precursor solution. It is obvious that the

precursor solution infiltrated the entire volume of $\sim 1.3 \text{ cm}^3$ of the DNHG-derived aerogel stamp.

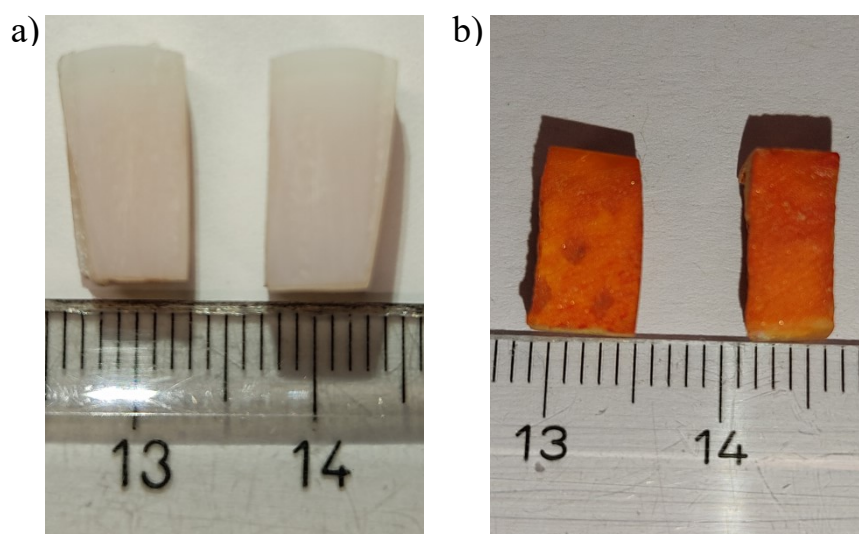


Figure 4.7: Photographs showing cross-sectional views of DNHG-derived aerogel stamps. The topographically structured surfaces with contact elements point outwards. a) As-prepared DNHG-derived aerogel stamps and b) DNHG-derived aerogel stamps infiltrated with precursor solution.

The contact angle of the ethanolic precursor solution on the FDTS-coated rough and grainy ITO substrates under ambient conditions amounted to $52.4^\circ \pm 1.5^\circ$. Therefore, the precursor solution did not spread on the FDTS-coated ITO substrates. Instead, liquid bridges of the precursor solution connecting the tips of the contact elements of the DNHG-derived aerogel stamps and the surface of the FDTS-coated ITO substrates formed (Figure 4.2b). The PTFE vessel containing the stamping device including the DNHG-derived aerogel stamp, the FDTS-coated ITO substrate and the precursor solution was inserted into a steel autoclave (Figure 4.3d,e) with a free volume of $\sim 29.15 \text{ mL}$ available to the fluid phases. The solvothermal conversion yielding nickel ferrite was carried out at 413 K for 48 h . The solvothermal reaction conditions were approximated by considering the phase behavior of pure ethanol, which were estimated by the van der Waals equation of state using van der Waals parameters $a = 12.18 \text{ L}^2 \text{ bar/mol}^2$ and $b = 0.08407 \text{ L/mol}$.^[198] Assuming that 6 mL ($\sim 0.1 \text{ mol}$) liquid ethanol is applied to the stamping device with a free volume of 29.15 mL , at 293.15 K the ethanol forms coexisting liquid and gaseous phases at a pressure of 4.3 bar . The mole fraction of the liquid phase

amounts to 98 % and that of the gas phase to 2 %. At the reaction temperature of 413 K, liquid and vapor phases coexist at a pressure of 24.6 bar. The mole fractions of the liquid and vapor phases amount to 84 % and 16 %. Thus, under the solvothermal reaction conditions applied here precursor solution and an ethanol-rich vapor phase coexist. However, prior to the supply of precursor solution, no ethanol at all is present in the volume between upper part and lower part of the stamping device. Hence, the ethanol-rich vapor phase is solely obtained by evaporation of ethanol, which can, in principle, occur at the mesopore openings of the DNHG-derived aerogel stamp or at the liquid bridges between the contact elements of the DNHG-derived aerogel stamp and the ITO substrate. However, the concave menisci and the negative Laplace pressure of the precursor solution at the mesopore openings impedes transfer of solvent molecules from the liquid phase to the vapor phase. The liquid bridges do not only have a large exposed liquid surface. Their concave curvature normal to ITO substrate is smaller than the concave curvatures of the menisci at the mesopore openings and impedes evaporation to lesser extent. On the other hand, the curvature of the liquid bridges parallel to the ITO substrate is convex. This convex curvature component will also enhance evaporation, considering that the vapor pressure resulting from liquid surfaces with convex curvature is enhanced as compared to that resulting from plane surfaces, as quantified by the Kelvin equation.^[199] Therefore, it is reasonable to assume that the ethanol preferentially evaporates from the liquid bridges into the volume between the upper part and the lower part of the stamping device.

The applied volume of the precursor solution exceeds the volume of the DNHG-derived aerogel stamp by a factor of more than 5 so that the DNHG-derived aerogel stamp is always in contact with a bulk reservoir of the precursor solution located above the upper part of the stamping device. Evaporation drags new precursor solution from the interior of the DNHG-derived aerogel stamp into the liquid bridges. The interior of the DNHG-derived aerogel stamp is in turn refilled from the above-mentioned bulk reservoir of the precursor solution. The nonvolatile nickel ferrite precursors thus enrich in the liquid bridges and are then converted to the solvothermal reaction product nickel ferrite (Figure

4.2c). It is assumed that the precursor enrichment mechanism is the main reason for the formation of three-dimensional submicron nickel ferrite dots in place of the liquid bridges. After completion of the solvothermal capillary stamping procedure, removal of the stamping device from the autoclave and the PTFE vessel, disassembly of the stamping device and detachment from the ITO substrate, the DNHG-derived aerogel stamps did not show any damage. While the DNHG-derived aerogel stamps are apparently partially filled with the reaction product nickel ferrite, the contact elements at their contact surface remained intact (Figure 4.6c,d). The DNHG-derived aerogel stamps could be reused after ultrasonication in ethanol for 30 minutes.

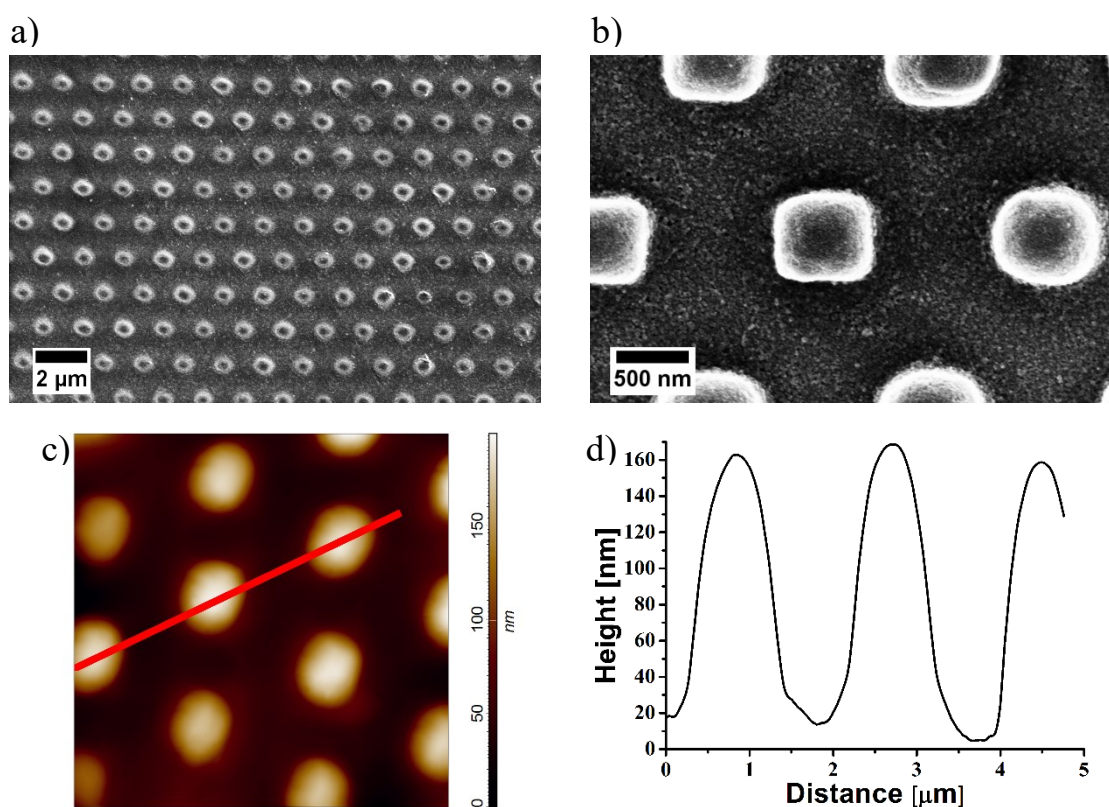


Figure 4.8: Arrays of submicron NiFe_2O_4 dots on ITO substrates. a) Large-field SEM top-view image. b) SEM top view image at higher magnification. c) AFM topography image (the image field extends $5 \times 5 \mu\text{m}^2$) and d) topographic height profile along the red line in panel c).

4.3.3. Properties of submicron nickel ferrite dot arrays

Solvothermal capillary stamping yielded ITO substrates patterned with ordered monolayers of submicron nickel ferrite dots (Figure 4.2d) typically extending 1 cm^2 –

corresponding to the area of the contact surface of the DNHG-derived aerogel stamps. The nearest-neighbor distance between the submicron nickel ferrite dots amounted to 1.5 μm and corresponds to the nearest-neighbor distance between the contact elements of the DNHG-derived aerogel stamps. The submicron nickel ferrite dots had a diameter of ~ 700 nm (Figure 4.8a,b) and a height of ~ 150 nm (Figure 4.8c,d). X-ray photoelectron spectroscopy (XPS) was deployed to evaluate whether the FDTS coating on the ITO substrates was still intact after the solvothermal synthesis (Figure 4.9).

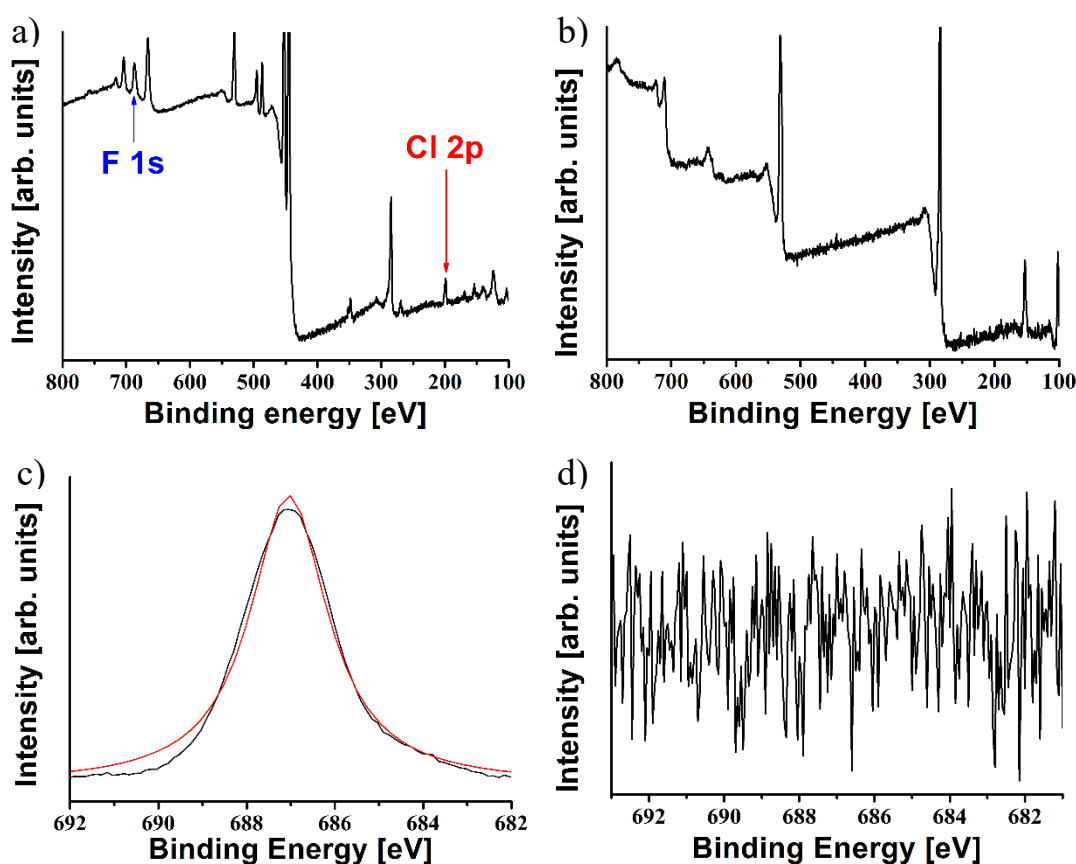


Figure 4.9: XPS spectra of ITO substrates. a) XPS spectrum of an ITO substrate modified with FDTS before solvothermal treatment. b) XPS spectrum of an ITO substrate modified with FDTS after solvothermal treatment. c), d) High-resolution XPS spectra of ITO substrates modified with FDTS c) before and d) after solvothermal treatment covering the binding energy range in which the F 1s peak at 687.04 eV appears. The black curves are raw data; the red curve in panel c) is a Lorentzian fit. The XPS spectra were measured with a take-off angle of 45° .

An XPS spectrum of an FDTS-coated ITO substrate shows the fluorine 1s peak at 686.43 eV indicating the presence of FDTS. However, after the solvothermal synthesis fluorine

was no longer found. Moreover, after the solvothermal synthesis the precursor solution spread on the ITO substrates. These observations corroborate the notion that the solvothermal treatment resulted in the destruction of the FDTs coating.

X-ray powder diffractometry confirmed that any material that could be scraped off from the ITO substrates consisted of nickel ferrite. The diffractogram obtained in this way (Figure 4.10a) exhibited the characteristic reflections of cubic NiFe_2O_4 showing inverse spinel structure (space group $Fd-3m$), such as the (220) reflection at $2\theta = 30.295^\circ$, the (311) reflection at $2\theta = 35.686^\circ$, the (511) reflection at $2\theta = 57.377^\circ$ and the (440) reflection at $2\theta = 63.015^\circ$. The magnetic moment of an array of submicron nickel ferrite dots on an ITO substrate as function of the external magnetic field were measured by vibrating sample magnetometry (VSM) at 300 K. While bulk nickel ferrite shows ferrimagnetic behavior, the submicron nickel ferrite dots are superparamagnetic with vanishing magnetization hysteresis and vanishing remnant magnetization. The magnetic moment per sample area approached its saturation value of $1.1 \cdot 10^{-3} \text{ emu/cm}^2$ at an external magnetic field of $\pm 10000 \text{ G}$ (Figure 4.10b). Rescaling the magnetic moment per sample area to the nickel ferrite volume yielded a saturation magnetization of 290 emu/cm^3 , which is somewhat lower than the saturation magnetization of bulk nickel ferrite amounting to 330 emu/cm^3 .^[200] The total volume of nickel ferrite was approximated by assuming that the submicron nickel ferrite dots were cuboids with square bottom faces measuring 700 nm in edge length and a height of 150 nm. These cuboids were arranged in a hexagonal lattice pattern with a lattice constant of $1.5 \mu\text{m}$. In this way, the effective nickel ferrite layer thickness was estimated to 38 nm.

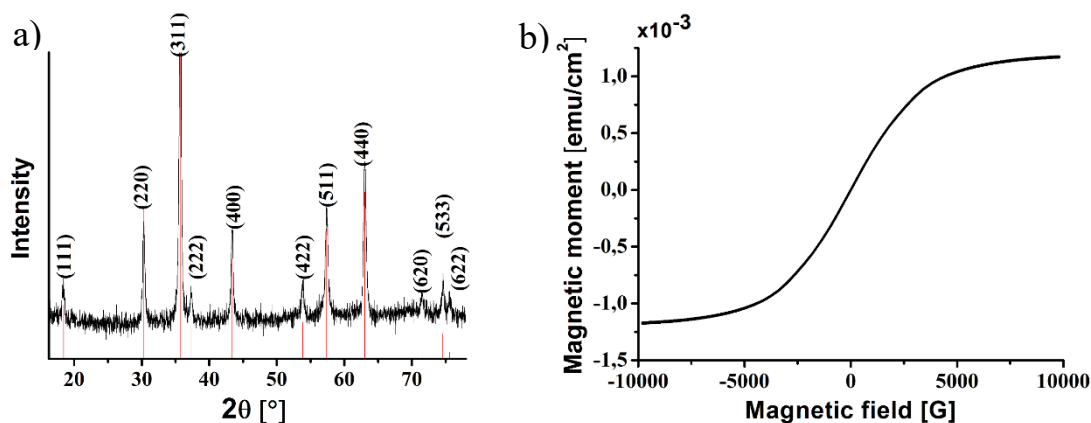
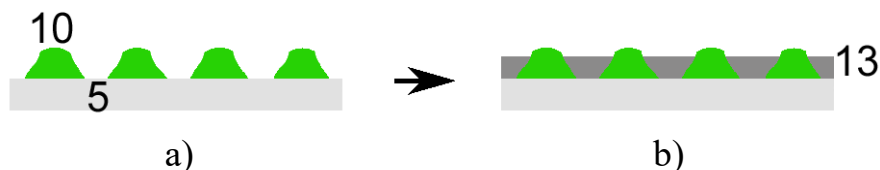


Figure 4.10: Characterization of submicron nickel ferrite dots obtained by solvothermal capillary stamping. a) XRD pattern of a powder of submicron nickel ferrite dots scrapped off from ITO substrates. The red lines indicate characteristic reflections of cubic NiFe_2O_4 ^[201] according to PDF card 01-074-2081 (Inorganic Crystal Structure Database). b) Magnetic moment per sample area of submicron nickel ferrite dots on an ITO substrate extending 1 cm² as function of an external magnetic field measured by VSM at 300 K.

Ordered monolayers of submicron nickel ferrite dots on ITO substrates were stamped to demonstrate the preparation of thin NiFe_2O_3 -Ni hybrid films by orthogonal substrate functionalization. Thus, additionally electrodeposited ~ 100 nm thick nickel layers on ITO substrates were modified with submicron nickel ferrite dots. The nickel was deposited onto the exposed ITO areas surrounding the submicron nickel ferrite dots (Figure 4.11 a,b). In this way, NiFe_2O_3 -Ni hybrid films consisting of an ordered monolayer of submicron nickel ferrite dots surrounded by a continuous nickel film with a thickness of ~ 100 nm were obtained (Figure 4.11c). Furthermore, the elemental distribution in NiFe_2O_3 -Ni hybrid films by energy-dispersive X-ray (EDX) spectroscopy were probed. It is challenging to map peaks representing the elements exclusively present in the nickel ferrite dots; oxygen is also contained in the ITO substrates, and the iron peaks were overlapped by much stronger nickel peaks. However, the number of nickel atoms per volume in the nickel ferrite dots is lower than in the surrounding pure nickel films. Therefore, in maps of the intensity of the Ni $L_{\alpha,2}$ peak the positions of the nickel ferrite dots are apparent as areas in which nickel is depleted (Figure 4.11d). The dependence of the magnetic moment per sample area of the NiFe_2O_3 -Ni hybrid film and the pure nickel film on an external magnetic field measured by VSM is displayed in Figure 4.11e. The

saturation values of the magnetic moment per sample area lying in the range from $3.3 \times 10^{-3} \text{ emu/cm}^2$ to $3.4 \times 10^{-3} \text{ emu/cm}^2$ were similar for the NiFe_2O_3 -Ni hybrid film and the pure nickel film. Rescaling the magnetic moment per sample area to the approximated sample volumes yielded saturation magnetizations of 350 emu/cm^3 for the pure nickel film and of 290 emu/cm^3 for the NiFe_2O_3 -Ni hybrid film. The volume of the latter was estimated by adding the effective nickel ferrite layer thickness of 38 nm obtained as described above to the effective thickness of the nickel layer amounting to 75 nm. The effective thickness of the nickel layer was approximated by assuming that a 100 nm thick nickel layer was electrodeposited onto the exposed areas of the ITO substrate not covered by nickel ferrite dots. The VSM curve of the NiFe_2O_3 -Ni hybrid film showed a more pronounced magnetization hysteresis than the VSM curve of the pure nickel film. While the pure nickel film reached the saturation magnetization already at external magnetic field strengths of $\pm 200 \text{ G}$, the NiFe_2O_3 -Ni hybrid film approached the saturation magnetization only at external field strengths of $\pm 1300 \text{ G}$. The coercive field strengths increased from $\pm 30 \text{ G}$ for the pure nickel film to $\pm 90 \text{ G}$ for the NiFe_2O_3 -Ni hybrid film. The remnant magnetic moment per sample area decreased from $3.1 \times 10^{-3} \text{ emu/cm}^2$ for the pure nickel film to $1.5 \times 10^{-3} \text{ emu/cm}^2$ for the NiFe_2O_3 -Ni hybrid film. Rescaling to the estimated sample volumes yielded remnant magnetizations of 310 emu/cm^3 for the pure nickel film and of 133 emu/cm^3 for the NiFe_2O_3 -Ni hybrid film. The squareness M_R/M_S of the magnetization hysteresis loops (ratio of the remnant magnetization M_R and the saturation magnetization M_S) amounted to ~ 0.91 for the pure nickel film and to ~ 0.45 for the NiFe_2O_3 -Ni hybrid film. Hence, the incorporation of ordered monolayers of nickel ferrite dots into a thin ferromagnetic nickel layers results in magnetic hardening of the latter.



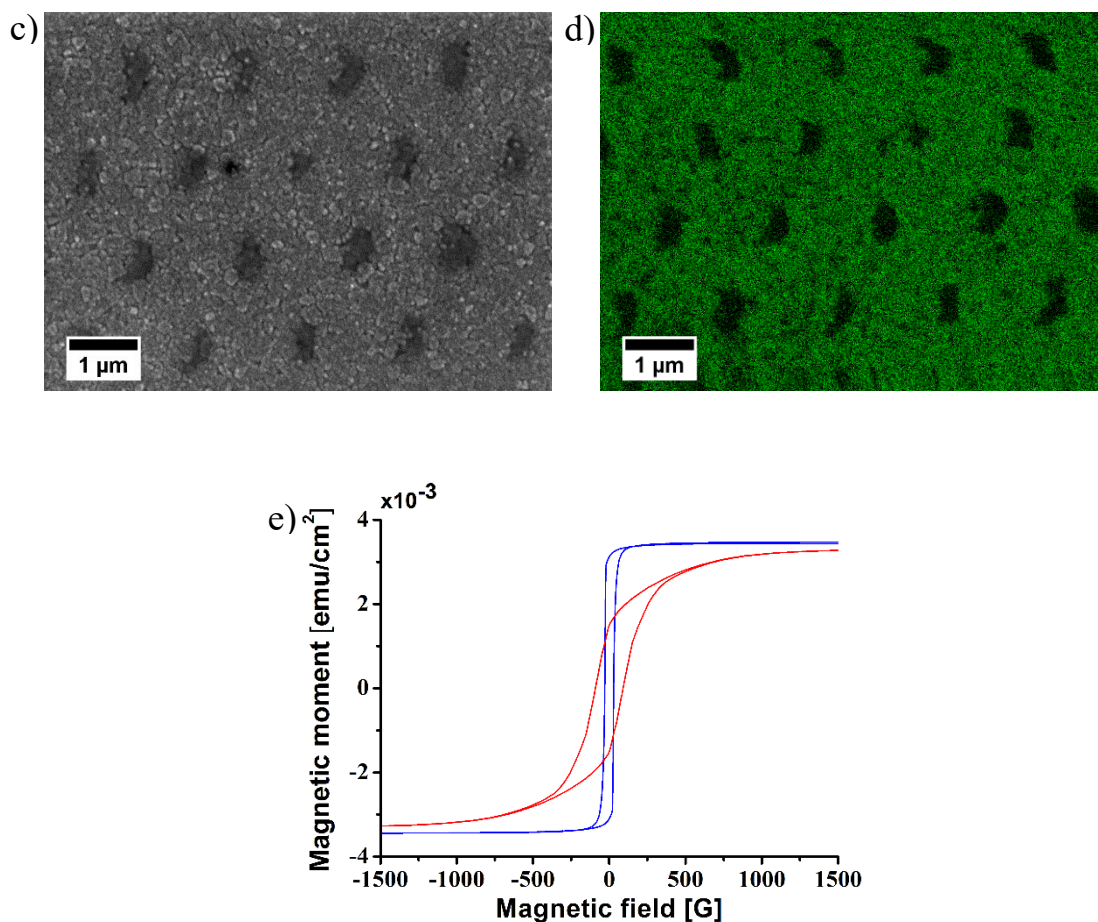


Figure 4.11: Thin NiFe₂O₃-Ni hybrid films. a) An ITO substrate (**5**) functionalized with an ordered monolayer of submicron nickel ferrite dots (**10**) is b) subjected to orthogonal functionalization by electrodeposition of nickel. Thus, NiFe₂O₃-Ni hybrid films (**13**) consisting of ordered monolayers of submicron nickel ferrite dots (**10**) surrounded by ~100 nm thick electrodeposited nickel films are obtained on ITO substrates (**5**). c) SEM image of a NiFe₂O₃-Ni hybrid film (**13**). d) EDX map of the Ni L_{α1,2} peak at 0.85 eV of a NiFe₂O₃-Ni hybrid film (**13**). Nickel ferrite dots (**10**) are located in areas where the nickel is depleted. e) Magnetic moments per sample area of a NiFe₂O₃-Ni hybrid film (**13**) (red) on an ITO substrate (**5**) and a ~100 nm thick continuous nickel film electrodeposited on an FDTS-coated ITO substrate (**5**) (blue) as function of an external magnetic field measured by VSM. The samples extended 1 cm². The magnetization measurements were carried out at 300 K.

4.4. Conclusion

So far, solvothermal syntheses and state-of-the-art lithography have by and large remained incompatible. Thus, the preparation of patterned thin films consisting of solvothermal synthesis products has remained challenging. Capillary stamping was demonstrated in autoclaves under solvothermal conditions enabling stamp-guided

conversion of precursors into solvothermal reaction products. The aerogel stamps used for this purpose were derived from a double-network hydrogel by solvent exchange and drying under subcritical ambient conditions. Precursor solutions imbibe the DNHG-derived aerogel stamps. Thus, liquid bridges form between the stamps' contact elements and the substrates to be patterned. Preferential evaporation of the solvent from the liquid bridges drags more precursor solution into the liquid bridges, where the precursors are enriched. Liquid-bridge guided solvothermal syntheses eventually yield submicron dots of the solvothermal reaction products in place of the liquid bridges. Therefore, solvothermal capillary stamping may yield device components comprising complex thin-layer architectures of solvothermal reaction products formed on functional substrates. Problems related to alternative sol-gel routes (high-temperature calcination steps) and direct serial ballistic deposition of the target materials (insufficient adhesion) are overcome. As example, arrays of submicron nickel ferrite dots having heights of ~ 150 nm on ITO substrates were generated. Subsequent orthogonal substrate functionalization by electrodeposition of nickel onto the exposed substrate areas surrounding the submicron nickel ferrite dots yielded thin nickel ferrite-nickel hybrid films consisting of a monolayer of submicron nickel ferrite dots surrounded by a continuous nickel layer. The submicron nickel ferrite dots halved the remanence of the ferromagnetic nickel film, while the saturation value of the magnetic moment per area remained by and large constant. Remanence engineering of thin ferromagnetic layers may help customize miniaturized transformers, positioning systems and electromechanical systems such as nanorelays. Solvothermal capillary stamping may pave the way for complex functional thin-film configurations so far predominantly accessible by combinations of layer transfer techniques, such as wafer bonding or ion slicing, and subtractive lithography. Orthogonal functionalization of substrates patterned by solvothermal capillary stamping may yield functional hybrid layers, in which the properties of the solvothermal reaction product and the second component are either synergistic or complementary.

**5. High-temperature stamping of molten functional polymers:
Orthogonal substrate functionalization for wettability
management**

5.1. Introduction

The wettability of surfaces determines their antifouling, antifogging, anti-icing and self-cleaning properties as well as their usability for sensing, oil-water separation, water collection and water purification.^[37-41] High-temperature capillary stamping of melts of stimuli-responsive polymers^[146] yielding arrays of stimuli-responsive polymer microdots on differently modified substrates enables the flexible generation of surfaces with switchable water contact angles (WCAs). High-temperature deposition of polymer melts circumvents problems associated with stamping polymer solutions, such as the handling of organic solvents, phase separation induced by solvent evaporation and capillarity-driven flow processes.^[148,202] Composite stamps with topographically patterned contact surfaces consisting of a metallic nickel core and a porous MnO₂ coating were used for taking up the polymer melts. The short transport ways from the MnO₂ contact layers to the counterpart substrates even allowed stamping melts of stimuli-responsive polymers containing carbon nanotubes (CNTs). The deposition of arrays of polymer-CNT hybrid microdot arrays instead of continuous films minimizes delamination and crack propagation. More importantly, orthogonal substrate modification between the microdots enables tuning the switching range of the stimuli-responsive polymers. For poly(2-(methacryloyloxy)ethyl ferrocenecarboxylate)-CNT hybrid microdot arrays by modification of the underlying indium tin oxide substrates with a PEO-terminated silane shifted the electrochemical WCA switching range by nearly 50°.

5.2. Experimental section

5.2.1. Chemicals and materials

Lithium perchlorate (LiClO₄), manganese sulfate (MnSO₄), nickel sulfate (NiSO₄), sodium acetate (C₂H₃NaO₂), sodium chloride (NaCl), boric acid (H₃BO₃), sodium dodecyl sulfate (NaC₁₂H₂₅SO₄; SDS), anisole (C₇H₈O), *tert*-butyl α -bromoisobutyrate (tBbib; C₈H₁₅BrO₂), copper (I) bromide (CuBr), pentamethyldiethylenetriamine

(PMDETA; $C_9H_{23}N_3$) and indium tin oxide (ITO) substrates [$(In_2O_3)_{0.9} \cdot (SnO_2)_{0.1}$ with a resistance of $8\text{--}12 \Omega \text{ sq}^{-1}$ and a thickness of $1200\text{--}1600 \text{ \AA}$] were purchased from Sigma-Aldrich. 3-[Methoxy(polyethyleneoxy) $_{6-9}$]propyltrichlorosilane $CH_3O(C_2H_4O)_{6-9}(CH_2)_3Cl_3Si$ (PEO-silane) was purchased from Gelest. Multiwalled CNTs (NC7000) were purchased from Nanocyl. Macroporous silicon^[185,192] with macropores $1 \mu\text{m}$ in diameter and a depth of 730 nm arranged in a hexagonal array with a lattice constant of $1.5 \mu\text{m}$ was purchased from Smart Membranes (Halle an der Saale). Pt wires were purchased from Rettberg Glasapparatebau and Ag/AgCl electrodes ($c(KCl): 3 \text{ mol L}^{-1}$) from Metrohm. Polyimide tape (heat resistant adhesive 1810-DS tape) was purchased from M&S Lehner GmbH. If not stated otherwise, chemicals and materials were used as received.

5.2.2. Synthesis and characterization of PFcMA

The details about the synthesis of PFcMA can be found in Elbert, Gallei et al.^[45] and Mazurowski, Gallei et al.^[86] The NMR spectrum of the obtained PFcMA was acquired at 400 MHz using a Bruker Avance II 400 spectrometer and processed with the software MestReNova (MetsreLab Research). The chemical shifts were referenced relative to the chemical shifts originating from the used deuterated solvent (Figure 5.1).

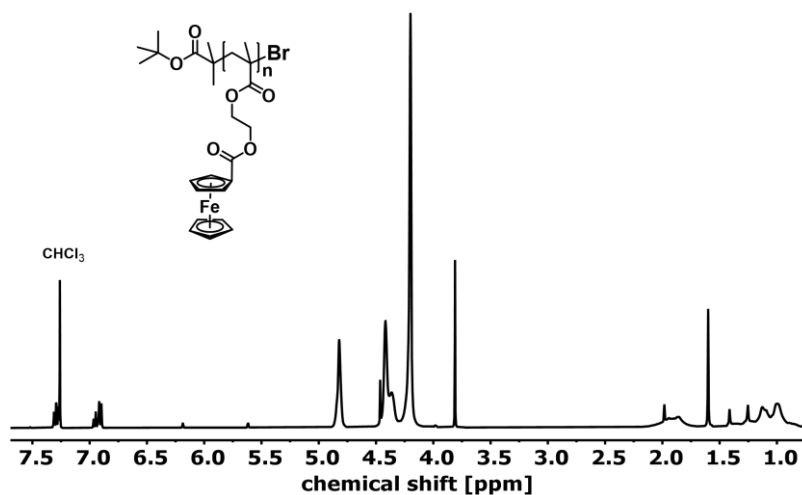


Figure 5.1: $^1\text{H-NMR}$ spectrum of as-synthesized PFcMA in CHCl_3 .

Size-exclusion chromatography (SEC) was carried out using an Agilent 1260 Infinity II setup with an SDV column set (1000 Å, 5000 Å, 6000 Å) from Polymer Standard Service (PSS, Mainz, Germany) and a PSS Security2 RI/UV detector. THF was used as the eluent at a flow rate of 1 mL/min and calibration was carried out using polystyrene standards (PSS, Mainz, Germany).

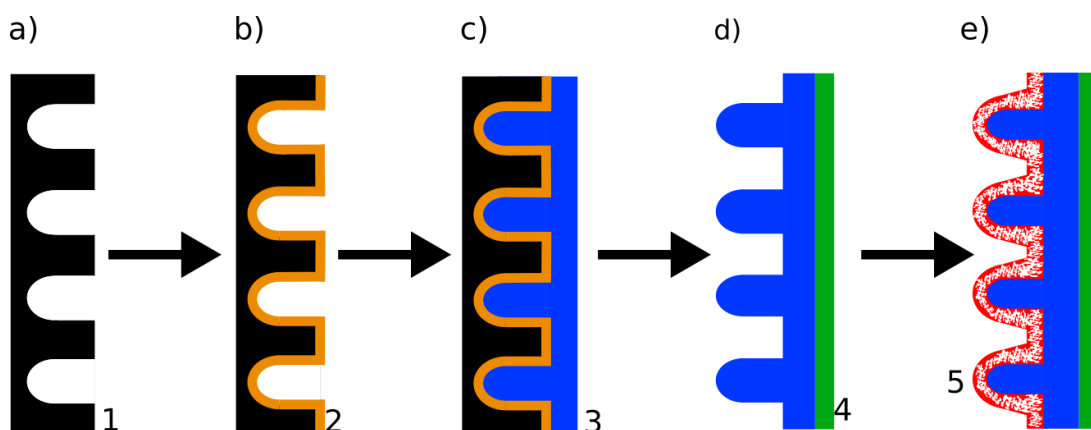


Figure 5.2: Preparation of Ni/MnO₂ composite stamps. a) Cross-sectional view of macroporous silicon (1; black) used as master template. b) Macroporous silicon coated with a thin gold layer (2; orange). c) Electrodeposition of nickel (3; blue) onto the gold-coated macroporous silicon. d) A heat-resistant adhesive polyimide tape (4, green) is glued on the flat exposed nickel surface and the nickel film supported by the polyimide tape is detached from the gold-coated macroporous silicon. e) A porous MnO₂ coating (5; red) is electrodeposited onto the topographically patterned surface of the nickel film initially in contact with the cold-coated macroporous silicon.

5.2.3. Preparation of Ni/MnO₂ composite stamps

Pieces of macroporous silicon^[185,192] extending 1 x 1 cm containing macropores with a diameter of 1 μm and a depth of 730 nm arranged in a hexagonal array with a lattice constant of 1.5 μm (Figure 5.2a) were sputtered 3 times with gold for 15 s using a JEOL JFC 1200 fine coater to generate an electrically conductive surface (Figure 5.2b). Electrodeposition of nickel was performed in 20 mL of an aqueous solution containing 1 mol/L NiSO₄, 0.1 mol/L NaCl, 0.4 mol/L H₃BO₃ and 0.15 mol/L SDS.^[203] A nickel plate was used as counter electrode and the gold-coated macroporous Si template as working electrode. The deposition was conducted with a current of 1 mA/cm² for 600 s followed

by rinsing with water and drying. Heat-resistant adhesive polyimide tape was glued onto the smooth exposed surface of the formed nickel films, which were then detached from the silicon master templates. Thus, nickel films with a thickness of 2 μm , which were topographically structured with hexagonal arrays of rods having a lattice constant of 1.5 μm at their exposed surface opposite of the adhesive polyimide tape were obtained. The rods were replicas of the macropores of the macroporous Si and had round tips, a height of 730 nm and base diameters of 1 μm . The adhesive polyimide tape mechanically stabilized the unsupported nickel films with an area of 1x1 cm^2 . In the next step, the topographically structured exposed surface of the nickel films was coated with a porous MnO_2 layer with a thickness of ~ 200 nm by electrodeposition using a three-electrode system with a platinum counter electrode and an Ag/AgCl reference electrode. The electrodeposition was carried out for 90 s in 20 mL of an aqueous electrolyte solution containing 0.33 mol/L MnSO_4 and 0.33 mol/L sodium acetate with a current of 0.5 mA/cm^2 following procedures reported elsewhere.^[100] All electrodeposition steps were performed with a potentiostat Interface 1000 (Gamry).

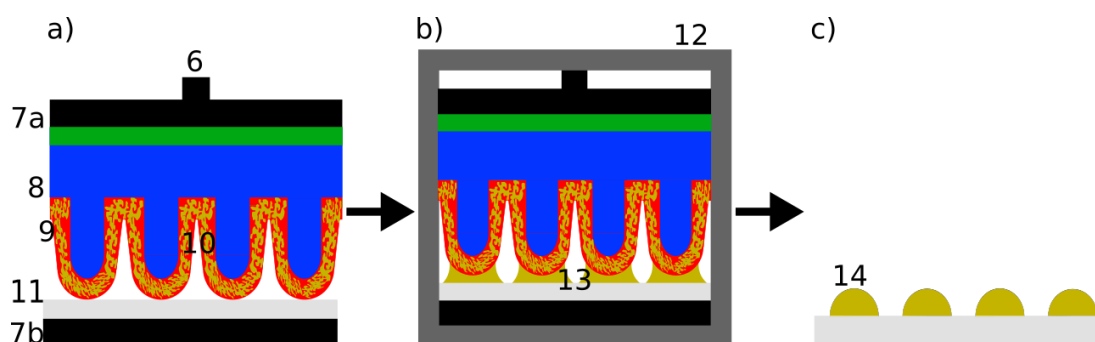


Figure 5.3: High temperature capillary stamping of molten PFcMA containing CNTs. a) The contact elements (10) of Ni/MnO₂ composite stamp (8) infiltrated with a PFcMA-CNT mixture attached to upper part (7a) of stamping device (7) approach ITO counterpart substrate (11) attached to lower part (7b) of stamping device (7). b) After insertion of stamping device (7) into vacuum furnace (12) and heating under Ar flow, the PFcMA-CNT mixture (9) forms liquid bridges (13) between the contact elements (10) and glass substrate (11). c) After detachment of Ni/MnO₂ composite stamp (8) using pin (6) and cooling to room temperature, substrate (11) is modified with submicron PFcMA-CNT hybrid microdots (14).

5.2.4. High temperature capillary stamping

As counterpart substrates to be patterned, ITO substrates were used. Some ITO substrates were surface-modified with PEO-silane before stamping by oxygen plasma treatment for 10 minutes using a Diener Femto plasma cleaner followed by chemical vapor deposition of PEO-silane at 110 °C for 12 h following procedures reported elsewhere.^[181] 10 μm of a solution of 10 mg PFcMA and 0.2 mg CNTs in 10 mL toluene was pipetted onto the topographically patterned MnO₂ surface of the Ni/MnO₂ composite stamps in such a way that the whole stamp area extending 1 cm² was covered with a PFcMA-CNT film. After evaporation of the toluene under ambient conditions the PFcMA-CNT mixture was further infiltrated into the pores of the MnO₂ layer at 190 °C for 10 h under a vacuum. The applied heating and cooling rates amounted to 20 K min⁻¹. For high-temperature capillary stamping, a procedure reported elsewhere was adapted.^[10] The flat nickel surface of the infiltrated Ni/MnO₂ composite stamps was glued onto the upper part of a stamping device with heat-resistant double-sided adhesive tape.

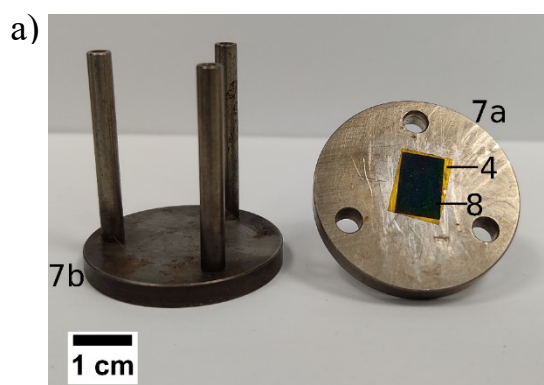




Figure 5.4: Stamping device (7). a) The MnO₂/Ni composite stamp (8) is attached to the upper part (7a) of stamping device (7) using heat-resistant polyimide adhesive tape (4). ITO substrate (11) (not shown) is located on lower part (7b) of stamping device (7). b) Assembled stamping device. The 3 pins of lower part (7b) inserted into the holes of upper part (7a) of stamping device (7) prevent an offset during high-temperature capillary stamping.

The counterpart substrate to be patterned was located on the lower part of the stamping device. The stamping device was then assembled by placing its upper part onto its lower part. A contact pressure of 3.9 kN/m² was exerted during the stamping process. The assembled stamping device was then transferred into a home-made precision vacuum furnace and heated to 190 °C at a rate of 20 K min⁻¹. The contact time at the target temperature of 190 °C amounted to 1 min. The upper part of the stamping device was then removed and the lower part with the counterpart substrate was cooled to room temperature at a rate of -20 K min⁻¹. All high-temperature steps were carried out under argon atmosphere. To check whether the stamping procedure had an impact on the molecular weight distribution of the PFcMA, molten PFcMA without CNTs, as described above, were stamped on ITO substrates, scraped off and used them for SEC measurements as described above.

5.2.5. Electrochemical analyses and treatments of PFCMA-CNT hybrid microdot arrays

For cyclic voltammetry ITO substrates with an area of 1 cm² functionalized with PFCMA-CNT hybrid microdots were used. The cyclic voltammetry measurements were performed in 20 mL of an aqueous electrolyte solution containing 0.1 mol/L LiClO₄ using a three-electrode setup with a platinum wire counter electrode and an Ag/AgCl reference electrode. The measurements were carried out at a scan rate of 20 mV s⁻¹. The oxidations and reductions of the PFCMA-CNT hybrid microdots for the investigation of electrochemical contact angle switching were also carried out electrochemically. Oxidation and reduction steps were performed by applying a constant potential of 1 or 0 vs. Ag/AgCl, respectively, for 30 min in the setup described above.

5.2.6. Microscopic characterization of PFCMA-CNT hybrid arrays

For imaging by scanning electron microscopy (SEM), the samples were dried overnight at 40 °C in air and then sputter-coated 2-3 times for 15 s with platinum/iridium alloy using an EMITECH K575X sputter coater. SEM images were taken with a Zeiss Auriga device equipped with a field emission cathode and a Gemini column at a working distance of 5 mm applying an acceleration voltage of 3 kV. For image detection an InLens detector was used. Atomic force microscopy (AFM) topography images were recorded with an NTEGRA microscope (NT-MDT) in the tapping mode using HQ:NSC16/AL BS cantilevers from µmasch with a resonance frequency of 170 - 210 kHz and a force constant of 30 - 70 N/m.

5.2.7. Surface analysis by X-ray photoelectron spectroscopy

X-ray photoelectron spectroscopy measurements were carried out under ultra-high vacuum using an ESCA system Phi 5000 VersaProbe III with a base pressure of 1•10⁻⁹ mbar equipped with a monochromatized aluminum anode (K α = 1486.6eV) and a 32-channel electrostatic hemispherical electronic analyzer. An ion gun and an electron gun

were used to prevent sample charging. A take-off angle of 45° was used. The XP spectra were calibrated using the carbon C 1s peak at 284.5 eV.^[204] Lorentz fits of the XP spectra were obtained using the software Origin.

5.2.8. Investigations of wettability and evaporation dynamics

Water contact angles (WCAs) were measured by the sessile drop method with a DSA100 drop shape analyzer at 22 °C and a relative humidity of 23 %. All data points represent the average of 3 measurements at different sample positions. The imaging of the contact lines of evaporating sessile water droplets was carried out using an optical microscope Di-Li 1027. To this end, droplets of deionized water with an initial volume of 2 µL were deposited on the sample surfaces. All experiments were carried out at 23 °C at a relative humidity of 31 %.

5.3. Results and discussion

5.3.1. High-temperature capillary stamping

The Ni/MnO₂ composite stamps for high-temperature capillary stamping combined sufficient mechanical stability, stability at high temperatures, good heat conductivity and the capability of taking up sufficient amounts of the polymer melts to be transferred. Furthermore, high-temperature capillary stamping should enable the deposition of mixtures containing components not able to flow, such as nanocomposites or mixtures of molten polymers and CNTs. Therefore, the transport paths should be shorter as in fully porous stamps, such as the aerogel stamps reported previously, which may also be used at elevated temperatures.^[10] The Ni/MnO₂ composite stamps devised here with an area of 1 cm² contained nickel layers prepared by electrodeposition of nickel into macroporous silicon templates^[185,185,192,192] adapting procedures reported elsewhere (Figure 5.2a-e).^[203] The surface of the ~2 µm thick nickel layers in contact with the macroporous silicon is patterned with arrays of nickel rods, which are negative replicas of the macropores of the macroporous silicon templates. Thus, the nickel rods arranged in hexagonal arrays with a

nearest-neighbor distance of 1.5 μm have a diameter of 1 μm , a height of 730 nm and hemispherical tips (Figure 5.5a). The nickel substrates exhibit the thermal conductivity well as the mechanical properties^[205] typical of nickel. These properties were combined with those of a ~ 200 nm thick porous MnO_2 layer with pore diameters of ~ 20 nm (Figure 5.5b,c) electrodeposited onto the topographically patterned nickel surface by adapting procedures reported elsewhere (Figure 5.2e).^[100] As a result, Ni/ MnO_2 composite stamps having a topographically patterned porous MnO_2 contact surface were obtained. The topographic patterns of the contact surfaces consisted of arrays of rod-like contact elements with a height of ~ 730 nm and a diameter of 1.2 μm arranged in a hexagonal lattice with a lattice constant of 1.5 μm (Figure 5.5b,c). The porous MnO_2 layer takes up the PFCMA-CNT mixtures and stores them close to the contact surface of the Ni/ MnO_2 composite stamps.

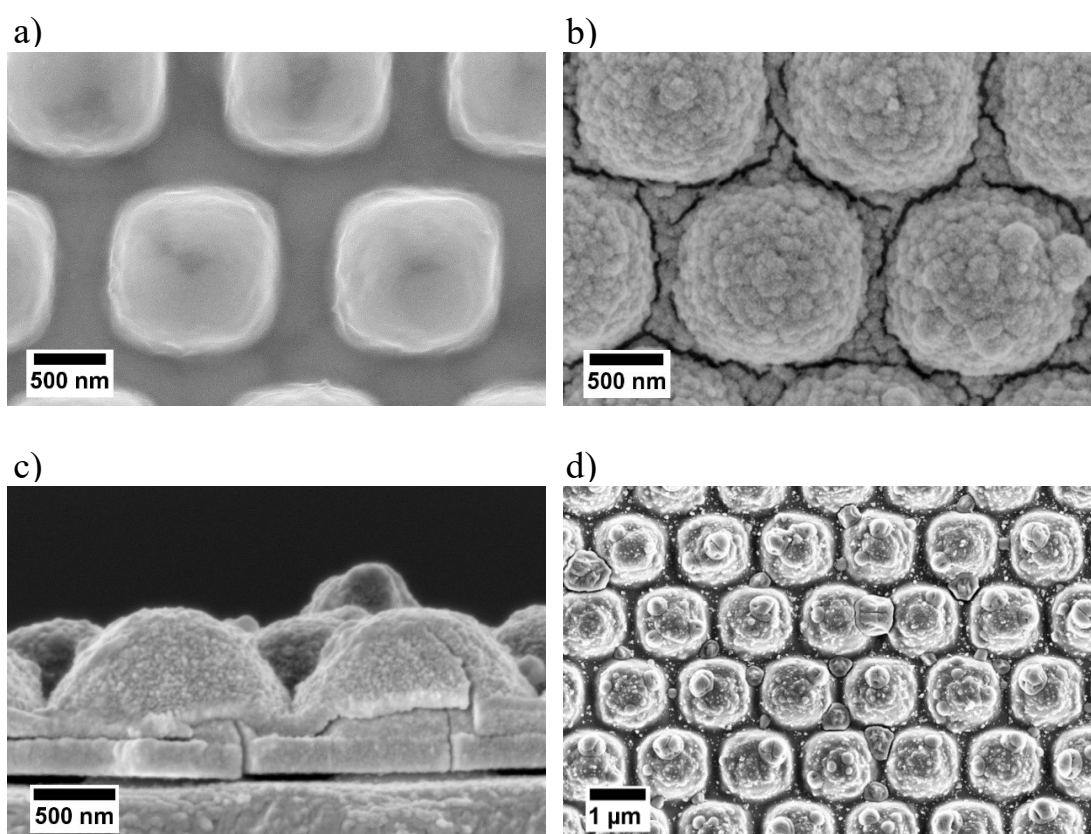


Figure 5.5: SEM images of Ni/ MnO_2 composite stamps (**8**). a) Topographically patterned nickel layer (**3**) prior to electrodeposition of MnO_2 (**5**). b) Topographically patterned surface and c) cross section of a Ni/ MnO_2 composite stamp (**8**). d) SEM image of the contact surface of a Ni/ MnO_2 composite stamp after high-temperature capillary stamping.

Using Ni/MnO₂ composite stamps, PFcMA melts containing CNTs were stamped onto either pristine ITO substrates or ITO substrates whose surface had been modified with PEO-silane at 190 °C under an argon atmosphere. The contact time amounted to ~9.5 min including the heating ramp and a dwell time of 1 min at the target temperature. Liquid bridges consisting of PFcMA melts mixed with CNTs connecting the contact elements of the Ni/MnO₂ composite stamps and the surfaces of the ITO counterpart substrates were formed (Figure 5.3a,b). After detachment from the ITO counterpart substrates and cooling to room temperature, the Ni/MnO₂ composite stamps were still intact (Figure 5.5d) and could be reused several times without replenishment. On the ITO counterpart substrates arrays of PFcMA-CNT hybrid microdots typically extending 1 cm² – corresponding to the area of the contact surface of the Ni/MnO₂ composite stamps – were deposited (Figure 5.9). As expected, the geometry of the arrays of PFcMA-CNT hybrid microdots mirrors the contact topography of the Ni/MnO₂ composite stamps. Thus, the nearest-neighbor distance between the PFcMA-CNT hybrid microdots amounted to 1.5 μm. Their diameter amounted to ~800 nm (Figure 5.10a) and their height to ~250 nm (Figure 5.10b,c). Stamping of pure PFcMA melts without CNTs onto an pristine ITO substrate under exactly the same conditions as described above yielded PFcMA microdots with diameters and heights by and large identical to those of the PFcMA-CNT hybrid microdots (Figure 5.6a,b).

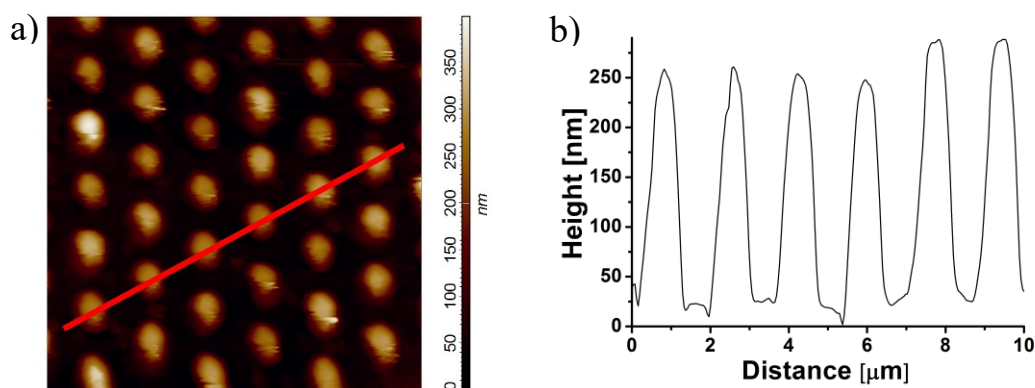


Figure 5.6: a) AFM topography image of pure PFcMA microdots on a pristine ITO substrate. b) Topographic height profile along the red line in panel a). The image fields extend 10 x 10 μm².

Also, stamping of PFCMA-CNT mixtures onto ITO substrates modified with PEO-silane otherwise under the same conditions as described above did not perceptibly alter diameter and height of the PFCMA-CNT hybrid microdots (Figure 5.7a,b).

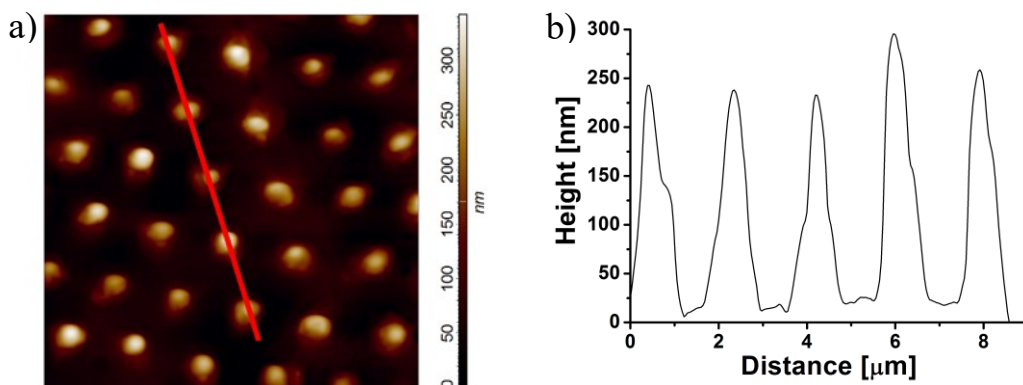


Figure 5.7: a) AFM topography image of PFCMA-CNT hybrid microdots on an ITO substrate coated with PEO-silane. b) Topographic height profile along the red line in panel a). The image fields extend $10 \times 10 \mu\text{m}^2$.

It should finally be noted that the molecular weight distribution of PFCMA subjected to the high-temperature capillary stamping procedure described above remained unaltered, as revealed by size exclusion chromatography (Figure 5.8).

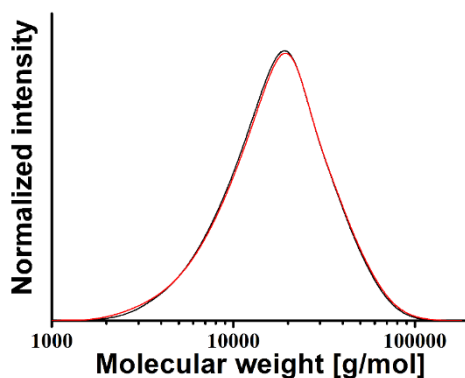


Figure 5.8: Molecular weight distribution of as-synthesized bulk PFCMA (black) and PFCMA microdots obtained by high-temperature capillary stamping of PFCMA melts conducted in the same way as high-temperature capillary stamping of PFCMA-CNT mixtures (red) obtained by SEC measurements.

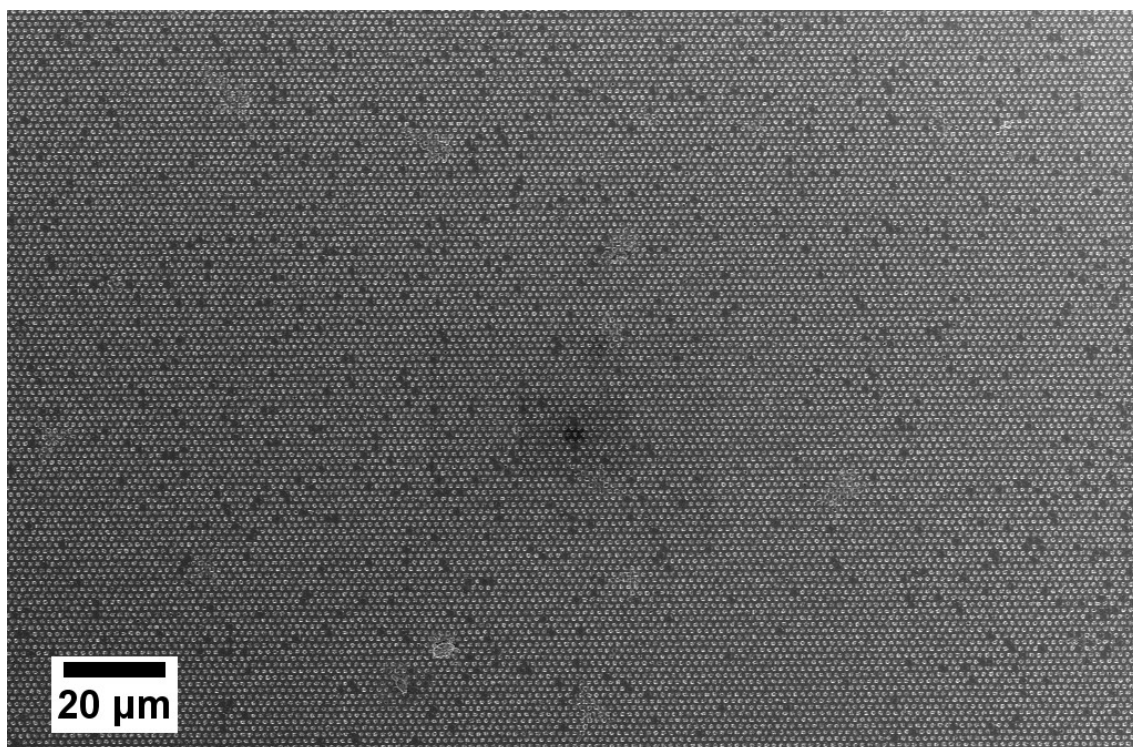


Figure 5.9: Large-field SEM top-view image of an array of PFCMA-CNT hybrid microdots on an ITO substrate obtained by high-temperature capillary stamping.

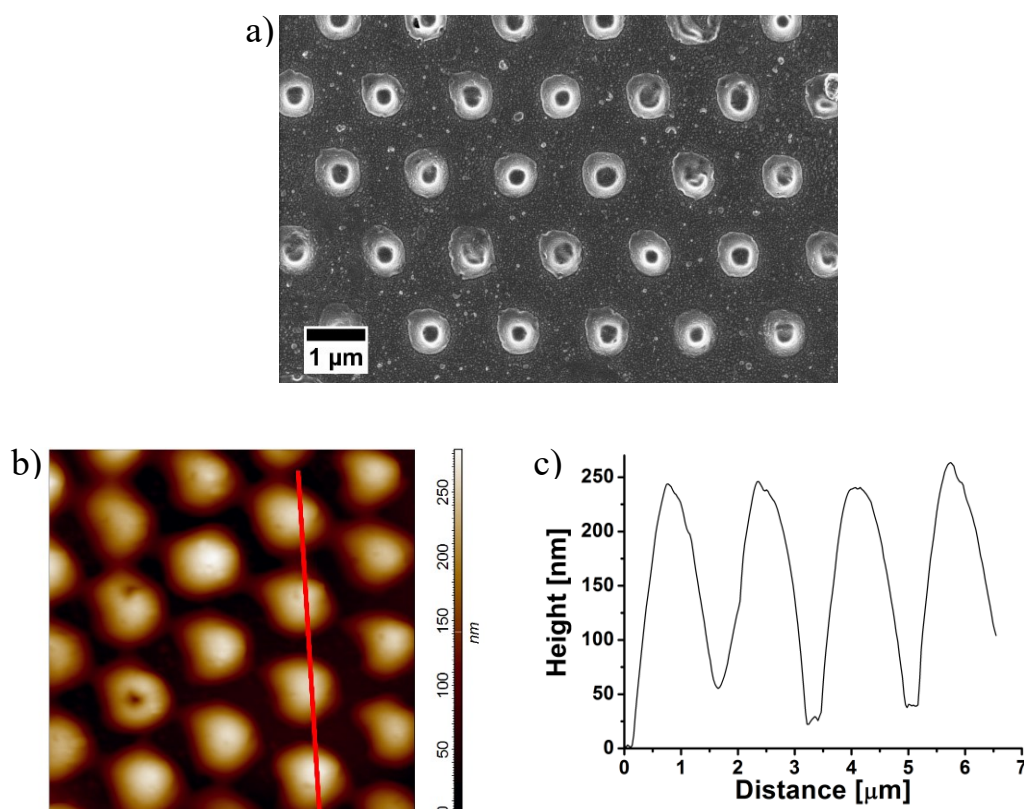


Figure 5.10: Arrays of PFCMA-CNT hybrid microdots on non-modified ITO substrates produced by high-temperature capillary stamping of PFCMA melts containing CNTs. a) SEM image. b) AFM topography image (the image field extends $8 \times 8 \mu\text{m}^2$). c)

Topographic height profile along the red line in panel c).

The impact of the CNTs on the electrochemically induced oxidation and reduction of the PFCMA in PFCMA-CNT hybrid microdots and microdots consisting of pure PFCMA stamped onto pristine ITO substrates was evaluated by cyclic voltammetry. PFCMA-CNT hybrid microdots display narrow and pronounced oxidation and reduction peaks with a peak separation of 220 mV, a maximum oxidation current of 47 μA and a reduction current of 53 μA (Figure 5.11a). Pure PFCMA microdots also undergo electrochemical oxidation and reduction (Figure 5.11b). However, the oxidation and reduction peaks are less pronounced because of the lower conductivity of the PFCMA microdots in the absence of CNTs. The apparently larger peak separation can thus hardly be quantified. The oxidation current amounted to 17 μA . Therefore, the presence of CNTs in the PFCMA microdots accounts for a significant improvement of their electrochemical response.

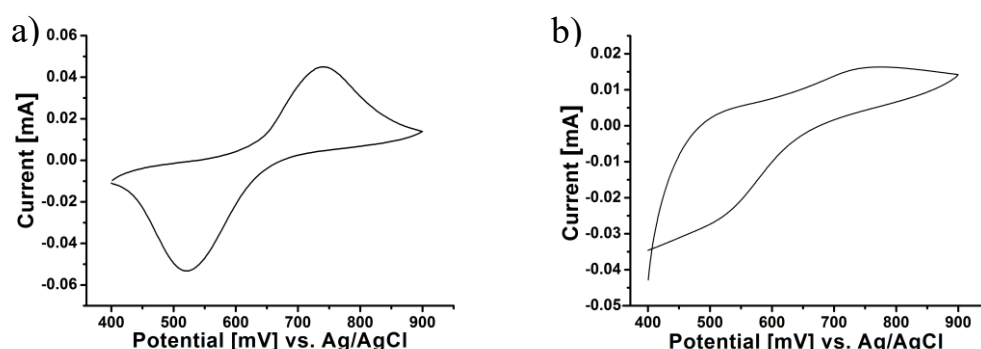


Figure 5.11: Cyclic voltammetry of a) PFCMA-CNT hybrid microdot arrays and b) arrays of pure PFCMA microdots deposited on non-modified ITO substrates extending 1 cm^2 by high-temperature capillary stamping

5.3.2. Wettability switching

The wettability of pristine ITO substrates and ITO substrates surface-modified with PEO-silane, which had been patterned with PFCMA-CNT hybrid microdots were investigated. To evaluate the impact of the electrochemical switching of the PFCMA-CNT hybrid microdots on the WCAs, five successive electrochemical switching cycles from the reduced state to the oxidized state and *vice versa* were performed. The apparent WCA

measured here does not correspond to the equilibrium WCA or to the Young WCA.^[156] However, it is assumed that it reasonably represents the practical wettability of PFcMA-CNT hybrid microdot arrays under operating conditions. The WCA for PFcMA-CNT hybrid microdot arrays on pristine ITO substrates in the reduced state amounted to $112^\circ \pm 1^\circ$ and in the oxidized state to $94^\circ \pm 2^\circ$ (Figure 5.13a-c). Deposition of the PFcMA-CNT hybrid microdots onto ITO substrates modified with PEO-silane resulted in the reduction of the WCAs by nearly 50° . Thus, a WCA of $65^\circ \pm 1^\circ$ was obtained for the reduced state and of $46^\circ \pm 1^\circ$ for the oxidized state (Figure 5.13d). X-ray photoelectron spectroscopy (XPS) indicated that the PEO-silane coating in the ITO substrate was still intact after five electrochemical oxidation-reduction cycles (Figure 5.12).

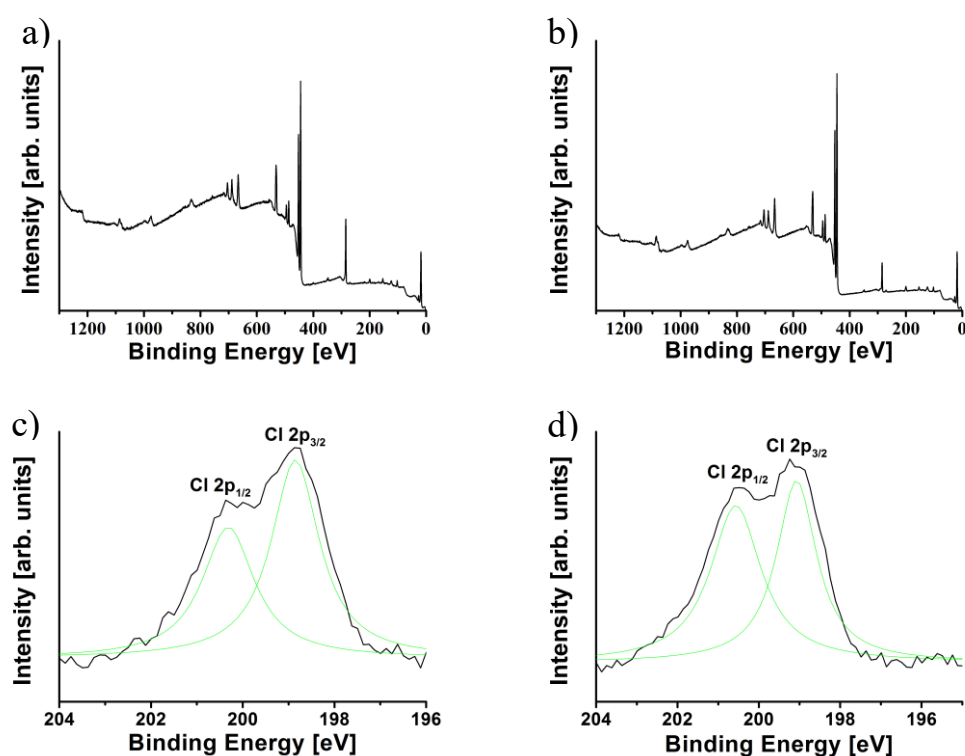
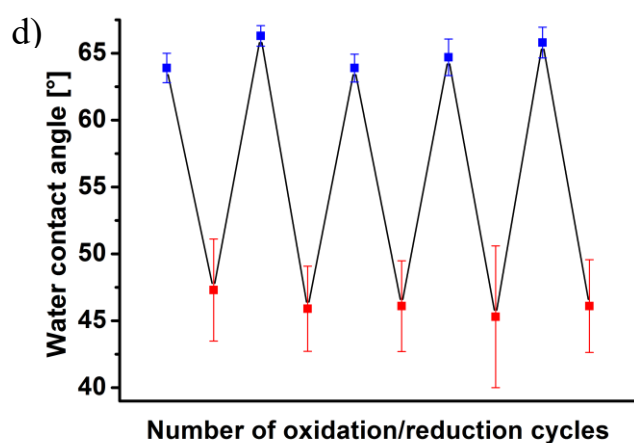
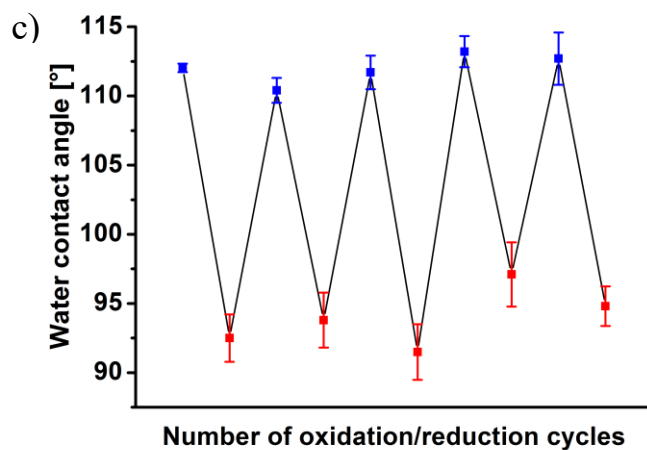
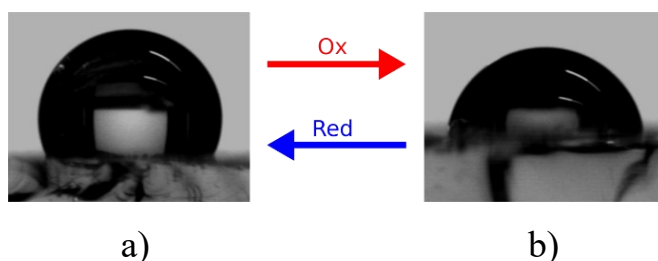


Figure 5.12: XP spectra of ITO substrates modified with PEO-silane a) before any treatment and b) after five treatments simulating the oxidation-reduction cycles applied to electrochemically switch PFcMA-CNT hybrid microdots. c), d) High resolution XP spectra of the binding energy range, in which the Cl 2p peaks at ~ 199 eV appear, c) before and d) after five simulated oxidation-reduction cycles. The XP spectra were measured with a take-off angle of 45° .

For a continuous PFcMA film spin-coated on an ITO substrate a WCA of $103^\circ \pm 1^\circ$ for

the reduced and of $75^\circ \pm 3^\circ$ for the oxidized state was obtained (Figure 5.13e). In the course of the five successive electrochemical switching cycles no significant systematic change in the WCA values was apparent.



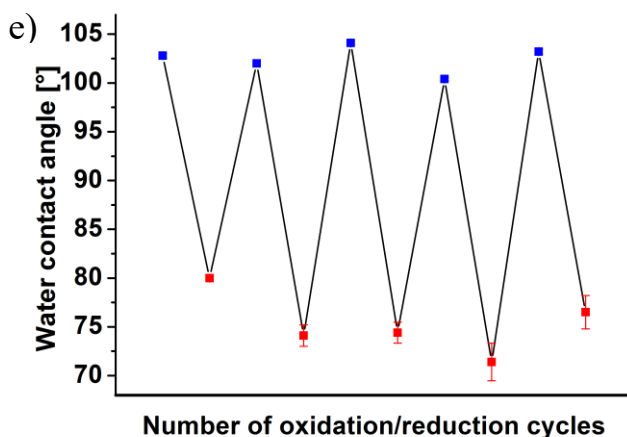


Figure 5.13: Electrochemical wettability switching of ITO substrates functionalized with PFCMA-CNT hybrid microdot arrays. Blue denotes the reduced and red the oxidized state. a), b) Sessile water droplets on pristine ITO substrates functionalized with PFCMA-CNT hybrid microdot arrays. The PFCMA is a) in the reduced and b) in the oxidized state. The image widths correspond to 3 mm. c)-d) WCAs of sessile water droplets on c) a pristine ITO substrate patterned with a PFCMA-CNT hybrid microdot array, d) on an ITO substrate modified with PEO-silane followed by patterning with PFCMA-CNT hybrid microdot arrays and e) a continuous PFCMA film with a thickness of 300 nm spin-coated on an ITO substrate.

Finally, the evaporation of sessile water droplets deposited onto ITO substrates functionalized with PFCMA-CNT hybrid microdot arrays was monitored because droplet evaporation crucially impacts technical relevant processes such as ink-jet printing, pesticide spraying, spin coating, and biochemical sensing.^[206,207] The WCAs and the relative contact radii $r^* = r_e / r_0$, where r_e is the contact radius after the elapsed evaporation time t_e and r_0 the initial contact radius of the considered water droplet, were captured as a function of the relative evaporation time $t^* = t_e / t_c$, where t_c is the time required for complete evaporation.

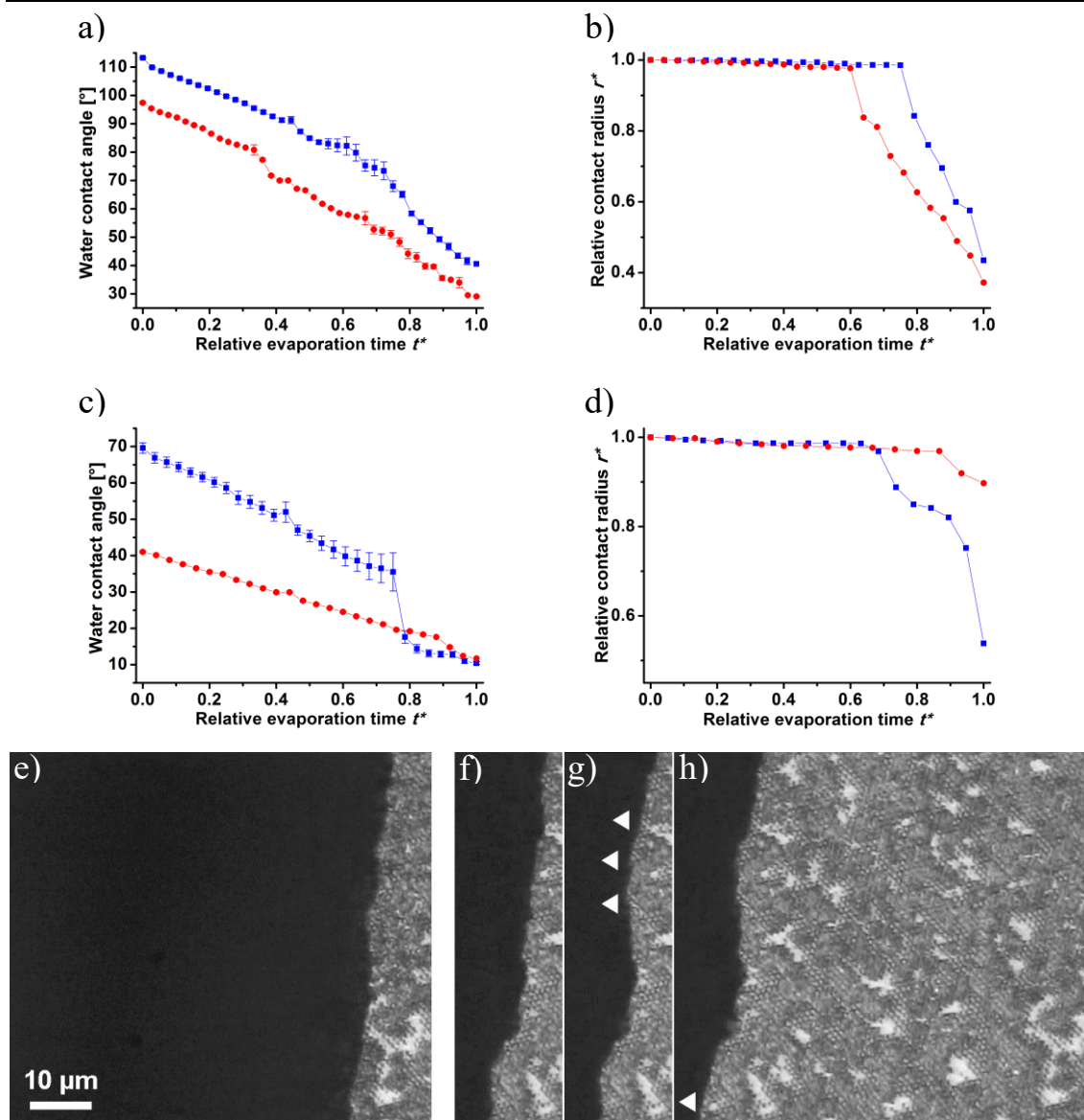


Figure 5.14: a),c) WCAs and b),d) relative contact radii $r^* = r_e/r_0$ of evaporating sessile water droplets with an initial volume of 2 μ L plotted against the relative evaporation time $t^*=t_e/t_c$, where r_e is the contact radius of the considered water droplet after the elapsed evaporation time t_e , r_0 the initial contact radius and t_c the time required for complete evaporation. The sessile water droplets were located on PFCMA-CNT hybrid microdot arrays stamped onto a),b) pristine ITO substrates and c),d) ITO substrates coated with PEO-silane. Blue squares represent data points obtained with reduced and red circles data points obtained with oxidized PFCMA. e) – h) Optical microscopy images of the contact line of an evaporating sessile water droplet with an initial volume of 2 μ L deposited on ITO substrate patterned with an array of PFCMA-CNT hybrid microdots (PFCMA in the reduced state) taken at e) $t^* \approx 0.24$ and f)-h) successively at $t^* \approx 0.32$. All experiments were carried out at 23 °C at a relative humidity of 31%.

Figure 5.14 a shows the WCAs of sessile water droplets with an initial volume of 2 μ L as a function of t^* on PEO-silane-coated ITO substrates functionalized with PFCMA-CNT

hybrid microdot arrays. The WCAs decreased from 69° (reduced state; blue squares) and 41° (oxidized state; red circles) to $\sim 10^\circ$ at $t^* = 1$ (Figure 5.14a). As shown in Figure 5.14b, r^* remains nearly constant up to t^* values of 0.7 for the reduced state and 0.9 for the oxidized state. At $t^* = 1$, r^* amounted to 0.6 for the reduced state and to 0.95 for the oxidized state. For pristine ITO substrates functionalized with PFcMA-CNT hybrid microdot arrays the WCAs for the reduced and oxidized states nearly linearly decreased from 113° and 98° at $t^* = 0$ to 50° and 40° at $t^* = 1$ (Figure 5.14c). Figure 5.14d shows the corresponding dependence of r^* on t_e . For both cases, r^* remains nearly constant until t^* values of 0.6 (oxidized state) and 0.8 (reduced state) are reached. In both cases a r^* value of ~ 0.4 was reached at $t^* = 1$.

The ccr behaviour from Figure 5.14b can also be seen in the microscopy images Figure 5.14e-h. The contact radius remains constant at first and decreases continuously after approx. 15 minutes. Since the microscopy images do not show exactly when the water droplet evaporates completely, t^* cannot be determined exactly.

5.4. Conclusion

Wettability management is crucial for the design of surfaces with optimized antifouling, antifogging, anti-icing and self-cleaning properties as well as for applications such as sensing, oil-water separation, water collection and water purification. Stimuli-responsive polymers have attracted significant interest to tailor and to switch the wetting properties of surfaces. In some scenarios, stimuli-responsive polymers may be chemically grafted onto substrates. However, non-reactive deposition significantly extends the range of the deployable stimuli-responsive polymers and of the substrates to be patterned. Continuous thin films of stimuli-responsive polymers accessible by standard methods such as spin coating and dip coating may also be prone to crack propagation and delamination. This problem may be mitigated by the deposition of arrays of discrete microdots of the stimuli-responsive polymers. More importantly, orthogonal substrate functionalization in the substrate areas between the microdots is possible, resulting in either synergistic or

complementary interplay of the properties of the stimuli-responsive polymer and the second functional component. Thus, arrays of hybrid microdots consisting of the stimuli-responsive polymer PFCMA and CNTs by high-temperature capillary stamping at elevated temperatures where the PFCMA is molten were generated. PFCMA-CNT hybrids are known to show electrochemically switchable wettability. The stamping of melts prevents problems associated with the use of polymeric solutions such as the precautions to be considered in the presence of organic solvents. Moreover, in polymer solutions and hardly controllable structure formation processes, such as phase separation induced by solvent evaporation and capillarity-driven flow processes, may occur. For high-temperature capillary stamping specifically designed composite stamps with a topographically patterned contact surface consisting of a nickel core and a MnO₂ coating were used. The latter takes up the PFCMA melt containing the CNTs. The short transport lengths related to this design even allow stamping inks containing components impeding flow, such as CNTs. The electrochemical switching range of the water contact angle on arrays of PFCMA-CNT hybrid microdots deposited on ITO substrates by high-temperature capillary stamping could be shifted by nearly 50° depending on the orthogonal functionalization of the ITO substrates between the microdots with suitable silanes.

6. Summary

This work focuses on the orthogonal substrate functionalization using additive contact lithography. New contact lithography methods and new mesoporous stamps were developed in order to generate functional films under different ambient conditions. Via orthogonal modification, hybrid films were generated to enhance or tune the properties of the stamped, functional materials. The effect of the orthogonal modification of the functional films can be additive or synergistic.

Microstructured LiNbO_3 films on indium tin oxide (ITO) substrates were generated by direct stamping with a polystyrene-*block*-poly(2-vinylpyridine) (PS-*b*-P2VP) stamp of an aqueous precursor solutions containing lithium acetate ($\text{C}_2\text{H}_3\text{LiO}_2$) and niobium oxalate hydrate ($\text{C}_{10}\text{H}_5\text{NbO}_{20} \cdot 6 (\text{H}_2\text{O})$). These lithium and niobium sources are cheap and commercially available compounds that can simply be dissolved in water without further precautions. Moreover, their reaction produces, apart from LiNbO_3 , only volatile by-products that evaporate. Calcination of the stamped precursor film leads to patterned LiNbO_3 films containing regular arrays of holes (hole diameter $\sim 1 \mu\text{m}$, pitch $\sim 1,5 \mu\text{m}$), in which the ITO substrate was exposed. The holey LiNbO_3 films showed uniform second harmonic output except at the positions of the macropores of the holey film. The holey nature of the LiNbO_3 film enabled orthogonal substrate functionalization with gold via electrodeposition at the position of the holes, which resulted in an increase in the second harmonic output intensity by a factor of 5.4. A major problem of additive contact lithography by using a PS-*b*-P2VP stamp is the mechanical instability of the stamp or deformation of the contact elements.

Certain functional materials like ferrites are preferably synthesized in autoclaves under solvothermal conditions because they are difficult to attain under ambient conditions. While traditional porous stamps are not suitable for solvothermal synthesis, DNHG-derived aerogel stamps overcome this problem because DNHGs, which combine a hard but brittle network with a soft and ductile network, contain continuous mesopore systems but exhibit nevertheless excellent mechanical strength. Moreover, the DNHG synthesis

used in this work can easily be combined with standard replication molding. Thus DNHG-derived aerogel stamps, which do not only retain the excellent mechanical properties of DNHGs but are also characterized by the presence of continuous mesopore systems and by contact surfaces topographically patterned with contact elements were synthesized. Hence, the DNHG-derived aerogel stamps can be used for parallel additive contact lithography under solvothermal conditions and enable the generation of patterns of solvothermal reaction products by stamp-guided solvothermal conversion of their precursors taking advantage of the enrichment of the precursors in the volume between the contact elements and a counterpart substrate. The DNHG-derived aerogel stamps were used for the preparation of thin nickel ferrite-nickel ($\text{NiFe}_2\text{O}_3\text{-Ni}$) hybrid layers consisting of a regular monolayer of submicron nickel ferrite dots embedded in a continuous nickel film. Capillary stamping with DNHG-derived aerogel stamps combined with a solvothermal synthesis based on ethanolic solutions of iron(III)-acetylacetonate ($\text{Fe}(\text{C}_5\text{H}_7\text{O}_2)_3$) and nickel(II)-acetylacetonate ($\text{C}_{10}\text{H}_{14}\text{NiO}_4$)^[35,36] yielded arrays of submicron nickel ferrite dots on indium tin oxide (ITO) substrates. Then, the ITO substrates functionalized with ordered monolayers of submicron nickel ferrite dots were further orthogonally functionalized with metallic nickel by electrodeposition. The superparamagnetic submicron nickel ferrite dots halved the magnetic remanence of the thin ferromagnetic nickel film, while the saturation value of the magnetic moment per area remained by and large unaffected.

The DNHG-derived aerogel stamp tends to degrade and change his morphology at higher temperatures and can therefore only be used at moderate temperatures. Consequently, the stamp cannot be used at higher temperatures, for example to stamp solvent free polymers from the melt. For this purpose, metallic hybrid stamps made of Ni/MnO₂ were generated. The stamping method permits the flexible on-demand manufacturing of tailored surfaces with switchable wettability by additive lithographic high-temperature deposition of molten stimuli-responsive polymers. As example, arrays of poly(2-(methacryloyloxy)ethyl ferrocenecarboxylate with multiwalled carbon nanotubes (CNTs) PFcMA-CNT hybrid microdots with a diameter of 800 nm, a height of 250 nm and a

lattice of 1.5 μm onto conductive indium tin oxide (ITO) substrates were stamped. Electrochemical WCA switching reversibly transformed the PFcMA-CNT hybrid microdots from a high-WCA state, in which the PFcMA is reduced, to a low-WCA state, in which the PFcMA is oxidized (the ferrocene units are positively charged), and *vice versa*. Orthogonal substrate functionalization of the areas around the PFcMA-CNT hybrid microdots with 3-[Methoxy(polyethyleneoxy)₆₋₉]propyltrichlorosilane $\text{CH}_3\text{O}(\text{C}_2\text{H}_4\text{O})_6-9(\text{CH}_2)_3\text{Cl}_3\text{Si}$ (PEO-silane) via chemical vapor shifted the WCA switching range by nearly 50°.

In summary, the novel stamps and stamping processes enable the production of thin layers of functional materials under special conditions due to the special properties of the stamps, which was previously not possible. Likewise, through the orthogonal modification of the stamped thin layers, physical effects of different materials can be combined, resulting in interesting applications in the field of nanotechnology.

Literature

- [1] H. Krishna, R. Kalyanaraman. Functional Nanostructured Thin Films, Functional Nanostructures, *Springer*, **2008**, p. 65.
- [2] A. Yamashita, T. Hayashi, Organic molecular beam deposition of metallophthalocyanines for opto-electronics applications, *Advanced Materials* **1996**, *8*, 791.
- [3] S. R. Forrest, The path to ubiquitous and low-cost organic electronic appliances on plastic, *Nature* **2004**, *428*, 911.
- [4] E. B. Cooper, S. R. Manalis, H. Fang, H. Dai, K. Matsumoto, S. C. Minne, T. Hunt, C. F. Quate, Terabit-per-square-inch data storage with the atomic force microscope, *Applied Physics Letters* **1999**, *75*, 3566.
- [5] A. S. Aricò, P. Bruce, B. Scrosati, J.-M. Tarascon, W. van Schalkwijk, Nanostructured materials for advanced energy conversion and storage devices, *Nature Materials* **2005**, *4*, 366.
- [6] D. Rosenthal, Functional surfaces in heterogeneous catalysis: A short review, *Physica Status Solidi a-Applied Research* **2011**, *208*, 1217.
- [7] E. T. Slonecker, D. B. Jennings, D. Garofalo, Remote sensing of impervious surfaces: A review, *Remote Sensing Reviews* **2001**, *20*, 227.
- [8] A. M. EL-Refaie, T. M. Jahns, Optimal Flux Weakening in Surface PM Machines Using Fractional-Slot Concentrated Windings, *IEEE Transactions on Industry Applications* **2005**, *41*, 790.
- [9] F. Alarслан, L. Vittadello, J. Klein, Q. A. Khan, C. Kijatkin, M. Haase, H. Schäfer, M. Imlau, M. Steinhart, Thin Patterned Lithium Niobate Films by Parallel Additive Capillary Stamping of Aqueous Precursor Solutions, *Advanced Engineering Materials* **2022**, *24*, 2101159.
- [10] F. Alarслан, M. Frosinn, K. Ruwisch, J. Thien, T. Jähnichen, L. Eckert, J. Klein, M. Haase, D. Enke, J. Wollschläger, U. Beginn, M. Steinhart, Reactive Additive Capillary Stamping with Double Network Hydrogel-Derived Aerogel Stamps under

- Solvothermal Conditions, *ACS Applied Materials & Interfaces* **2022**, *14*, 44992.
- [11] Y. F. Kong, F. Bo, W. W. Wang, D. H. Zheng, H. D. Liu, G. Q. Zhang, R. Rupp, J. J. Xu, Recent Progress in Lithium Niobate: Optical Damage, Defect Simulation, and On-Chip Devices, *Advanced Materials* **2020**, *32*, 1806452.
- [12] R. S. Weis, T. K. Gaylord, Lithium Niobate: Summary of Physical Properties and Crystal Structure, *Applied Physics A - Materials Science & Processing* **1985**, *37*, 191.
- [13] A. Honardoost, K. Abdelsalam, S. Fathpour, Rejuvenating a Versatile Photonic Material: Thin-Film Lithium Niobate, *Laser & Photonics Reviews* **2020**, *14*, 2000088.
- [14] D. H. Sun, Y. W. Zhang, D. Z. Wang, W. Song, X. Y. Liu, J. B. Pang, D. Q. Geng, Y. H. Sang, H. Liu, Microstructure and domain engineering of lithium niobate crystal films for integrated photonic applications, *Light-Science & Applications* **2020**, *9*, 197.
- [15] Y. L. Zheng, X. F. Chen, Nonlinear wave mixing in lithium niobate thin film, *Advances in Physics-X* **2021**, *6*, 1889402.
- [16] G. Poberaj, H. Hu, W. Sohler, P. Günter, Lithium niobate on insulator (LNOI) for micro-photonic devices, *Laser & Photonics Reviews* **2012**, *6*, 488.
- [17] Y. C. Jia, L. Wang, F. Chen, Ion-cut lithium niobate on insulator technology: Recent advances and perspectives, *Applied Physics Reviews* **2021**, *8*, 11307.
- [18] V. Amendola, R. Pilot, M. Frascioni, O. M. Maragò, M. A. Iatì, Surface plasmon resonance in gold nanoparticles: a review, *Journal of Physics-Condensed Matter* **2017**, *29*, 203002.
- [19] F. Dutto, M. Heiss, A. Lovera, O. Lopez-Sanchez, A. F. I. Morral, A. Radenovic, Enhancement of Second Harmonic Signal in Nanofabricated Cones, *Nano Letters* **2013**, *13*, 6048.
- [20] E. Yraola, P. Molina, J. L. Plaza, M. O. Ramirez, L. E. Bausa, Spontaneous Emission and Nonlinear Response Enhancement by Silver Nanoparticles in a Nd³⁺-Doped Periodically Poled LiNbO₃ Laser Crystal, *Advanced Materials* **2013**,

- 25, 910.
- [21] D. Lehr, J. Reinhold, I. Thiele, H. Hartung, K. Dietrich, C. Menzel, T. Pertsch, E. B. Kley, A. Tünnermann, Enhancing Second Harmonic Generation in Gold Nanoring Resonators Filled with Lithium Niobate, *Nano Letters* **2015**, *15*, 1025.
- [22] M. O. Ramirez, P. Molina, A. Gomez-Tornero, D. Hernandez-Pinilla, L. Sanchez-Garcia, S. Carretero-Palacios, L. E. Bausa, Hybrid Plasmonic-Ferroelectric Architectures for Lasing and SHG Processes at the Nanoscale, *Advanced Materials* **2019**, *31*, 23.
- [23] F. Ge, X. Han, J. L. Xu, Strongly Coupled Systems for Nonlinear Optics, *Laser & Photonics Reviews* **2021**, *15*, 2000514.
- [24] E. Gurdal, A. Horneber, N. Shaqura, A. J. Meixner, D. P. Kern, D. Zhang, M. Fleischer, Enhancement of the second harmonic signal of nonlinear crystals by self-assembled gold nanoparticles, *Journal of Chemical Physics* **2020**, *152*, 104711.
- [25] S. Hirano, K. Kato, Formation of LiNbO₃ Films by Hydrolysis of Metal Alkoxides, *Journal of Non-Crystalline Solids* **1988**, *100*, 538.
- [26] T. Yogo, Y. Takeichi, K. Kikuta, S. Hirano, Ultraviolet Patterning of Alkoxy-Derived Lithium Niobate Film, *Journal of the American Ceramic Society* **1995**, *78*, 1649.
- [27] S. Ono, S. Hirano, Patterning of lithium niobate thin films derived from aqueous solution, *Journal of the American Ceramic Society* **1997**, *80*, 2533.
- [28] S. Hirano, T. Yogo, W. Sakamoto, Y. Takeichi, S. Ono, Processing of highly oriented LiNbO₃ thin films through a metal-organic precursor solution, *Journal of the European Ceramic Society* **2004**, *24*, 435.
- [29] S. Ono, S. I. Hirano, Processing of lithium niobate and potassium lithium niobate films using environmentally-friendly aqueous precursor solutions, *Journal of the Ceramic Society of Japan* **2007**, *115*, 801.
- [30] M. Wu, W. B. Yan, J. L. Jing, D. H. Wang, L. H. Shi, L. X. Zhang, X. Wang, S. B. Li, H. J. Chen, Patterned LiNbO₃ thin film fabrication basing aqueous precursor and the study on pattern quality and film morphology, *Journal of Alloys and*

- Compounds* **2016**, 670, 144.
- [31] A. Rabenau, The Role of Hydrothermal Synthesis in Preparative Chemistry, *Angewandte Chemie-International Edition* **1985**, 24, 1026.
- [32] G. Demazeau, Solvothermal reactions: an original route for the synthesis of novel materials, *Journal of Materials Science* **2008**, 43, 2104.
- [33] F. F. Lange, Chemical Solution Routes to Single-Crystal Thin Films, *Science* **1996**, 273, 903.
- [34] D. Andeen, J. H. Kim, F. F. Lange, G. K. L. Goh, S. Tripathy, Lateral epitaxial overgrowth of ZnO in water at 90 degrees C, *Advanced Functional Materials* **2006**, 16, 799.
- [35] S. Yanez-Vilar, M. Sanchez-Andujar, C. Gomez-Aguirre, J. Mira, M. A. Senaris-Rodriguez, S. Castro-Garcia, A simple solvothermal synthesis of MFe₂O₄ (M = Mn, Co and Ni) nanoparticles, *Journal of Solid State Chemistry* **2009**, 182, 2685.
- [36] J. Z. Huo, M. Z. Wei, Characterization and magnetic properties of nanocrystalline nickel ferrite synthesized by hydrothermal method, *Materials Letters* **2009**, 63, 1183.
- [37] Z. X. Wang, M. Elimelech, S. H. Lin, Environmental Applications of Interfacial Materials with Special Wettability, *Environmental Science & Technology* **2016**, 50, 2132.
- [38] Z. K. He, X. R. Lan, Q. S. Hu, H. M. Li, L. M. Li, J. Y. Mao, Antifouling strategies based on super-phobic polymer materials, *Progress in Organic Coatings* **2021**, 157, 106285.
- [39] J. J. Chi, X. X. Zhang, Y. T. Wang, C. M. Shao, L. R. Shang, Y. J. Zhao, Bio-inspired wettability patterns for biomedical applications, *Materials Horizons* **2021**, 8, 124.
- [40] N. Abu Jarad, H. Imran, S. M. Imani, T. F. Didar, L. Soleymani, Fabrication of Superamphiphobic Surfaces via Spray Coating; a Review, *Advanced Materials Technologies* **2022**, 7, 2101702.
- [41] M. Load, B. Ghule, Fabrication Techniques of Superhydrophobic Coatings: A

- Comprehensive Review, *Physica Status Solidi a-Applications and Materials Science* **2022**, *219*, 2200109.
- [42] B. W. Xin, J. C. Hao, Reversibly switchable wettability, *Chemical Society Reviews* **2010**, *39*, 769.
- [43] D. J. Zhang, Z. J. Cheng, Y. Y. Liu, Smart Wetting Control on Shape Memory Polymer Surfaces, *Chemistry-a European Journal* **2019**, *25*, 3979.
- [44] C. Li, M. Li, Z. S. Ni, Q. W. Guan, B. R. K. Blackman, E. Saiz, Stimuli-responsive surfaces for switchable wettability and adhesion, *Journal of The Royal Society Interface* **2021**, *18*, 20210162.
- [45] J. Elbert, M. Gallei, C. Rüttiger, A. Brunsen, H. Didzoleit, B. Stühn, M. Rehahn, Ferrocene Polymers for Switchable Surface Wettability, *Organometallics* **2013**, *32*, 5873.
- [46] H. Hübner, R. Candeago, D. Schmitt, A. Schiesser, B. C. Xiong, M. Gallei, X. Su, Synthesis and covalent immobilization of redox-active metallopolymers for organic phase electrochemistry, *Polymer* **2022**, *244*, 124656.
- [47] J. Willmann, D. Stocker, E. Dörsam, Characteristics and evaluation criteria of substrate-based manufacturing. Is roll-to-roll the best solution for printed electronics?, *Organic Electronics* **2014**, *15*, 1631.
- [48] P. Rai-Choudhury, Handbook of microlithography, micromachining, and microfabrication, *SPIE Optical Engineering Press* **1997**.
- [49] S. Hong, C. A. Mirkin, A nanoplotter with both parallel and serial writing capabilities, *Science* **2000**, *288*, 1808.
- [50] F. Huo, Z. Zheng, G. Zheng, L. R. Giam, H. Zhang, C. A. Mirkin, Polymer pen lithography, *Science* **2008**, *321*, 1658.
- [51] G. M. Whitesides, E. Ostuni, S. Takayama, X. Jiang, D. E. Ingber, Soft lithography in biology and biochemistry, *Annual Review of Biomedical Engineering* **2001**, *3*, 335.
- [52] A. P. Quist, E. Pavlovic, S. Oscarsson, Recent advances in microcontact printing, *Analytical and Bioanalytical Chemistry* **2005**, *381*, 591.

-
- [53] Y. Xia, G. M. Whitesides, Extending Microcontact Printing as a Microlithographic Technique, *Langmuir* **1997**, *13*, 2059.
- [54] E. Kim, Y. Xia, G. M. Whitesides, Polymer microstructures formed by moulding in capillaries, *Nature* **1995**, *376*, 581.
- [55] Y. Xia, E. Kim, G. M. Whitesides, Micromolding of Polymers in Capillaries: Applications in Microfabrication, *Chemistry of Materials* **1996**, *8*, 1558.
- [56] X.-M. Zhao, Y. Xia, G. M. Whitesides, Soft lithographic methods for nanofabrication, *Journal of Materials Chemistry* **1997**, *7*, 1069.
- [57] E. King, Y. Xia, X.-M. Zhao, G. M. Whitesides, Solvent-assisted microcontact molding: A convenient method for fabricating three-dimensional structures on surfaces of polymers, *Advanced Materials* **1997**, *9*, 651.
- [58] S. A. Nikitov, L. Presmanes, Ph. Tailhades, D. E. Balabanov, Magnetic duplication and contact printing method, *Journal of Magnetism and Magnetic Materials* **2002**, *241*, 124.
- [59] S. Hoepfner, R. Maoz, J. Sagiv, Constructive Microlithography: Electrochemical Printing of Monolayer Template Patterns Extends Constructive Nanolithography to the Micrometer–Millimeter Dimension Range, *Nano Letters* **2003**, *3*, 761.
- [60] B. Kang, W. H. Lee, K. Cho, Recent advances in organic transistor printing processes, *ACS Applied Materials & Interfaces* **2013**, *5*, 2302.
- [61] G. Cummins, M. P. Desmulliez, Inkjet printing of conductive materials: a review, *Circuit World* **2012**, *38*, 193.
- [62] M. J. Uddin, J. Hassan, D. Douroumis, Thermal Inkjet Printing: Prospects and Applications in the Development of Medicine, *Technologies* **2022**, *10*, 108.
- [63] G.-K. Lau, M. Shrestha, Ink-Jet Printing of Micro-Electro-Mechanical Systems (MEMS), *Micromachines* **2017**, *8*, 194.
- [64] J. Li, F. Rossignol, J. Macdonald, Inkjet printing for biosensor fabrication: combining chemistry and technology for advanced manufacturing, *Lab on a Chip* **2015**, *15*, 2538.
- [65] V. Beedasy, P. J. Smith, Printed Electronics as Prepared by Inkjet Printing,

Materials **2020**, *13*.

- [66] G. A. Torres Sevilla, M. M. Hussain, Printed Organic and Inorganic Electronics: Devices To Systems, *IEEE Journal on Emerging and Selected Topics in Circuits and Systems* **2017**, *7*, 147.
- [67] N. J. Wilkinson, M. A. A. Smith, R. W. Kay, R. A. Harris, A review of aerosol jet printing—a non-traditional hybrid process for micro-manufacturing, *The International Journal of Advanced Manufacturing Technology* **2019**, *105*, 4599.
- [68] E. B. Secor, Principles of aerosol jet printing, *Flexible and Printed Electronics* **2018**, *3*, 35002.
- [69] H. Sirringhaus, T. Shimoda, Inkjet Printing of Functional Materials, *MRS Bulletin* **2003**, *28*, 802.
- [70] P. Serra, A. Pique, Laser-Induced Forward Transfer: Fundamentals and Applications, *Advanced Materials Technologies* **2019**, *4*, 1800099.
- [71] P. Delaporte, A.-P. Alloncle, [INVITED] Laser-induced forward transfer: A high resolution additive manufacturing technology, *Optics & Laser Technology* **2016**, *78*, 33.
- [72] H. Xu, X. Y. Ling, J. van Bennekom, X. Duan, M. J. W. Ludden, D. N. Reinhoudt, M. Wessling, R. G. H. Lammertink, J. Huskens, Microcontact printing of dendrimers, proteins, and nanoparticles by porous stamps, *Journal of the American Chemical Society* **2009**, *131*, 797.
- [73] D.-M. Wang, J.-Y. Lai, Recent advances in preparation and morphology control of polymeric membranes formed by nonsolvent induced phase separation, *Current Opinion in Chemical Engineering* **2013**, *2*, 229.
- [74] M. Schmidt, M. Philippi, M. Münzner, J. M. Stangl, R. Wieczorek, W. Harneit, K. Müller-Buschbaum, D. Enke, M. Steinhart, Capillary Nanostamping with Spongy Mesoporous Silica Stamps, *Advanced Functional Materials* **2018**, *28*, 1800700.
- [75] P. Hou, W. Han, M. Philippi, H. Schäfer, M. Steinhart, Nanostructured Submicron Block Copolymer Dots by Sacrificial Stamping: A Potential Preconcentration Platform for Locally Resolved Sensing, Chemistry, and Cellular Interactions, *ACS*

- Applied Nano Materials* **2018**, *1*, 1413.
- [76] W. Han, P. Hou, S. Sadaf, H. Schäfer, L. Walder, M. Steinhart, Ordered Topographically Patterned Silicon by Insect-Inspired Capillary Submicron Stamping, *ACS Applied Materials & Interfaces* **2018**, *10*, 7451.
- [77] L. Guo, M. Philippi, M. Steinhart, Substrate Patterning Using Regular Macroporous Block Copolymer Monoliths as Sacrificial Templates and as Capillary Microstamps, *Small* **2018**, *14*, 1801452.
- [78] Y. Wang, U. Gösele, M. Steinhart, Mesoporous block copolymer nanorods by swelling-induced morphology reconstruction, *Nano Letters* **2008**, *8*, 3548.
- [79] Y. Wang, Y. Qin, A. Berger, E. Yau, C. He, L. Zhang, U. Gösele, M. Knez, M. Steinhart, Nanoscopic Morphologies in Block Copolymer Nanorods as Templates for Atomic-Layer Deposition of Semiconductors, *Advanced Materials* **2009**, *21*, 2763.
- [80] Y. Wang, L. Tong, M. Steinhart, Swelling-induced morphology reconstruction in block copolymer nanorods: kinetics and impact of surface tension during solvent evaporation, *ACS Nano* **2011**, *5*, 1928.
- [81] Y. Wang, C. He, W. Xing, F. Li, L. Tong, Z. Chen, X. Liao, M. Steinhart, Nanoporous metal membranes with bicontinuous morphology from recyclable block-copolymer templates, *Advanced Materials* **2010**, *22*, 2068.
- [82] L. Xue, A. Kovalev, K. Dening, A. Eichler-Volf, H. Eickmeier, M. Haase, D. Enke, M. Steinhart, S. N. Gorb, Reversible adhesion switching of porous fibrillar adhesive pads by humidity, *Nano Letters* **2013**, *13*, 5541.
- [83] H. Xu, X. Y. Ling, J. van Bennekom, X. Duan, M. J. W. Ludden, D. N. Reinhoudt, M. Wessling, R. G. H. Lammertink, J. Huskens, Microcontact Printing of Dendrimers, Proteins, and Nanoparticles by Porous Stamps, *Journal of the American Chemical Society* **2009**, *131*, 797.
- [84] M. Schmidt, M. Philippi, M. Münzner, J. M. Stangl, R. Wiczorek, W. Harneit, K. Müller-Buschbaum, D. Enke, M. Steinhart, Capillary nanostamping with spongy mesoporous silica stamps, *Advanced Functional Materials* **2018**, *28*, 1800700.

-
- [85] P. Hou, R. Kumar, B. Oberleiter, R. Kohns, D. Enke, U. Beginn, H. Fuchs, M. Hirtz, M. Steinhart, Scanner-based capillary stamping, *Advanced Functional Materials* **2020**, *30*, 2001531.
- [86] M. Runge, H. Hübner, A. Grimm, G. Manoharan, R. Wiczorek, M. Philippi, W. Harneit, C. Meyer, D. Enke, M. Gallei, M. Steinhart, Capillary Stamping of Functional Materials: Parallel Additive Substrate Patterning without Ink Depletion, *Advanced Materials Interfaces* **2021**, *8*, 2001911.
- [87] L. M. Guo, J. Klein, J. Thien, M. Philippi, M. Haase, J. Wollschlager, M. Steinhart, Phenolic Resin Dual-Use Stamps for Capillary Stamping and Decal Transfer Printing, *ACS Applied Materials & Interfaces* **2021**, *13*, 49567.
- [88] J. T. C. Yeh, Laser ablation of polymers, *Journal of Vacuum Science & Technology A: Vacuum, Surfaces, and Films* **1986**, *4*, 653.
- [89] S. Alom Ruiz, C. S. Chen, Microcontact printing: A tool to pattern, *Soft Matter* **2007**, *3*, 168.
- [90] J. Zhou, D. A. Khodakov, A. V. Ellis, N. H. Voelcker, Surface modification for PDMS-based microfluidic devices, *ELECTROPHORESIS* **2012**, *33*, 89.
- [91] L. M. Cox, A. M. Martinez, A. K. Blevins, N. Sowan, Y. Ding, C. N. Bowman, Nanoimprint lithography: Emergent materials and methods of actuation, *Nano Today* **2020**, *31*, 100838.
- [92] D. Qin, Y. Xia, G. M. Whitesides, Soft lithography for micro- and nanoscale patterning, *Nature Protocols* **2010**, *5*, 491.
- [93] H. Xu, J. Huskens, Versatile stamps in microcontact printing: transferring inks by molecular recognition and from ink reservoirs, *Chemistry* **2010**, *16*, 2342.
- [94] J. P. Gong, Y. Katsuyama, T. Kurokawa, Y. Osada, Double-network hydrogels with extremely high mechanical strength, *Advanced Materials* **2003**, *15*, 1155.
- [95] M. A. Haque, T. Kurokawa, J. P. Gong, Super tough double network hydrogels and their application as biomaterials, *Polymer* **2012**, *53*, 1805.
- [96] J. P. Gong, Why are double network hydrogels so tough?, *Soft Matter* **2010**, *6*, 2583.

-
- [97] H. Tsukeshiba, M. Huang, Y.-H. Na, T. Kurokawa, R. Kuwabara, Y. Tanaka, H. Furukawa, Y. Osada, J. P. Gong, Effect of polymer entanglement on the toughening of double network hydrogels, *The Journal of Physical Chemistry B* **2005**, *109*, 16304.
- [98] Y.-H. Na, T. Kurokawa, Y. Katsuyama, H. Tsukeshiba, J. P. Gong, Y. Osada, S. Okabe, T. Karino, M. Shibayama, Structural Characteristics of Double Network Gels with Extremely High Mechanical Strength, *Macromolecules* **2004**, *37*, 5370.
- [99] T. Nakajima, H. Furukawa, Y. Tanaka, T. Kurokawa, Y. Osada, J. P. Gong, True Chemical Structure of Double Network Hydrogels, *Macromolecules* **2009**, *42*, 2184.
- [100] J. N. Broughton, M. J. Brett, Variations in MnO₂ electrodeposition for electrochemical capacitors, *Electrochimica Acta* **2005**, *50*, 4814.
- [101] R. S. Weis, T. K. Gaylord, Lithium niobate: Summary of physical properties and crystal structure, *Applied Physics A Solids and Surfaces* **1985**, *37*, 191.
- [102] T. Jungk, Untersuchung der Abbildungsmechanismen ferroelektrischer Domänen mit dem Rasterkraftmikroskop, *Shaker* **2007**.
- [103] S. C. Abrahams, P. Marsh, Defect structure dependence on composition in lithium niobate, *Acta Crystallographica Section B Structural Science* **1986**, *42*, 61.
- [104] R. W. Boyd, Nonlinear optics, *Elsevier* **2008**.
- [105] D. A. Kleinman, Theory of Second Harmonic Generation of Light, *Physical Review* **1962**, *128*, 1761.
- [106] R. W. Boyd, Nonlinear optics, *Elsevier/Academic Press* **2008**.
- [107] M. Perner, Optische Untersuchung der Elektronen- und Gitterdynamik in Edelmetall-Nanopartikeln, *Shaker* **1999**.
- [108] U. Kreibig, M. Vollmer, Optical Properties of Metal Clusters, *Springer Science & Business Media* **2013**.
- [109] S. Link, M. A. El-Sayed, Shape and size dependence of radiative, non-radiative and photothermal properties of gold nanocrystals, *International Reviews in Physical Chemistry* **2000**, *19*, 409.

-
- [110] A. Trügler, *Optical Properties of Metallic Nanoparticles: Basic Principles and Simulation*, Springer **2016**.
- [111] K. L. Kelly, E. Coronado, L. L. Zhao, G. C. Schatz, The Optical Properties of Metal Nanoparticles: The Influence of Size, Shape, and Dielectric Environment, *The Journal of Physical Chemistry B* **2003**, *107*, 668.
- [112] R. Schlipper, R. Kusche, B. von Issendorff, H. Haberland, Multiple Excitation and Lifetime of the Sodium Cluster Plasmon Resonance, *Physical Review Letters* **1998**, *80*, 1194.
- [113] K. Hagino, Anharmonicity of the dipole resonance of metal clusters, *Physical Review B* **1999**, *60*, R2197-R2199.
- [114] C Sönnichsen, T Franzl, T Wilk, G von Plessen, J Feldmann, Plasmon resonances in large noble-metal clusters, *New Journal of Physics* **2002**, *4*, 93.
- [115] L. Bonacina, Nonlinear nanomedicine: harmonic nanoparticles toward targeted diagnosis and therapy, *Molecular Pharmaceutics* **2013**, *10*, 783.
- [116] E. Kim, A. Steinbrück, M. T. Buscaglia, V. Buscaglia, T. Pertsch, R. Grange, Second-harmonic generation of single BaTiO₃ nanoparticles down to 22 nm diameter, *ACS Nano* **2013**, *7*, 5343.
- [117] M. Kauranen, A. V. Zayats, Nonlinear plasmonics, *Nature Photon* **2012**, *6*, 737.
- [118] V. Amendola, R. Pilot, M. Frasconi, O. M. Maragò, M. A. Iatì, Surface plasmon resonance in gold nanoparticles: a review, *Journal of Physics: Condensed Matter* **2017**, *29*, 203002.
- [119] D. Lehr, J. Reinhold, I. Thiele, H. Hartung, K. Dietrich, C. Menzel, T. Pertsch, E.-B. Kley, A. Tünnermann, Enhancing second harmonic generation in gold nanoring resonators filled with lithium niobate, *Nano Letters* **2015**, *15*, 1025.
- [120] N. C. Panoiu, W. E. I. Sha, D. Y. Lei, G.-C. Li, Nonlinear optics in plasmonic nanostructures, *Journal of Optics* **2018**, *20*, 83001.
- [121] J. Butet, K.-Y. Yang, S. Dutta-Gupta, O. J. F. Martin, Maximizing Nonlinear Optical Conversion in Plasmonic Nanoparticles through Ideal Absorption of Light, *ACS Photonics* **2016**, *3*, 1453.

- [122] Y. Pu, R. Grange, C.-L. Hsieh, D. Psaltis, Nonlinear optical properties of core-shell nanocavities for enhanced second-harmonic generation, *Physical Review Letters* **2010**, *104*, 207402.
- [123] S. A. Maier, Plasmonics: Fundamentals and Applications, *Springer Science & Business Media* **2007**.
- [124] M. I. Stockman, Nanoplasmonics: The physics behind the applications, *Physics Today* **2011**, *64*, 39.
- [125] Y.-B. Park, B. Min, K. J. Vahala, H. A. Atwater, Integration of Single-Crystal LiNbO₃ Thin Film on Silicon by Laser Irradiation and Ion Implantation– Induced Layer Transfer, *Advanced Materials* **2006**, *18*, 1533.
- [126] Y. Xia, G. M. Whitesides, Soft Lithography, *Annual Review of Materials Science* **1998**, *28*, 153.
- [127] D. Li, Y. Sun, P. Gao, X. Zhang, H. Ge, Structural and magnetic properties of nickel ferrite nanoparticles synthesized via a template-assisted sol–gel method, *Ceramics International* **2014**, *40*, 16529.
- [128] G. Dixit, J. P. Singh, R. C. Srivastava, H. M. Agrawal, R. J. Choudhary, A. Gupta, Annealing effect on the structural and magnetic properties of nickel ferrite thin films, *Surface and Interface Analysis* **2010**, *42*, 151.
- [129] B. Issa, I. M. Obaidat, B. A. Albiss, Y. Haik, Magnetic nanoparticles: surface effects and properties related to biomedicine applications, *International Journal of Molecular Sciences* **2013**, *14*, 21266.
- [130] W. Demtröder, Experimentalphysik 2: Elektrizität und Optik, *Springer* **1999**.
- [131] G. Fasching, Werkstoffe für die Elektrotechnik: Mikrophysik, Struktur, Eigenschaften, *Springer* **2005**.
- [132] S. Hunklinger, Festkörperphysik, *Oldenbourg* **2014**.
- [133] R. J. Brook, W. D. Kingery, Nickel Ferrite Thin Films: Microstructures and Magnetic Properties, *Journal of Applied Physics* **1967**, *38*, 3589.
- [134] K. N. Koo, A. F. Ismail, M. H. D. Othman, N. Bidin, M. A Rahman, Preparation and characterization of superparamagnetic magnetite (Fe₃O₄) nanoparticles: A short

- review, *Malaysian Journal of Fundamental and Applied Sciences* **2019**, *15*, 23.
- [135] H. Fischer, H. Hofmann, J. Spindler, Werkstoffe in der Elektrotechnik: Grundlagen, Aufbau, Eigenschaften, Prüfung, Anwendung, Technologie ; mit 110 Tabellen, sowie zahlreichen Beispielen, Übungen und Testaufgaben, *Hanser* **2000**.
- [136] K. J. Klabunde, Nanoscale Materials in Chemistry, *Wiley-Interscience* **2001**.
- [137] S. Anjum, G. H. Jaffari, A. K. Rumaiz, M. S. Rafique, S. I. Shah, Role of vacancies in transport and magnetic properties of nickel ferrite thin films, *Journal of Physics D: Applied Physics* **2010**, *43*, 265001.
- [138] R. Sen, P. Jain, R. Patidar, S. Srivastava, R. S. Rana, N. Gupta, Synthesis and Characterization of Nickel Ferrite (NiFe₂O₄) Nanoparticles Prepared by Sol- Gel Method, *Materials Today: Proceedings* **2015**, *2*, 3750.
- [139] A. R. Chavan, S. D. Birajdar, R. R. Chilwar, K. M. Jadhav, Structural, morphological, optical, magnetic and electrical properties of Al³⁺ substituted nickel ferrite thin films, *Journal of Alloys and Compounds* **2018**, *735*, 2287.
- [140] K. Mondal, M. D. McMurtrey, Present status of the functional advanced micro-, nano-printings - a mini review, *Materials Today Chemistry* **2020**, *17*, 100328.
- [141] C. Carbonell, D. J. Valles, A. M. Wong, M. W. Tsui, M. Niang, A. B. Braunschweig, Massively Multiplexed Tip-Based Photochemical Lithography under Continuous Capillary Flow, *Chem* **2018**, *4*, 857.
- [142] C. Carbonell, A. B. Braunschweig, Toward 4D Nanoprinting with Tip-Induced Organic Surface Reactions, *Accounts of Chemical Research* **2017**, *50*, 190.
- [143] M. Mazurowski, M. Gallei, J. Li, H. Didzoleit, B. Stühn, M. Rehahn, Redox-Responsive Polymer Brushes Grafted from Polystyrene Nanoparticles by Means of Surface Initiated Atom Transfer Radical Polymerization, *Macromolecules* **2012**, *45*, 8970.
- [144] B. Y. Kim, E. L. Ratcliff, N. R. Armstrong, T. Kowalewski, J. Pyun, Ferrocene functional polymer brushes on indium tin oxide via surface-initiated atom transfer radical polymerization, *Langmuir the ACS Journal of Surfaces and Colloids* **2010**, *26*, 2083.

- [145] J. Elbert, F. Krohm, C. Rüttiger, S. Kienle, H. Didzoleit, B. N. Balzer, T. Hugel, B. Stühn, M. Gallei, A. Brunsen, Polymer-Modified Mesoporous Silica Thin Films for Redox-Mediated Selective Membrane Gating, *Advanced Functional Materials* **2014**, *24*, 1591.
- [146] M. A. C. Stuart, W. T. S. Huck, J. Genzer, M. Müller, C. Ober, M. Stamm, G. B. Sukhorukov, I. Szleifer, V. V. Tsukruk, M. Urban, F. Winnik, S. Zauscher, I. Luzinov, S. Minko, Emerging applications of stimuli-responsive polymer materials, *Nature Materials* **2010**, *9*, 101.
- [147] G. Q. Liu, S. H. Petrosko, Z. J. Zheng, C. A. Mirkin, Evolution of Dip-Pen Nanolithography (DPN): From Molecular Patterning to Materials Discovery, *Chemical Reviews* **2020**, *120*, 6009.
- [148] P. van de Witte, P. J. Dijkstra, J. W. A. van den Berg, J. Feijen, Phase separation processes in polymer solutions in relation to membrane formation, *Journal of Membrane Science* **1996**, *117*, 1.
- [149] T. M. Robinson, D. W. Hutmacher, P. D. Dalton, The Next Frontier in Melt Electrospinning: Taming the Jet, *Advanced Functional Materials* **2019**, *29*, 1904664.
- [150] G. Kumar, K. N. Prabhu, Review of non-reactive and reactive wetting of liquids on surfaces, *Advances in Colloid and Interface Science* **2007**, *133*, 61.
- [151] J. Bico, C. Tordeux, D. Quéré, Rough wetting, *Europhysics Letters* **2001**, *55*, 214.
- [152] Y. Wu, J. Du, G. Liu, D. Ma, F. Jia, J. J. Klemesš, J. Wang, A review of self-cleaning technology to reduce dust and ice accumulation in photovoltaic power generation using superhydrophobic coating, *Renewable Energy* **2022**, *185*, 1034.
- [153] D. Y. Kwok, A. W. Neumann, Contact angle measurement and contact angle interpretation, *Advances in colloid and interface science* **1999**, *81*, 167.
- [154] III. An essay on the cohesion of fluids, *Philosophical Transactions of the Royal Society*. **1805**, *95*, 65.
- [155] D. Bonn, J. Eggers, J. Indekeu, J. Meunier, E. Rolley, Wetting and spreading, *Reviews of Modern Physics* **2009**, *81*, 739.

-
- [156] A. Marmur, C. Della Volpe, S. Siboni, A. Amirfazli, J. W. Drelich, Contact angles and wettability: towards common and accurate terminology, *Surface Innovations* **2017**, 5, 3.
- [157] A. Marmur, The Contact Angle Hysteresis Puzzle, *Colloids and Interfaces* **2022**, 6, 39.
- [158] A. Nakajima, K. Hashimoto, T. Watanabe. Recent Studies on Super-Hydrophobic Films, Molecular materials and functional polymers (Eds.: W. J. Blau, P. Lianos, U. Schubert), *Springer* **2001**, p. 31.
- [159] R. N. Wenzel, RESISTANCE OF SOLID SURFACES TO WETTING BY WATER, *Industrial & Engineering Chemistry* **1936**, 28, 988.
- [160] M. Morra, E. Occhiello, F. Garbassi, Knowledge about polymer surfaces from contact angle measurements, *Advances in Colloid and Interface Science* **1990**, 32, 79.
- [161] H. Nakae, R. Inui, Y. Hirata, H. Saito, Effects of surface roughness on wettability, *Acta Materialia* **1998**, 46, 2313.
- [162] A. B. D. Cassie, S. Baxter, Wettability of porous surfaces, *Transactions of the Faraday Society* **1944**, 40, 546.
- [163] Sakai, Fujii, The Dependence of the Apparent Contact Angles on Gravity, *Journal of Colloid and Interface Science* **1999**, 210, 152.
- [164] B. He, J. Lee, N. A. Patankar, Contact angle hysteresis on rough hydrophobic surfaces, *Colloids and Surfaces A: Physicochemical and Engineering Aspects* **2004**, 248, 101.
- [165] C. W. Extrand, Criteria for ultralyophobic surfaces, *Langmuir* **2004**, 20, 5013.
- [166] H. Y. Erbil, The debate on the dependence of apparent contact angles on drop contact area or three-phase contact line: A review, *Surface Science Reports* **2014**, 69, 325.
- [167] M. N. MacGregor - Ramiasa, K. Vasilev, Questions and Answers on the Wettability of Nano - Engineered Surfaces, *Advanced Materials Interfaces* **2017**, 4, 1700381.
- [168] D. Öner, T. J. McCarthy, Ultrahydrophobic Surfaces. Effects of Topography Length

- Scales on Wettability, *Langmuir* **2000**, *16*, 7777.
- [169] L. Gao, T. J. McCarthy, How Wenzel and Cassie were wrong, *Langmuir* **2007**, *23*, 3762.
- [170] R. G. Picknett, R. Bexon, The Evaporation of Sessile or Pendant Drops in Still Air, *Journal of Colloid and Interface Science* **1977**, *61*, 336.
- [171] Y. V. Kalinin, V. Berejnov, R. E. Thorne, Contact Line Pinning by Microfabricated Patterns: Effects of Microscale Topography, *Langmuir* **2009**, *25*, 5391.
- [172] P. S. H. Forsberg, C. Priest, M. Brinkmann, R. Sedev, J. Ralston, Contact Line Pinning on Microstructured Surfaces for Liquids in the Wenzel State, *Langmuir* **2010**, *26*, 860.
- [173] K. Gleason, S. A. Putnam, Microdroplet Evaporation with a Forced Pinned Contact Line, *Langmuir* **2014**, *30*, 10548.
- [174] S. Kumar, V. Charitatos, Influence of Surface Roughness on Droplet Evaporation and Absorption: Insights into Experiments from Lubrication-Theory- Based Models, *Langmuir* **2022**, *38*, 15889.
- [175] H. G. Ozcelik, E. Satiroglu, M. Barisik, Size dependent influence of contact line pinning on wetting of nano-textured/patterned silica surfaces, *Nanoscale* **2020**, *12*, 21376.
- [176] J. G. Zhang, F. Müller-Plathe, F. Leroy, Pinning of the Contact Line during Evaporation on Heterogeneous Surfaces: Slowdown or Temporary Immobilization? Insights from a Nanoscale Study, *Langmuir* **2015**, *31*, 7544.
- [177] N. Verplanck, Y. Coffinier, V. Thomy, R. Boukherroub, Wettability Switching Techniques on Superhydrophobic Surfaces, *Nanoscale Research Letters* **2007**, *2*, 577.
- [178] Y. Jiang, P. Wan, M. Smet, Z. Wang, X. Zhang, Self-Assembled Monolayers of a Malachite Green Derivative: Surfaces with pH- and UV-Responsive Wetting Properties, *Advanced Materials* **2008**, *20*, 1972.
- [179] S. Wang, Y. SONG, L. JIANG, Photoresponsive surfaces with controllable wettability, *Journal of Photochemistry and Photobiology C: Photochemistry*

Reviews **2007**, *8*, 18.

- [180] B. S. Lee, Y. S. Chi, J. K. Lee, I. S. Choi, C. E. Song, S. K. Namgoong, S. Lee, Imidazolium ion-terminated self-assembled monolayers on Au: effects of counteranions on surface wettability, *Journal of the American Chemical Society* **2004**, *126*, 480.
- [181] A. Y. Fadeev, T. J. McCarthy, Self-Assembly Is Not the Only Reaction Possible between Alkyltrichlorosilanes and Surfaces: Monomolecular and Oligomeric Covalently Attached Layers of Dichloro- and Trichloroalkylsilanes on Silicon, *Langmuir* **2000**, *16*, 7268.
- [182] N. Sakai, Y. Fujiwara, M. Arai, K. Yu, T. Tatsuma, Electrodeposition of gold nanoparticles on ITO: Control of morphology and plasmon resonance-based absorption and scattering, *Journal of Electroanalytical Chemistry* **2009**, *628*, 7.
- [183] L. Vittadello, C. Kijatkin, D. Dzikowski, J. Klenen, K. Kömpe, C. Meyer, A. Paululat, M. Imlau, In-vivo tracking of harmonic nanoparticles: a study based on a TIGER widefield microscope, *Optical Materials Express* **2021**, *11*, 1953.
- [184] K. L. Purvis, G. Lu, J. Schwartz, S. L. Bernasek, Surface characterization and modification of indium tin oxide in ultrahigh vacuum, *Journal of the American Chemical Society* **2000**, *122*, 1808.
- [185] A. Birner, U. Grüning, S. Ottow, A. Schneider, F. Müller, V. Lehmann, H. Föll, U. Gösele, Macroporous silicon: A two-dimensional photonic bandgap material suitable for the near-infrared spectral range, *Physica Status Solidi a-Applied Research* **1998**, *165*, 111.
- [186] A. Birner, R. B. Wehrspohn, U. M. Gösele, K. Busch, Silicon-based photonic crystals, *Advanced Materials* **2001**, *13*, 377.
- [187] F. L. Faita, C. E. M. Campos, K. Ersching, P. S. Pizani, Structural, thermal and vibrational characterization of mechanical alloyed In₅₀Te₅₀, *Materials Chemistry and Physics* **2011**, *125*, 257.
- [188] S. C. Abrahams, J. M. Reddy, J. L. Bernstein, Ferroelectric lithium niobate. 3. Single crystal X-ray diffraction study at 24°C, *Journal of Physics and Chemistry of*

Solids **1966**, 27, 997.

- [189] V. Bornand, P. Papet, Reliability and effectiveness of LiNbO₃ ferroelectric films sputtered on ITO-based conductive electrode, *Materials Chemistry and Physics* **2005**, 92, 424.
- [190] F. Chen, H. Amekura, Y. Jia, Ion Irradiation of Dielectrics for Photonic Applications, *Springer Nature* **2020**.
- [191] B. Knabe, K. Buse, W. Assenmacher, W. Mader, Spontaneous polarization in ultrasmall lithium niobate nanocrystals revealed by second harmonic generation, *Physical Review B* **2012**, 86, 195428.
- [192] V. Lehmann, H. Föll, Formation Mechanism and Properties of Electrochemically Etched Trenches in N-Type Silicon, *Journal of the Electrochemical Society* **1990**, 137, 653.
- [193] B. Ruzicka, E. Zaccarelli, A fresh look at the Laponite phase diagram, *Soft Matter* **2011**, 7, 1268.
- [194] Z. Ren, Y. Li, J. Yu, A flexible supercapacitor with high true performance, *iScience* **2018**, 9, 138.
- [195] S. Kundu, Y. Wang, W. Xia, M. Muhler, Thermal stability and reducibility of oxygen-containing functional groups on multiwalled carbon nanotube surfaces: a quantitative high-resolution XPS and TPD/TPR study, *The Journal of Physical Chemistry C* **2008**, 112, 16869.
- [196] A. Seidel, M. Peterca, H. F. Mark, Encyclopedia of Polymer Science and Technology, *Wiley* **2014**.
- [197] H. Maleki, L. Durães, A. Portugal, An overview on silica aerogels synthesis and different mechanical reinforcing strategies, *Journal of Non-Crystalline Solids* **2014**, 385, 55.
- [198] R. C. Weast, Handbook of Chemistry and Physics, *Chemical Rubber Company* **1972**.
- [199] H. J. Butt, D. S. Golovko, E. Bonaccorso, On the derivation of Young's equation for sessile drops: Nonequilibrium effects due to evaporation, *Journal of Physical*

Chemistry B **2007**, *111*, 5277.

- [200] J. M. D. Coey, *Magnetism and Magnetic Materials*, Cambridge University Press **2010**.
- [201] K. N. Subramanyam, Neutron and X-ray diffraction studies of certain doped nickel ferrites, *Journal of Physics C: Solid State Physics* **1971**, *4*, 2266.
- [202] R. V. Craster, O. K. Matar, Dynamics and stability of thin liquid films, *Reviews of Modern Physics* **2009**, *81*, 1131.
- [203] Z. Ren, Y. Li, J. Yu, A flexible supercapacitor with high true performance, *iScience* **2018**, *9*, 138.
- [204] S. Kundu, Y. Wang, W. Xia, M. Muhler, Thermal stability and reducibility of oxygen-containing functional groups on multiwalled carbon nanotube surfaces: a quantitative high-resolution XPS and TPD/TPR study, *The Journal of Physical Chemistry C* **2008**, *112*, 16869.
- [205] T. E. Buchheit, D. A. LaVan, J. R. Michael, T. R. Christenson, S. D. Leith, Microstructural and mechanical properties investigation of electrode posited and annealed LIGA nickel structures, *Metallurgical and Materials Transactions A* **2002**, *33*, 539.
- [206] D. Y. Zang, S. Tarafdar, Y. Y. Tarasevich, M. D. Choudhury, T. Dutta, Evaporation of a Droplet: From physics to applications, *Physics Reports* **2019**, *804*, 1.
- [207] Y. L. Wang, F. Liu, Y. M. Yang, L. P. Xu, Droplet evaporation-induced analyte concentration toward sensitive biosensing, *Materials Chemistry Frontiers* **2021**, *5*, 5639.

Acknowledgments

First and foremost, I would like to thank my advisor **Prof. Dr. Martin Steinhart** for the opportunity to join the project, his continuous support, and especially for his help with the thesis. I thank him for his contributions of great encouragement, guidance, and assistance in making my PhD period productive and exciting.

Many thanks to **Prof. Dr. Uwe Beginn** for his support and examination of my doctoral thesis.

I wish to thank **Prof. Dr. Joachim Wollschläger** and **Dr. Karsten Küpper** for being part of the examination board.

Many sincere thanks go to **Prof. Dr. Markus Haase**, **Dr. Karsten Kömpe**, **Christian Homann**, and **Jonas Klein** from the University of Osnabrück for their kind support regarding X-ray diffraction and electrochemical experiments.

I would like to acknowledge **Prof. Dr. Uwe Beginn** and **Martin Frosinn** from the University of Osnabrück for the synthesis and characterization of the DNHG-derived aerogel stamp.

Many thanks go to **Prof. Dr. Joachim Wollschläger**, **Dr. Karsten Küpper**, **Dr. Jannis Thien**, and **Kevin Ruwisch** from the Department of Physics at Universität Osnabrück for X-ray photoemission spectroscopy and vibrating sample magnetometer measurements.

I am also very thankful to **Prof. Dr. Imlau**, **Dr. Laura Vittadello**, and **Dr. Christian Kijatkin** from the Department of Physics at Universität Osnabrück for the optical nonlinear measurements of the LiNbO₃ films.

I am very grateful to **Prof. Dr. Dirk Enke**, **Tim Jähnichen**, and **Louisa Eckert** from the University of Leipzig for their kind support regarding nitrogen sorption measurements.

I would like to appreciate **Prof. Dr. Markus Gallei** and **Hanna Hübner** from the University of Saarland for the synthesis and characterization of the PFeMA.

Many sincere thanks to **Claudia Heß** and **Christine Schulz-Kölbel** for their support in the lab, as well as to Barbara Gunkel for her help, especially with administrative issues.

My deepest thanks to our research group members at the University of Osnabrück:

Dr. Helmut Schäfer, Dr. Peilong Hou, Wajiha Akram, Dr. Michael Philippi, Ruža Periz, Dr. Leiming Guo, Dr. Weijia Han, Dr. Qaiser Ali Khan, Dr. Fernando Vázquez-Luna, and Markus Geuß for their support, productive discussions, and enjoyable times together.

Finally, I take this opportunity to thank my parents and my brothers **Muhammed Alarслан, Burak and Emre Günel, Ali and Muhammed Güvendi, Araz Ismayilov, Mohamed Faisal Ali, Burc Acabuga, Fatih Özden, Furkan Özdemir, and Guerino Luca Galzerano** for their long-term encouragement.

List of publications

(A) Publications that report results of this thesis

1. **Alarслан, Fatih**, et al., High-Temperature Stamping of Molten Functional Polymers: Orthogonal Substrate Functionalization for Wettability Management. Submitted.

2. **Alarслан, Fatih**, et al. "Reactive Additive Capillary Stamping with Double Network Hydrogel-Derived Aerogel Stamps under Solvothermal Conditions." *ACS Applied Materials & Interfaces* 14.39 (2022): 44992-45004.

3. **Alarслан, Fatih**, et al. "Thin patterned lithium niobate films by parallel additive capillary stamping of aqueous precursor solutions." *Advanced Engineering Materials* 24.6 (2022): 2101159.

(B) Other publications

1. Klein, Jonas, et al. "Dispersible SnO₂: Sb and TiO₂ Nanocrystals After Calcination at High Temperature." *Small* 2023, 19, 2207674.

2. Klein, Jonas, et al. "Cerium-Modified Mesoporous Antimony Doped Tin Oxide as Intercalation-Free Charge Storage Layers for Electrochromic Devices." *Advanced Functional Materials* 33.4 (2023): 2210167.

3. Klein, Jonas, et al. "Intercalation-free, fast switching of mesoporous antimony doped tin oxide with cathodically coloring electrochromic dyes." *Nanoscale Advances* 4.9 (2022): 2144-2152.

4. Thien, Jannis, et al. "Cationic Ordering and Its Influence on the Magnetic Properties of Co-Rich Cobalt Ferrite Thin Films Prepared by Reactive Solid Phase Epitaxy on Nb-Doped SrTiO₃ (001)." *Materials* 15.1 (2021): 46.

Curriculum Vitae

First Name Fatih
Family Name Alarslan
Date of Birth September 5, 1993
Place of Birth Georgsmarienhütte, Germany
Nationality German
E-mail falarslan@uos.de; fatihalarslan@hotmail.com

EDUCATION

11/2019-05/2023: Ph.D. in Physical Chemistry, University of Osnabrück,
Germany

Supervisor: Prof. Dr. Martin Steinhart

Research Topic: Orthogonal substrate functionalization using additive contact
lithography

10/2017-10/2019: Master in Nanosciences - Materials, Molecules and Cells
Master of Science, University of Osnabrück

Supervisor: Prof. Dr. Martin Steinhart

Research Topic: Periodische Lithiumniobat- und Antimonzinnoxid-
Mikrostrukturen mittels Kapillarstempeln und selektiver
Benetzung

10/2014-01/2018: B.S. in Chemistry, University of Osnabrück, Germany

Supervisor: Dr. Helmut Schäfer

Research Topic: Alternative Synthesewege zur Generierung von PZT
Bulkmaterial und Nanopartikel

Statement of Authorship

I hereby declare that this doctoral thesis describes my own work, unless otherwise acknowledged in the text. I have not used any sources other than those listed in the bibliography and identified as references. I further declare that I have not submitted this thesis at any other institution in order to obtain a degree.

April 2023, Osnabrück

Signature